The Dissertation Committee for Landon Paul Lockhart Certifies that this is the approved version of the following Dissertation:

A Mechanistic Approach for Predicting Pore Pressure in the Delaware Basin

Committee:

Peter B. Flemings, Supervisor

Maria A. Nikolinakou, Co-Supervisor

Demian Saffer

John Germain

A Mechanistic Approach for Predicting Pore Pressure in the Delaware Basin

by

Landon Paul Lockhart

Dissertation

Presented to the Faculty of the Graduate School of

The University of Texas at Austin

in Partial Fulfillment

of the Requirements

for the Degree of

Doctor of Philosophy

The University of Texas at Austin

December 2024

Acknowledgements

The list of people who deserve to be thanked is extensive, and there is no doubt I will inadvertently omit some names. First and foremost, I thank my advisor, Peter Flemings (a congenital optimist), and my co-advisor, Maria Nikolinakou, not only for their tireless work on this dissertation, but also for their long-term efforts to help shape me into a far more capable geoscientist than when I started. Through your patient and persistent instruction, I learned the value of precise and clear communication of ideas, and the amount of effort required to produce work that is not good but excellent. I also thank Jack Germaine for his contributions and insights into my research, as well as for the tremendous effort he spent each year helping prepare me for my countless GeoFluids talks. I thank Demian Saffer for serving on my PhD committee and for his meticulous edits on this dissertation, which have greatly contributed to its clarity.

I thank Athma Bhandari and Mahdi Heidari for sharing with me their wealth of knowledge in the field of geomechanics. Athma, in particular, showed immense patience as he taught me the intricacies of experimental work. Mahdi was always generous with his time in helping me tackle the many complex mathematical problems (which to him were probably rudimentary) I encountered in my research. I thank Josh O'Connell and Donnie Brooks for helping me in the lab. I thank Fran Pena for her scheduling assistance. Additionally, I am sincerely grateful for my friends whom I made in graduate school and for the fun we had – Kevin, Will, Zach, and Sebas, to name a few.

I also wish to thank my family for their unconditional love and support during my extensive time in school. I could not ask for two better parents – Jim and Susan – nor two better siblings – Hunter and Meredith. My parents' unwavering commitment and love toward each other is perhaps the most valuable lesson I have learning during these years I

have been in school, especially now as I progress through my second year of marriage. Hunter, you inspired me to be a geoscientist. There is no doubt that I would have never been accepted into a great school like UT without your help. You have always been someone I have looked up to – whether it be academically, spiritually, or as a husband. Meredith, you are, like your twin, someone I also look up to. You have inspired in me a desire to achieve excellence in life while also having fun.

I thank Matthew Elias and Jim Ballingall for serving as my mentors outside of school. I look up very high to you both as intellectuals, leaders, and husbands.

Finally, I would like to thank my wife and best friend, Rachel. I have put you through the wringer these past few years. Without your unwavering love and support, I could not have handled the many ups and downs of graduate school. I am more thankful for you than words can say. I am excited for what lies ahead of us in the years to come.

To God be the glory.

Abstract

A Mechanistic Approach for Predicting Pore Pressure in the Delaware Basin

Landon Paul Lockhart, Ph.D.

The University of Texas at Austin, 2024

Supervisor: Peter B. Flemings

Co-Supervisor: Maria A. Nikolinakou

My dissertation is concerned with the material behavior of mudrocks subjected to uplift and erosion, and how a physical understanding of this behavior can be used to predict the pore pressure. The concepts presented here integrate theory, field data, and experimental measurements.

Mudrock deformation is described by elastoplasticity: a rock will experience elastic and plastic deformations during loading, and will recover only the elastic deformations during unloading. Using this framework, I develop a model to describe the compaction state of a mudrock with a burial history of loading and erosional unloading. I establish that this behavior is systematically reflected by sonic P-wave velocities, thereby providing a mechanism for predicting a mudrock's compaction state. I calibrate the parameters of this model to field data in the Delaware Basin and show that the predicted pressures align more closely with the measured pressures compared to the traditional approaches, which fundamentally assume that a mudrock's compaction state is described the normal compaction (loading) trend, regardless of its burial history.

I then both petrophysically determine and experimentally constrain one of the central parameters in my model: the pore pressure buildup coefficient. This describes the undrained change in pore pressure due to a mechanical change in stress (e.g., erosion). I demonstrate that the petrophysical approach provides an efficient and cost-effective way to determine this coefficient compared to experimental measurements.

Lastly, I incorporate the thermal pressure coefficient into my model to account for the undrained change in pore pressure during erosional unloading when a rock is uplifted from a deeper, warmer depth to a shallower, cooler depth. I determine this parameter using petrophysical data and integrate it into my model for predicting pore pressure. I then predict pressure in a number of wells and show that this final approach successfully captures the underlying physical behavior of mudrocks with erosional unloading.

Ultimately, my works provides (1) a framework for better understanding the physical behavior of mudrocks in a basin with uplift and erosion, and (2) a method for predicting regional variations in uplift and erosion and the absolute pressures using wireline velocity data.

Table of Contents

List of Tables

List of Figures

Chapter 1: Introduction

1.1 Chapter Overview

In this introductory chapter, I begin with the background and motivation of my research. I then provide a brief summary of the content of each subsequent chapter, with an emphasis on the scientific insights and a discussion of what links them together, followed by an overview of the appendices. Lastly, I summarize the key conclusions of my dissertation and conclude with my recommendations to guide future work.

1.2 Background & Motivation

An understanding of the causal mechanisms that generate abnormal pore pressures is essential for the safe and efficient recovery of hydrocarbons, the advancement of the energy transition, and the processes associated with geological hazards. In the context of hydrocarbon recovery and the energy transition, an ability to accurately predict such pressures is critically important for identifying drilling hazards (Sweatman et al., 1999), locating potential drilling targets (Loughry et al., 2015), disposal of wastewater (Pskowski, 2024), and sequestration of CO_2 (Obradors-Prats et al., 2017). On the other hand, pressures in excess of hydrostatic (overpressure) can trigger earthquakes (Zoback and Gorelick, 2012), landslides (Rubey and Hubbert, 1959), hydraulic fractures (Pearson, 1981), sand injectites (Sanford, 2015), and mud volcanoes (Westbrook and Smith, 1983).

Much research has focused on understanding the physical processes that generate abnormal pressures in offshore basins (e.g., Gulf of Mexico Basin). As a result, there are well-established techniques to predict these pressures in such basins. Yet, the opposite is true of onshore basins (e.g., Delaware Basin). To date, very few well-documented, systematic, detailed studies of abnormal pressures in onshore basins has been conducted,

leaving the causal mechanisms that control these pressures virtually unexplored, and a physics-based prediction approach nonexistent.

One of the defining geological differences between offshore and onshore basins is the presence of erosion; over six major US basins onshore have experienced erosion in excess of 3,000 ft (Xia et al., 2013). This presents a particular challenge for predicting pore pressure.

Fundamental to pore pressure prediction is the compaction state of the rock. The prevailing conceptual model, regardless of the type of environment, is based on the idea that rocks monotonically compact during burial. This process causes a reduction in porosity as the sediments deform, rearrange, and dissipate excess fluid pressure (Lambe and Whitman, 1969). As the porosity decreases, the effective stress, which is the average stress transmitted through the rock skeleton, increases. If the fluids are unable to freely expel, this will prevent the rock from normally compacting as the fluids take on additional load and become overpressured.

This prevailing conceptual model is broadly applicable to offshore basins where a continuous supply of sediment is the primary driver of a rock's compaction state; thus, there is an implied single relationship between compaction state and effective stress. However, this model does not reflect the compaction behavior of onshore basins that have burial histories marked by uplift and erosion. This is because the stiffness of a rock is different when it is unloaded, and thus the relationship between compaction state and effective stress in non-unique. Yet, exactly how it is different is not well understood.

Thus, the fundamental question of my doctoral research is concerned with the material behavior of mudrocks subjected to erosional (mechanical) unloading, and how an understanding of this behavior can be used to predict stress and thus pore pressure.

I methodically address this question and present my findings in the succeeding chapters. The concepts I present are grounded in theory, field data, and experimental measurements, and the overall aim of my dissertation is broadly to provide a physics-based approach for understanding and predicting the mechanical behavior, and thus pore pressure, of unloaded mudrocks.

1.3 CHAPTER OVERVIEWS

1.3.1 Chapter 2

In this chapter, which is published in *Marine and Petroleum Geology* (Lockhart et al., 2023), I present a velocity-based approach to predict pore pressure in an onshore unconventional basin affected by erosional unloading. Predicting pore pressure in these types of basins has been a fundamental challenge for decades. My approach integrates an elastoplastic model with a concept of how pore pressure responds to unloading. I demonstrate my approach in the Delaware Basin using a calibration well and four prediction wells. My results show that this approach is an improvement over conventional pore pressure prediction techniques that do not physically capture the unloading behavior of mudrocks.

The impact of this chapter is twofold. First, it offers a reliable tool for predicting pore pressure in a basin that has experienced significant unloading; this enhances drilling safety and efficiency. Second, it provides deeper insights into how stress history impacts rock deformation and pore pressure. This contributes to a broader understanding of the complex interplay between pressure and stress in eroded basins.

A central assumption in my approach is that the uniaxial strain pore pressure buildup coefficient C is constant across the basin. C describes the undrained changes in pore pressure due to erosional unloading, and it is a function of the porosity and the

compressibilities of both the solid and fluid phases of the rock. Whereas my approach provides a significant advancement in predicting pore pressure in unloaded basins, an improvement of my approach involves a process to independently determine this parameter in the prediction wells. I address this challenge in the next chapter.

1.3.2 Chapter 3

In Chapter 3, I present two distinct approaches for determining Skempton's pore pressure buildup coefficient B (B describes the undrained change in pore pressure due to a change in isotropic stress and is mathematically related to the uniaxial strain pore pressure buildup coefficient C) using a dataset comprising Wolfcamp A mudrock obtained from a well in the Delaware Basin.

The first is an effective medium approach for computing Skempton's B using petrophysical data. The second involves experimental testing on mudrock samples, which is accomplished by superimposing an incremental change in confining stress on a pre-existing state of confining stress and pore pressure; the resulting ratio of the undrained change in pore pressure to change in stress yields Skempton's B. I apply both approaches at the same depths.

My results show that both approaches yield comparable Skempton's B coefficients. However, my work underscores that the computational approach offers an efficient and cost-effective alternative for estimating Skempton's B that avoids the complexities and challenges associated with experimental testing, of which the most challenging (and can be the most consequential) is the difficulty of achieving truly undrained conditions.

Although this chapter establishes a reliable way for determining the Skempton's B coefficient (and thus the C coefficient) using data that is available in the prediction wells,

I left actual application of its ability to predict pore pressure unexplored. I address this in my subsequent and final chapter.

1.3.3 Chapter 4

In this final chapter, I integrate my model for predicting pore pressure in unloaded basins (introduced in Chapter 2) with an effective medium approach for determining the uniaxial strain pore pressure buildup coefficient C and the thermal pressure coefficient α in each prediction well using petrophysical data. For my computation of C, I first determine Skempton's B coefficient using the approach I presented in Chapter 3, after which I mathematically transform Skempton's B to C using field data.

A core scientific insight of this chapter is a clear delineation of the undrained changes in pore pressure due to both changes in mechanical stress (e.g., due to erosion) and changes in temperature (e.g., due to uplift); the C coefficient defines the undrained changes in pressure due to changes in mechanical stress, and the α coefficient defines the undrained changes in pressure due to changes in temperature.

My application of this integrated method predicts pore pressures that compare remarkedly well to the measured pressures in each well. Thus, the impact of this chapter is an extension of Chapter 2: it offers yet a more reliable tool for predicting pore pressures in basins with erosional unloading, and it provides an even deeper insight into how a rock's burial history impacts its deformation and the resulting pore pressure response.

1.3.4 Appendices

I conclude my manuscript with a number of appendices that supplement the content of each chapter. My main goal is to provide the readers with detailed instructions on how to replicate the experiments and models I developed during my doctoral research. Although

the procedures are tailored to the equipment and data that were available to me during my time in graduate school, it is my hope that they may serve as a foundation for those seeking to adapt these methodologies using different equipment or datasets, and to build upon the findings contained herein.

1.4 CONCLUSIONS

My dissertation provides a comprehensive study of the prediction of pore pressure and stress in unconventional basins, with a focus on the Delaware Basin. A first-order observation underlying my work is that the majority of unconventional basins have experienced erosional unloading. Consequentially, the compaction behavior during loading will be different than its behavior during unloading.

I develop a velocity-based approach for predicting pore pressure that integrates the principles of elastoplasticity with the concept of a pore pressure buildup coefficient. This model effectively captures – and predicts – how a variable stress history impacts rock deformation and pore pressure. The key conclusions of my dissertation are as follows.

1. Erosional unloading can have a significant impact on the stress state and thus pore pressure of mudrocks. Pore pressures in basins with erosional unloading can range from sub-hydrostatic to more than a two-fold increase in overpressure.
2. The material behavior (e.g., compaction state) of an unloaded mudrock is not described by the normal compaction trend; instead, it is described by the principles of elastoplasticity.
3. Velocity systematically reflects the loading and unloading behavior of mudrocks.
4. The approach I develop to predict pore pressure in basins with erosional unloading better matches the measured pressures in each of the study wells compared to the

conventional approaches which do not physically capture the unloading behavior of mudrocks.

5. Determination of Skempton's pore pressure buildup coefficient B in Wolfcamp mudrocks, using either an effective medium computational approach with petrophysical data or experimental measurements on test samples, yields comparable results. However, the computation approach is significantly more time-efficient and cost-effective than the traditional experimental method.
6. The sum of the pore pressure buildup coefficient C and the thermal pressure coefficient α captures the undrained changes in pore pressure for a basin with structural uplift and erosion: C accounts the mechanical changes in stress due to erosion, and α accounts for the temperature changes associated with uplift. In all the wells studied, 26% of the total change in undrained pore pressure is due to the mechanical effects, and 74% is due to the thermal effects; both have to be considered to effectively describe the pore pressure response to erosion.
7. My work provides an effective method for predicting pore pressure in unconventional basins with uplift and erosion, and contributes to an overall improved understanding of the complex interplay between pressure and stress in the subsurface.

1.5 FUTURE WORK

The insights and methodologies presented in my dissertation lay the foundation for further research, and my practical recommendations to assist in this endeavor are summarized as follows.

1. Experimentally measure the lithology-dependent A and B normal compaction curve parameters in my pore pressure prediction approach (Eq 4.28), which I assume in this dissertation from literature for illitic mudrocks (Heppard and Ebrom, 2010).
2. Experimentally measure the unloading parameter U in my pore pressure prediction approach (Eq 4.28), which I empirically constrain in the drained section of my calibration well (see Chapter, section 2.4).
3. During experimental measurements of Skempton's B coefficient (documented in Chapter 3, section 3.3), minimize the ratio of dead volume to sample volume either by:
    a. **Reducing the dead volume.** This would require either new experimental equipment with an improved system design that moves the pressure transducer closer to the endcap, or to engineer the current equipment to facilitate this (e.g., one potential suggestion is to insert steel wire into the drainage lines to reduce the dead volume).
    b. **Increasing the sample volume.** This can be done by using samples with a larger diameter (e.g., 1.5" instead of the 1" diameter test samples used in this research), and greater test sample lengths (I used samples with 1" length; however, utilizing the maximum length that the equipment can accommodate would be an improvement). However, it should be noted that this will increase the time required for the experiments.
4. Refine my process for correcting the experimental measurements of Skempton's B coefficient (documented in Chapter 3, section 3.3) by experimentally measuring the static bulk compressibility to define this parameter, rather than determining it dynamically from the wireline velocities and bulk density.

5. Refine my process both for computing Skempton's B coefficient and for correcting the experimental measurements of Skempton's B (documented in Chapter 3, section 3.3) by directly determining the solid aggregate phase with x-ray diffraction (XRD) and total organic content (TOC) at the test sample depths, rather than estimating these from x-ray fluorescence (XRF) data.
6. Refine my process for defining the thermal pressure coefficient α (Chapter 4, section 4.4) by experimentally measuring α on test samples; compare these results to the values I computed in Chapter 4 (section 4.4).

Chapter 2: The Impact of Late-Stage Erosion on Pressure Prediction with Application in the Delaware Basin, U.S.[1]

2.1 ABSTRACT

I predict pore pressure from velocities in unconventional basins that have been unloaded by erosion. My method incorporates an elastoplastic model for soil behavior with a description of how the pore pressure changes as a function of erosional unloading. I demonstrate my method in the eastern portion of the Delaware Basin where significant erosion has occurred. I use well log and measured pore pressure data to establish a relationship between velocity and vertical effective stress in a well with a known erosional value. I use this relationship to predict the regional variations in erosion and vertical effective stress from velocities. I demonstrate the predictive capability of my approach by comparing my results against measured pore pressures that I interpret from drill-stem tests (DSTs) in four prediction wells spanning the eastern portion of the basin.

2.2 INTRODUCTION

An accurate knowledge of pore pressure is important to safely and economically drill for hydrocarbons. The classic techniques to predict pore pressure were developed in Gulf of Mexico shelf settings (Swarbrick et al., 2013). One common approach is to use a normal compaction trend (Bowers, 1995; Eaton, 1975) to relate porosity, or some proxy of porosity (e.g., velocity, resistivity, or density), to vertical effective stress (Flemings, 2021). This assumes there is a single relationship between porosity and vertical effective stress; only one porosity is associated with a particular vertical effective stress.

I demonstrate mudrock compaction with a drained uniaxial deformation test on material reconstituted from Gulf of Mexico sediments (Figure 2.1). Initially, the specimen

[1] The full content of this chapter is published in *Marine and Petroleum Geology*, Vol. 150, April 2023.

is loaded from points ‘a’ to ‘b’ under uniaxial strain. As the axial (vertical) effective stress increases, there is a rapid decrease in porosity (Figure 2.1A) and a rapid increase in velocity (Figure 2.1B). In geotechnical engineering, this is termed the compression curve (Germaine and Germaine, 2009; Lambe and Whitman, 1969), and in the geosciences we often term it as the normal compaction path, or, more generally, a porosity-effective stress curve (e.g., Flemings, 2021): along this path, the applied stress is always the maximum stress the sample has ever experienced.

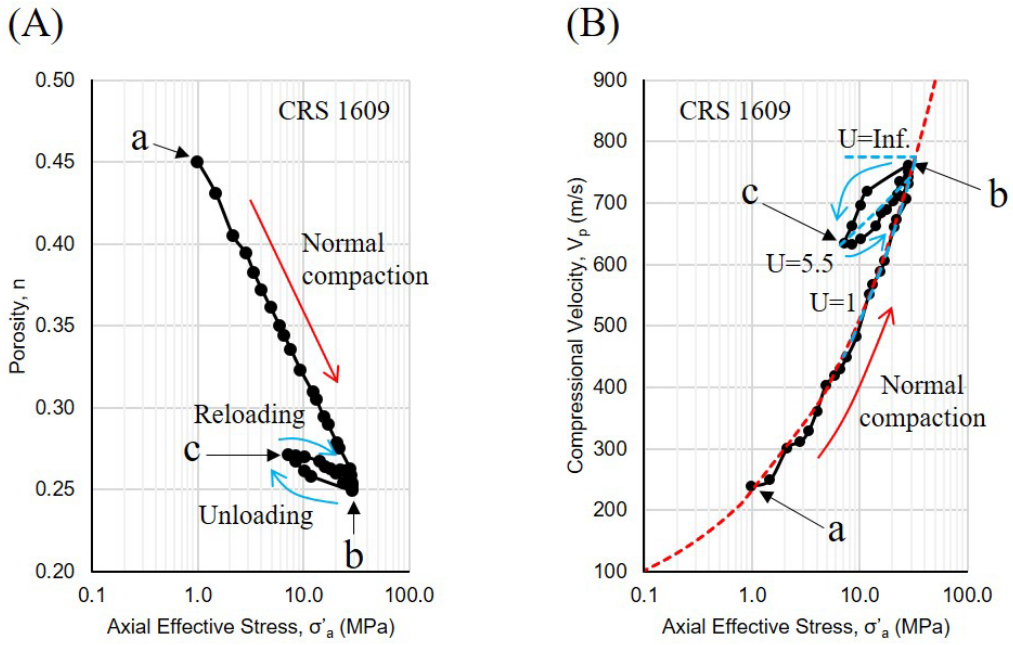

Figure 2.1: Mudrock compaction. Porosity (left) and velocity (right) as a function of effective stress in laboratory experiments. (A) Porosity versus axial effective stress during loading (points ‘a’ to ‘b’), unloading (points ‘b’ to ‘c’), and subsequent reloading (points ‘c’ to ‘b’). (B) Compressional velocity versus axial effective stress during loading (points ‘a’ to ‘b’), unloading (points ‘b’ to ‘c’), and subsequent reloading (points ‘c’ to ‘b’). Uniaxial compression test results on a resedimented Gulf of Mexico Eugene Island mudrock (constant rate of strain (CRS) 1609); from Germaine (2020). Reprinted with permission by John Germaine.

Bowers (1995) proposed the following equation between velocity (V) and vertical effective stress (σ_v') to describe loading along the normal compaction path:

$$V = V_w + A\sigma_v'^B, \qquad (2.1)$$

where V_w is the velocity of sound in water, and A and B are lithology-dependent constants. I fit Eq. 2.1 to the normal compaction data in Figure 2.1B. I find A equal to 133 $\frac{ft}{psi^B * s}$ (229 $\frac{m}{MPa^B * s}$), and B equal to 0.348, with V_w = 5,000 $\frac{ft}{s}$ (1,524 $\frac{m}{s}$). The model (red dashed line in Figure 2.1B) matches the observed normal compaction path (points 'a' to 'b' in Figure 2.1B).

In normally compacted basins that have not experienced unloading, vertical effective stress can be computed from Eq. 2.1 once A and B are known. If the lithostatic stress (σ_v) is known, pore pressure (u) can then be determined:

$$u = \sigma_v - \sigma_v'. \qquad (2.2)$$

Equations 2.1 and 2.2 have been applied in countless studies (Merrell et al., 2014; Sayers et al., 2002; Zhang, 2011). However, this technique, like other traditional approaches that rely on the normal compaction path, often fails to predict pore pressures in more complex settings than the Gulf of Mexico shelf (Gutierrez et al., 2006; Heidari et al., 2018; Lockhart, 2018). One limitation is their inability to capture the compaction and velocity behavior of unloaded mudrock. Unloading results in a net decrease in effective stress with time (Bowers, 1995). Under these conditions, the relationship between porosity and vertical effective stress is non-unique; a porosity is no longer associated with a single effective stress (Figure 2.1A).

To illustrate the material response of mudrocks to unloading, I return to the experiment illustrated in Figure 2.1. After the specimen was loaded from points 'a' to 'b,' it was unloaded to point 'c.' Point 'b' records the preconsolidation stress: the maximum past stress to which the rock has been exposed. When the specimen was unloaded, its

porosity and velocity followed a different path than the normal compaction curve (points ‘a’ to ‘b’); both porosity and velocity changed at reduced rates. This is because the deformation behavior of mudrocks is elastoplastic. During loading from point ‘a’ to point ‘b,’ the deformation includes both elastic (recoverable) and plastic (irrecoverable) components. However, when unloading from ‘b’ to ‘c’ and when reloading from ‘c’ to ‘b,’ the deformation is elastic (recoverable) (Germaine and Germaine, 2009).

The geological process of unloading can result from an increase in pressure due fluid volume expansion (e.g., hydrocarbon generation and gas cracking, aquathermal expansion). Alternatively, it can occur by a decrease in total stress (e.g., erosion) or a change in tectonic stress (e.g., a reduction in lateral stress).

Sinclair (2007) employed the Equivalent Depth (Hottmann and Johnson, 1965) and the Eaton Ratio (Eaton, 1975) methods to predict pressure in the Delaware Basin. In both cases, Sinclair (2007) relied on establishing a normal compaction trend by determining a relationship between velocity and effective stress in the shallow drained interval of the basin. He used this relationship to predict pore pressure in eleven wells and examined his results against pressures interpreted from drill-stem tests. His results from both methods match the measured pressures in six wells but under-predict pore pressure in the remaining 5 wells. Couzens-Schultz et al. (2013) also derived a normal compaction trend from velocity and effective stress. However, they constrained this relationship in the overpressured strata. To predict pore pressure in offset wells, they found that the best approach was to assume a constant vertical effective stress within equivalent stratigraphic intervals. This allowed them to predict pressure in wells with different amounts of overburden.

Bowers (1995) proposed a velocity-vertical effective stress equation to capture the compaction state of an unloaded mudrock:

$$V = V_w + A\left[\sigma_p'\left(\frac{\sigma_v'}{\sigma_p'}\right)^{\frac{1}{U}}\right]^B. \qquad (2.3)$$

Eq. 2.3 shares the same V, V_w, and A and B parameters as the loading equation (Eq. 2.1) but has two additional parameters: U and σ_p'. U describes the velocity behavior during unloading. With U = 1, the velocity behavior during normal compaction is identical to the velocity during unloading (blue dashed line in Figure 2.1B). With U equal to infinity, the velocity of the rock does not decline during unloading (blue dashed line in Figure 2.1B). σ_p' is the preconsolidation stress; it is the maximum past vertical effective stress to which the rock has been subjected. Zhang (2013) proposed a similar method that incorporates a compaction constant that can be adjusted for unloading.

I fit Eq. 2.3 to the unloaded data in Figure 2.1B. I show that with a U of 3.2 $\frac{ft}{psi^{B*s}}$ (5.5 $\frac{m}{MPa^{B*s}}$), a σ_p' of 4,200 psi (29 MPa), and the same A, B, and V_w as presented above for the loading trend, the model (orange dashed line in Figure 2.1B) matches the observed unloading path (points 'b' to 'c' in Figure 2.1B).

The four parameters in Eq. 2.3 need to be constrained with field data. Bowers (1995) determines A and B in a section that is not unloaded. Unfortunately, if the section has been unloaded, the preconsolidation stress and the U parameter are difficult to determine. Bowers (1995) suggested that one approach to determine the preconsolidation stress is to assume that the maximum velocity in the well records the preconsolidation stress. Bowers (2001) later suggested that an alternate approach is to cross-plot the transport properties (e.g., sonic velocity, resistivity, or permeability) with the bulk properties (e.g., bulk density or porosity).

I present a different approach to constrain the parameters in Eq. 2.3, and I demonstrate my approach in the highly eroded eastern portion of the Delaware Basin. In my calibration well, the amount of erosion is known from literature, and I am thus able to

determine the decrease in total vertical stress. I use this to compute the preconsolidation stress in the hydrostatically pressured interval. I am then able to constrain the unloading coefficient U with an assumed A and B value. I lastly fit my model to the overpressured section with a pore pressure buildup coefficient and predict pore pressure in four wells. I compare my results to measured pressures and an approach that relies on the normal compaction trend.

2.2.1 Pressure Buildup Coefficient and Preconsolidation Stress

When a basin experiences erosion, the total stress is reduced by $\Delta\sigma_v$ (where $\Delta\sigma_v = \Delta H \frac{\Delta\sigma_v}{\Delta Z}$). The resultant change in effective stress is:

$$\Delta\sigma_v' = \Delta\sigma_v - \Delta u. \tag{2.4}$$

Given an initial effective stress of σ_v', then, after unloading, the preconsolidation stress is:

$$\sigma_p' = \sigma_v' - \Delta\sigma_v'. \tag{2.5}$$

For drained mudrock, the pore pressure remains hydrostatic, and $\Delta\sigma_v'$ equals the change in overburden ($\Delta\sigma_v$) less the change in hydrostatic pore pressure (Δu_h):

$$\Delta\sigma_v' = \Delta\sigma_v - \Delta u_h. \tag{2.6}$$

If the thickness of rock eroded is ΔH, then the change in effective stress under drained conditions is:

$$\Delta\sigma_v' = \Delta H \left(\frac{\Delta\sigma_v}{\Delta Z} - \frac{\Delta u_h}{\Delta Z}\right), \tag{2.7}$$

where $\frac{\Delta\sigma_v}{\Delta Z}$ is the overburden gradient, and $\frac{\Delta u_h}{\Delta Z}$ is the water pore pressure gradient. Thus, the preconsolidation stress, under drained conditions ($\sigma_{p,D}'$), is:

$$\sigma_{p,D}' = \sigma_v' - \Delta H \left(\frac{\Delta\sigma_v}{\Delta Z} - \frac{\Delta u_h}{\Delta Z}\right). \tag{2.8}$$

The situation is more complicated when the fluids within the mudrock cannot drain. For undrained mudrock, the change in pore pressure (Δu) is a function of the change in total stress:

$$\Delta u = C\Delta\sigma_v, \tag{2.9}$$

where C, uniaxial strain pore pressure buildup coefficient (also referred to as the loading efficiency in other literature), is a function of porosity, the compressibilities of the bulk, solid, and fluid, and the undrained Poisson's ratio (Wang, 2000b).

C can range from 0 to 1. A C of 0 implies that the pore pressure changes are independent from the changes in applied stress during either loading or unloading. A C of 1 implies that the pore pressure increase is equal to the increase in total stress. Compressible mudrocks will have a C of approximately 1 if there is only water in their pores. However, more indurated mudrocks, such as present in unconventional basins, may have a lower C if only water is present (Flemings, 2021). Additionally, C may be lower if there is a compressible fluid in the pores (e.g., oil or gas) relative to the stiffness of the mudrock.

Under undrained conditions, the change in effective stress is:

$$\Delta\sigma_v' = \Delta H \frac{\Delta\sigma_v}{\Delta Z}(1 - C). \tag{2.10}$$

Equations 2.5 and 2.10 are combined to express the undrained preconsolidation stress ($\sigma_{p,UD}'$):

$$\sigma_{p,UD}' = \sigma_v' - \Delta H \frac{\Delta\sigma_v}{\Delta Z}(1 - C). \tag{2.11}$$

Given the equations for drained (Eq. 2.8) and undrained (Eq. 2.11) preconsolidation stress, I can now combine these with the unloading velocity equation to model drained mudrock:

$$V = V_w + A\left[\left(\sigma_v' - \Delta H\left(\frac{\Delta\sigma_v}{\Delta Z} - \frac{\Delta u_h}{\Delta Z}\right)\right)\left(\frac{\sigma_v'}{\sigma_v' + \Delta H\left(\frac{\Delta\sigma_v}{\Delta Z} - \frac{\Delta u_h}{\Delta Z}\right)}\right)^{\frac{1}{U}}\right]^B, \tag{2.12}$$

and undrained mudrock:

$$V = V_w + A\left[\left(\sigma_v' - \Delta H\frac{\Delta\sigma_v}{\Delta Z}(1-C)\right)\left(\frac{\sigma_v'}{\sigma_v' + \Delta H\frac{\Delta\sigma_v}{\Delta Z}(1-C)}\right)^{\frac{1}{U}}\right]^B. \quad (2.13)$$

2.3 Unloading Pore Pressure Prediction Workflow

I integrate Bowers' velocity-based unloading equation (Eq. 2.3) with my description of preconsolidation stress (Equations 2.8 and 2.11) to predict pressure. To constrain the model, the following information is required at a single location: (1) a lithologic description of the section (typically described at least by the gamma-ray log); (2) a velocity log; (3) known pore pressures; and (4) knowledge of the amount of erosion. Table 2.1 shows a generalized overview of the workflow to calibrate the model, and Table 2.2 shows a generalized overview of the workflow to predict pore pressure with the calibrated model.

Entire depth of calibration well	**Drained interval**	**Undrained interval**
1.1: Define drained and undrained intervals	**2.1:** Define A and B parameters	**3.1:** Constrain C parameter
↓	↓	
1.2: Pick mudrock velocities	**2.2:** Constrain U parameter	
↓		
1.3: Smooth sonic velocities		
↓		
1.4: Calculate lithostatic stress		

Table 2.1: Model calibration workflow. See text for full description.

Entire depth of well	Drained interval	Undrained interval
1.1: Repeat steps 1.1-1.4 of calibration process	**2.1:** Estimate erosion	**3.1:** Estimate pore pressure

Table 2.2: Model prediction workflow. See text for full description.

2.4 CASE STUDY: DELAWARE BASIN

2.4.1 Geological Overview

The Delaware Basin extends across portions of New Mexico and Texas and is one of several sub-basins comprising the overall Permian Basin (Figure 2.2). It is bounded to the north by the Northwestern shelf, to the east by the Central Basin platform, to the south by the Marathon fold and thrust belt, and to the west by the Diablo platform.

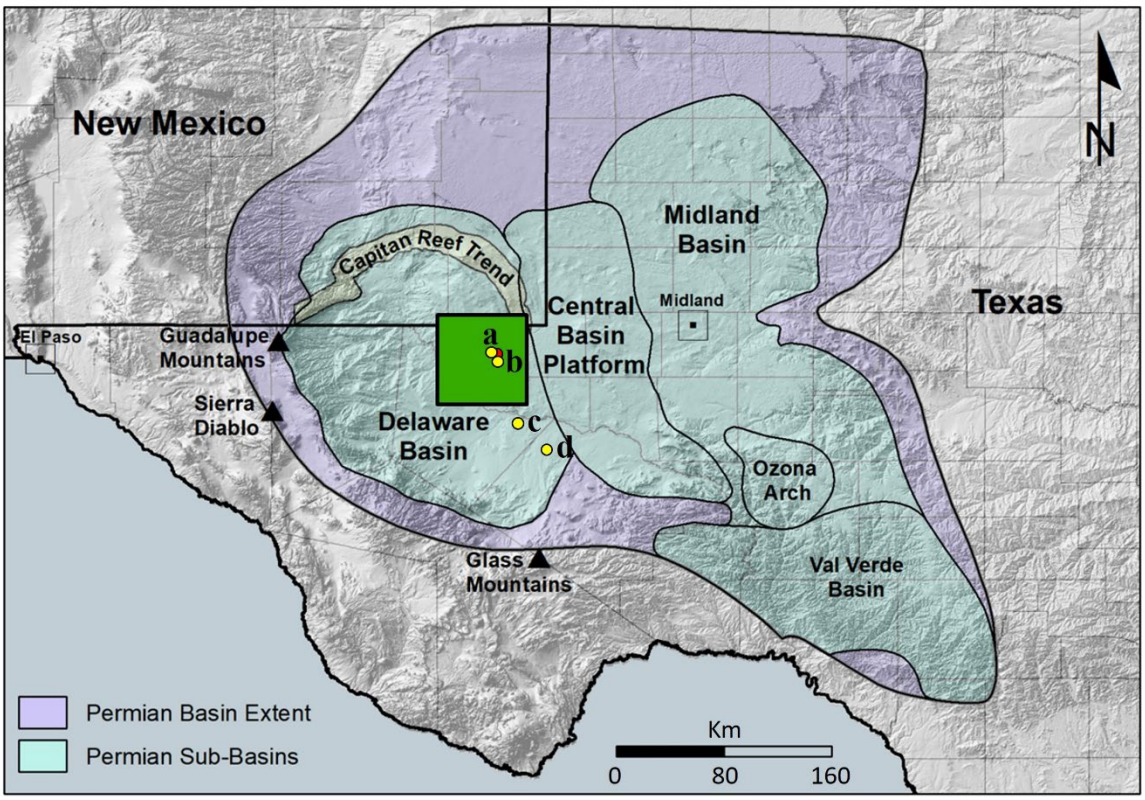

Figure 2.2: Map of study area. The green box marks the general location of the calibration well included in this paper. The red dot marks the location of the well Sinclair (2007) used to determine erosion. The yellow dot marks the location of the wells used to predict pore pressure: (a) Harrison 1001 well (UWI 42-301-300700000); (b) AG Hill Haley 1a well (UWI 42-301-303390000); (c) R Cleveland et al 2 well (UWI 42-389-003750000); (d) Jo Neal 43 well (UWI 42-371-101750000). Figure is modified from Ramiro-Ramirez et al. (2020).

I include one calibration well and four prediction wells in this study. The burial history is known at my calibration well (Figure 2.3). At this location, Sinclair (2007) used a combination of thermochronology and shale compaction curves to determine that there were two phases of uplift and erosion: the Laramide Orogeny (55-50 Ma), and the Basin and Range Event (25-10 Ma). This resulted in a net amount of erosion equal to 6,890' (2,100 m).

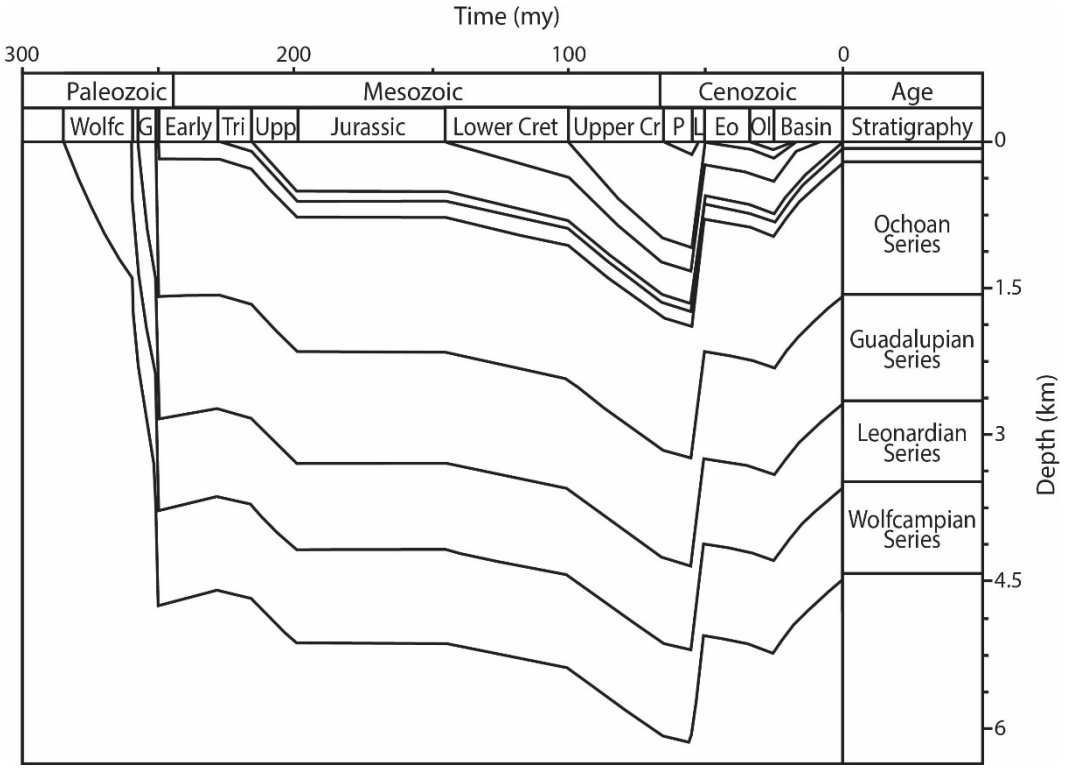

Figure 2.3: Geohistory diagram of the JE Haley 24-1 well. Well is located in Figure 2.2 (red dot). Figure is modified from Sinclair (2007).

The rocks at my calibration well are divided into the Wolfcampian, Leonardian, Guadalupian, and Ochoan Series (Figure 2.3). The Wolcampian, Leonardian, and Guadalupian-age rocks were deposited in marine environments. They largely consist of fine-grained sandstones, siltstones, mudrocks, and various types of limestones (Bachman, 1984). The Ochoan-age rocks were deposited in an evaporitic basin (Dutton et al., 2004). They primarily consist of anhydrite and halite with small amounts of limestone, siltstone, and mudrock (Bachman, 1984).

2.4.2 Model calibration

I calibrate my model with gamma ray (Figure 2.4A), resistivity (Figure 2.4B), bulk density (Figure 2.4C), and sonic compressional velocity (Figure 2.4D) log data, and 20

interpreted pore pressure measurements (black squares in Figure 2.4). I first define the drained and undrained intervals. Overpressure generally begins in the Bone Springs Formation (Lee and Williams, 2000; Luo et al., 1994; Rittenhouse et al., 2016). I observe a reversal in velocity, density, and resistivity log data that occurs at approximately the top of the Bone Springs (8,300' (2,530 m) in Figure 2.4); a reversal of this type can be a strong indicator of the onset of overpressure (Bowers, 2002). Accordingly, I interpret the interval extending from the base of salt (4,300' (1,311 m) in Figure 2.4) to the log reversals (8,300' (2,530 m) in Figure 2.4) to be hydrostatic and hence drained. I assume all the rocks below this to be fully undrained. I return to this assumption in my discussion.

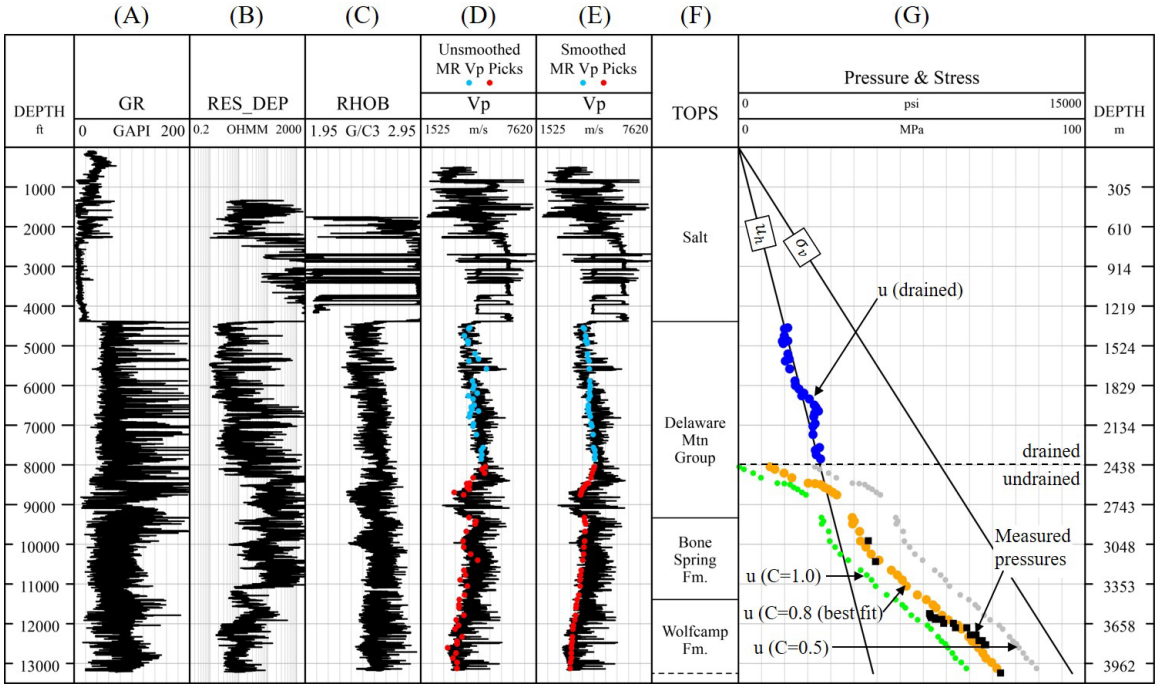

Figure 2.4: Calibration well. (Located within the green box in Figure 2.2). (A) Standard gamma-ray log. (B) Deep resistivity log. (C) Bulk density log. (D) Compressional sonic velocity log. Blue dots are the unsmoothed velocities from the mudrocks picked in the drained interval; Red dots are the unsmoothed velocities from the mudrock picked in the ndrained interval. (E) Compressional sonic velocity log. Blue dots are the smoothed velocities from the mudrock picked in the drained interval; Red dots are the smoothed velocities from the mudrock picked in the undrained interval. (F) Geological tops. (G) Pressure and stress plot: blue dots are the drained pore pressures (Eq. 2.12; parameters provided in Table 2.3; green (C=1.0), orange (C=0.8), and gray (C=0.5) dots are the undrained pore pressures (Eq. 2.13; parameters provided in Table 2.3 unless otherwise noted); black squares are the measured pore pressures.

I calculate the lithostatic stress by integrating the weight of the overlying material:

$$\sigma_v(Z) = \int_0^Z \rho_b g dZ, \qquad (2.14)$$

where ρ_b is the bulk density measured from the wireline bulk density log, Z is depth, and g is acceleration of gravity. In the sections where the overburden curve is missing, I interpolate density using an empirical depth versus porosity relationship (Athy, 1930):

$$n = n_0 e^{-\lambda Z}, \qquad (2.15)$$

where n is porosity, n_0 is surface porosity, and λ is an empirically derived constant. Bulk density is converted to porosity by the following equation:

$$n = \frac{\rho_b - \rho_m}{\rho_f - \rho_m}, \quad (2.16)$$

where ρ_m is the matrix density and ρ_f is the fluid density. I assume a ρ_m of 2.7 $\frac{g}{cm^3}$ and a ρ_f of 1.024 $\frac{g}{cm^3}$. I fit λ to my density data with an assumed surface porosity of 0.48 and use Eq. 2.15 to calculate porosity in the missing section. I then convert the interpolated porosities to densities (Eq. 2.16).

The derived lithostatic gradient varies from 0.82 $\frac{psi}{ft}$ (18.55 $\frac{KPa}{m}$) to 1.05 $\frac{psi}{ft}$ (23.75 $\frac{KPa}{m}$). It is lowest in the salt and increases with depth. I average it with depth and find the gradient to be 1.04 $\frac{psi}{ft}$ (23.53 $\frac{KPa}{m}$). I assume a hydrostatic gradient of 0.44 $\frac{psi}{ft}$ (9.95 $\frac{KPa}{m}$).

Parameter	Description	Input (Imperial)	Input (SI)
A	Parameter in velocity-vertical effective stress equation	14 $\frac{ft}{psi^B * s}$	161 $\frac{m}{MPa^B * s}$
B	Parameter in velocity-vertical effective stress equation	0.730	0.730
V_w	Velocity of sound in water	5,000 $\frac{ft}{s}$	1,524 $\frac{m}{s}$
ΔH	Erosion	6,890 ft	2,100 m
U	Slope of the velocity-effective stress unloading curve	10 $\frac{ft}{psi^B * s}$	115 $\frac{m}{MPa^B * s}$
C	Uniaxial strain pore pressure buildup coefficient (loading efficiency)	0.8	0.8
$\frac{\Delta \sigma_v}{\Delta Z}$	Lithostatic gradient	1.04 $\frac{psi}{ft}$	23.53 $\frac{KPa}{m}$
$\frac{\Delta u_h}{\Delta Z}$	Hydrostatic pore pressure gradient	0.44 $\frac{psi}{ft}$	9.95 $\frac{KPa}{m}$

Table 2.3: Input parameters for pore pressure prediction model. The parameters are constrained in the calibration well.

I pick the mudrock depths every 30~60’ (9~18 m). To interpret the mudrock intervals, I use the gamma-ray (GR; Figure 2.4A) and the bulk density (RHOB; Figure 2.4C) log data. I find that a high gamma-ray (150+ API) coupled with a bulk density near

2.45 g/cc provides consistent mudrock picks. I record the sonic velocity at these depths (Figure 2.4D) and smooth them by applying a moving average of 11-points (blue dots in Figure 2.4E are the smoothed mudrock velocities in the drained interval; red dots in Figure 2.4E are the smoothed mudrock velocities in the undrained interval). This removes any noise from borehole effects or small lithologic changes.

I next determine the A and B parameters (Eq. 2.3). These define the form of the velocity-effective stress curve for normal compaction. The typical approach is to fit a regression through these data in an interval that has not undergone unloading and where the pore pressures are known. However, if the rocks have been unloaded, A and B must be determined indirectly. I use Heppard and Ebrom's (2010) model of velocity versus depth in the drained section to infer $A = 14\ \frac{ft}{psi^{B*s}}$ ($161\ \frac{m}{MPa^{B*s}}$) and $B = 0.730$ for illitic mudrocks, and $A = 14\ \frac{ft}{psi^{B*s}}$ ($132\ \frac{m}{MPa^{B*s}}$) and $B = 0.690$ for smectitic mudrocks. I interpret the mudrock type by cross-plotting the photoelectric factor (PEF) values against the thorium and potassium ratios of the spectral GR log on an interpretation chart (Schlumberger, 2005). I find that the dominant clay is illite and I use values of $A = 14\ \frac{ft}{psi^{B*s}}$ ($161\ \frac{m}{MPa^{B*s}}$) and $B = 0.730$.

I then constrain the U parameter. I re-arrange Eq. 2.12 to solve for U at every picked mudrock depth in the drained interval:

$$U = \frac{\ln(\sigma'_v) - \ln(\sigma'_{p,D})}{\ln\left(\left(\frac{V - V_W}{A}\right)^{\frac{1}{B}}\right) - \ln(\sigma'_{p,D})}. \qquad (2.17)$$

σ'_v is calculated with depth by assuming hydrostatic pressure. The preconsolidation stress is computed from Eq. 2.8 with a ΔH of 6,890' (2,100 m). The remaining parameters are provided in Table 2.3. V is the smoothed mudrock velocity at depth. The blue curves in Figure 2.5 shows an unloading curve fit to every picked mudrock in the drained interval

of my calibration well. I calculate the average U value to be 10 $\frac{ft}{psi^{B}{}_{*s}}$ (115 $\frac{m}{MPa^{B}{}_{*s}}$) with a standard deviation of 5.

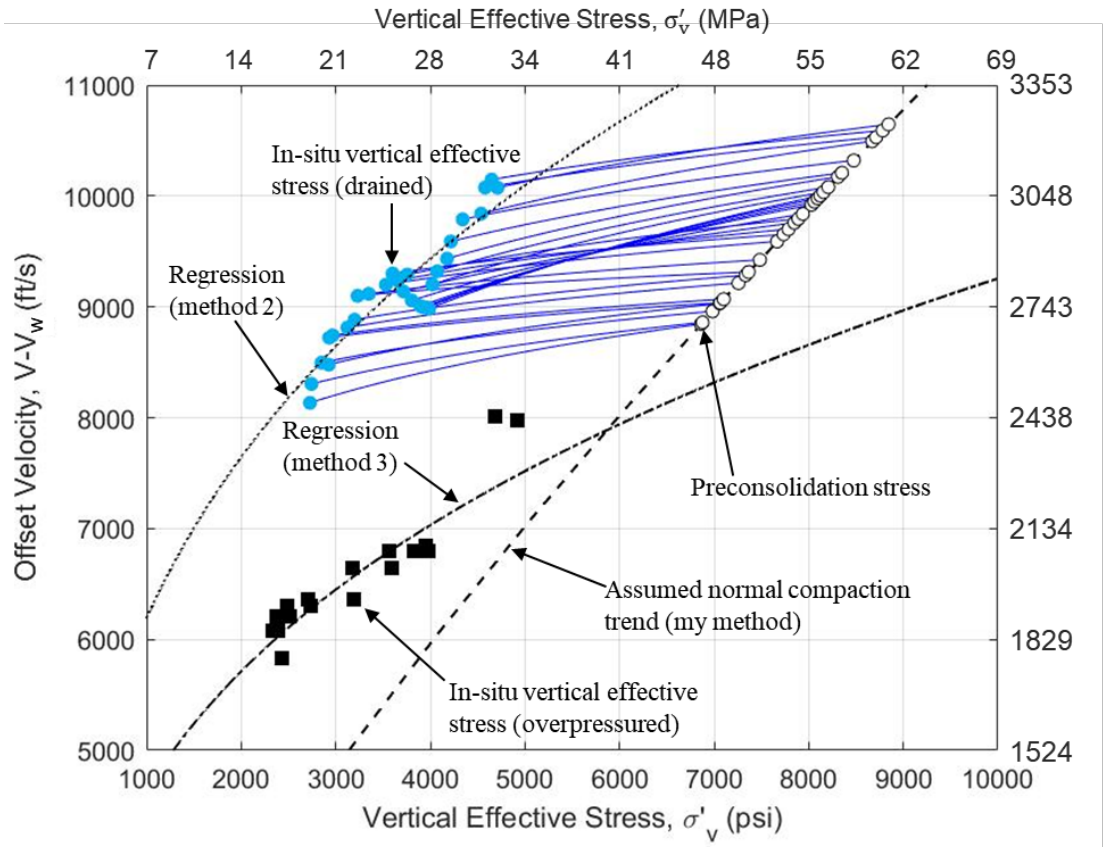

Figure 2.5: Velocity-effective stress relationships. Data is from calibration well. Unloading curves (dark blue line) are fit between every in-situ vertical effective stress assumed to be drained (blue dots) and corresponding preconsolidation stress (white dots) using Eq. 2.17 (my method). A, B, and U are provided in Table 2.3. Normal compaction trend is fit to blue dots (black dotted line; method 2). This yields an A value of 758 $\frac{ft}{psi^{B}{}_{*s}}$ (1049 $\frac{m}{MPa^{B}{}_{*s}}$) and a B value of 0.304 from a power regression (Eq. 2.1). Normal compaction trend is fit to measured in-situ vertical effective stresses (black squares), which are overpressured (dash-dotted line; method 3. This yields an A value of 584 $\frac{ft}{psi^{B}{}_{*s}}$ (792 $\frac{m}{MPa^{B}{}_{*s}}$) and a B value of 0.300 from a power regression (dashed black curve; Eq. 2.1).

The last step is to constrain the isotropic pore pressure buildup coefficient C. My objective is to capture the undrained change in pore pressure due to a change in vertical stress with a single value for my mudrocks. I apply Eq. 2.13 to solve for C at every depth where there is a measured pore pressure (black squares in Figure 2.4) in the undrained section. The velocity at that depth is calculated as the averaged value of the nearest picked and smoothed mudrocks bounding the measured pore pressure. The remaining parameters are provided in Table 2.3. I find C to be 0.8 with a standard deviation of 0.06.

I verify my calibrated model (Eq. 2.12 for drained mudrock and Eq. 2.13 for undrained mudrock) by predicting the amount of erosion and the pressure in the hydrostatic (drained) section and the overpressured (undrained) section of my calibration well (Figure 2.4). I use the smoothed velocities (blue (drained) and red (undrained) in Figure 2.4E) to predict pressure in the drained section (Equations 2.12) and the undrained section (Equations 2.13). In the drained section, the predicted pressures (blue dots in Figure 2.4G) lie along the hydrostatic pressure line (blue line in Figure 2.4G). I also plot the erosion thickness calculated from Eq. 2.12 for each velocity point as a function of depth (Figure 2.6A). The eroded thickness is fairly constant and equal to 6,765’ (2,062) to a depth of 8,000’ (2,438 m), which is where I initially interpreted the base of the drained interval to be. This confirms my original assumption and suggests an approach for determining the depth of the drained interval.

In the overpressured section, my modeled pressures (orange dots in Figure 2.4G) fit well with the measured overpressures (black squares in Figure 2.4G) assuming a C value of 0.8. In the discussion section, I address why the top of the undrained section has predicted pressures less than the hydrostatic pressure.

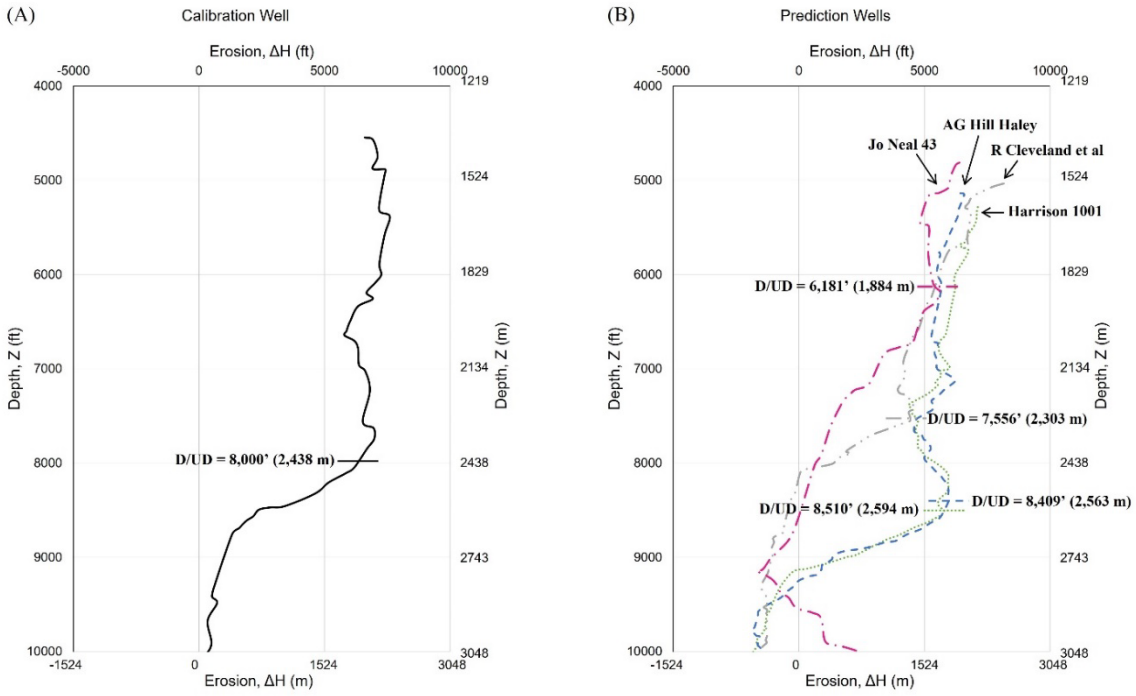

Figure 2.6: Estimated erosion in all wells. Depth versus erosion used to determine the drained-undrained (D/UD) boundary and the average amount of erosion (ΔH) for each well. ΔH is calculated from Eq. 2.12. (A) Calibration well. D/UD boundary is 8,000' (2,438 m)) and average ΔH is 6,890' (2,100 m). (B) Prediction wells. For the Harrison 1001 well (gray dotted line), D/UD boundary is 8,510' (2,594 m) and average ΔH is 5,755' (1,754 m). For the AG Hill Haley well (blue dashed line), D/UD boundary is 8,409' (2,563 m) and average ΔH is 5,558' (1,694 m). For the R Cleveland et al well (gray dash-dotted-dotted line), D/UD boundary is 7,556' (2,303) and average ΔH is 5,518' (1,682 m). For the Jo Neal 43 well (magenta dash-dotted line), D/UD boundary is 6,181' (1,884 m) and average ΔH is 5,667' (1,727 m).

2.4.3 Model Prediction

I apply my model to predict the amount of erosion and the pore pressure in four wells spanning the eastern portion of the Delaware Basin (yellow dots, Figure 2.2). I first pick the mudrock velocities as described in the calibration section. I determine the drained-undrained boundary by plotting the erosion thickness (ΔH) calculated from Eq. 2.12 for each velocity point as a function of depth (Figure 2.6 B-E) and; A, B, and U are from the

calibration well (Table 2.3). The point at which ΔH is no longer approximately constant is my inferred drained-undrained boundary. In the Harrison 1001, AG Hill Haley, and Jo Neal 43 wells, the eroded thickness is fairly constant in the shallow section. I interpret this to be the drained interval. However, there is greater variability in eroded thickness in the R Cleveland et al well. I interpret the depth of the drained-undrained boundary with less confidence in this well.

Once the depth of the drained interval is determined, I calculate the average eroded thickness for each well (Figure 2.6 B-E). I check my result in the drained section (Eq. 2.12 with the smoothed mudrock velocities), as I did in the calibration well, by demonstrating that the drained predicted pore pressures (blue dots in Figure 2.7) track the general trend of the hydrostatic pressure gradient (blue curve in Figure 2.7).

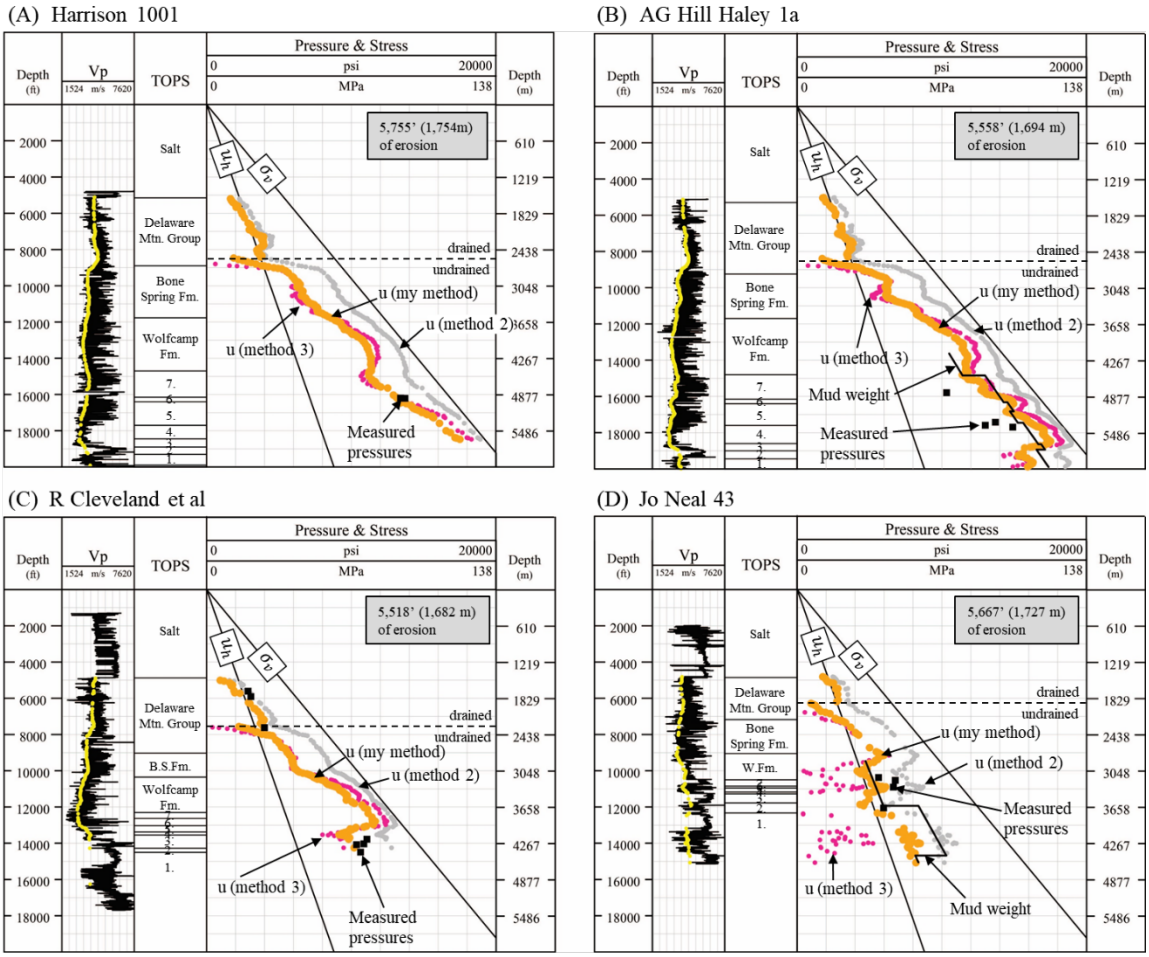

Figure 2.7: Pore pressure prediction results. In the 'Vp' (compressional velocity) track, yellow dots are smoothed velocities picked from mudrocks. In the 'Pressure & Stress' track, orange dots are predicted pressures from my method (Equations 2.12 and 2.13). Gray dots are the predicted pressures from method 2. Magenta dots are the predicted pressures from method 3. Black squares represent pore pressures interpreted from drill-stem tests (DSTs). (A) Harrison 1001 well. (B) AG Hill Haley 1a well. (C) R Cleveland et al 2 well. (D) Jo Neal 43 well. In 'TOPS' track, B.S.Fm. is Bone Spring Formation, W.Fm. is Wolfcamp Formation, 6 is Cisco, 5 is Strawn, 4 is Atoka, 3 is Morrow, 2 is Barnett, 1 is Mississippian).

I then predict pore pressure in the undrained section (Eq. 2.13 with the smoothed mudrock velocities) for each well. A, B, U, and C are the values constrained in the calibration well (Table 2.3) and ΔH is provided in Figure 2.6. I assume the lithostatic and

hydrostatic gradients derived in the calibration well (Table 2.3). The final predicted pore pressures are shown in Figure 2.7 (orange dots).

2.5 DISCUSSION

2.5.1 Estimation of Erosion

I find a similar amount of erosion in the four wells: the minimum amount is 5,518' (1,682 m), the maximum amount is 5,755' (1,754 m), and the average is 5,625' (1,715 m) (Figure 2.7). A plot of the predicted eroded thickness at each depth (Figure 2.6B) shows that the predicted thickness is fairly constant in the interpreted drained section. However, in all the wells, there is a slight decrease in predicted eroded thickness with depth (Figure 2.6B), particularly in the R Cleveland et al well.

The predicted pressure within the drained interval is generally hydrostatic but appears to slightly underpredict the hydrostatic pressure in the shallow section and overpredict it in the deep section (Figure 2.7). My method performs the worst predicting hydrostatic pressures in the R Cleveland et al well (Figure 2.6D). I note that the mis-prediction directly results from the fact that the eroded thickness (Figure 2.6B) is not constant in the inferred section. This may suggest that the appropriate compaction parameters (A and B) are varying between the wells.

2.5.2 Comparison of Pressure Prediction Approaches

I compare my method to the approach of fitting a normal compaction trend to the hydrostatic section ('method 2') and the approach of fitting the normal compaction trend to the overpressured section ('method 3'). In method 2, I calibrate Eq. 2.1 to the observed velocity-vertical effective stress relationship in the drained section. This is illustrated in Figure 2.5 (dotted line) and yields an A value of 758 $\frac{ft}{psi^B * s}$ (1049 $\frac{m}{MPa^B * s}$) and a B value of

0.304 (Eq. 2.1). In method 2, I calibrate Eq. 2.1 to the measured effective stresses of the overpressured interval (dash-dotted curve Figure 2.5). This is illustrated in Figure 2.5 (dash-dotted line) and yields an A value of 584 $\frac{ft}{psi^{B}*s}$ (792 $\frac{m}{MPa^{B}*s}$) and a B value of 0.300 (Eq. 2.1).

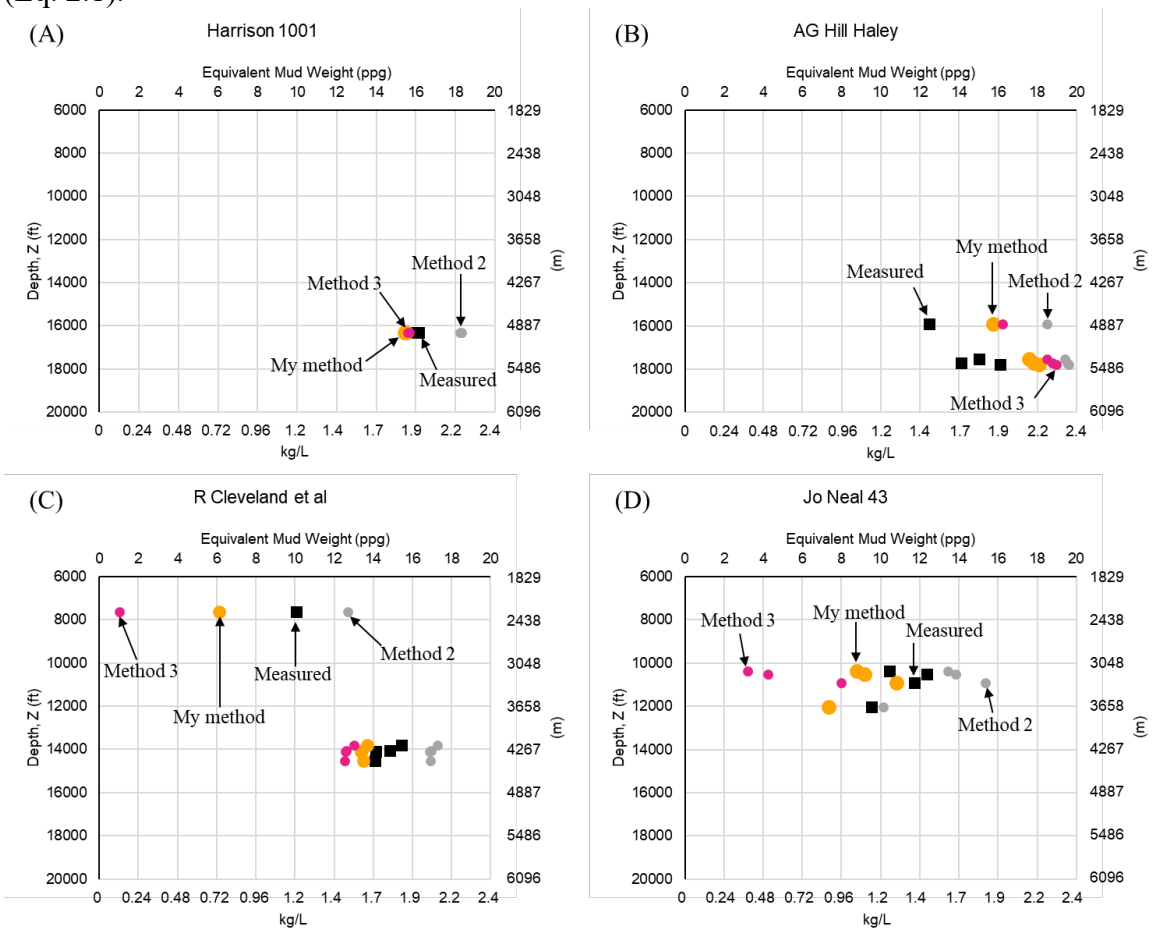

Figure 2.8: Prediction comparison. A comparison of predicted pressures to measured pressures for my method, methods 2, and method 3 for the four prediction wells (A. Harrison 1001; B. AG Hill Haley; C. R Cleveland et al; and D. Jo Neal 43). Pore pressures have been converted to equivalent mud weight (u[psi]/0.052/TVDSS[ft]). Orange dots represent my method; gray dots represent method 2; magenta dots represent method 3; and black squares represent measured pressures.

Method Compared to Measured	Average Difference $[\boldsymbol{u}\,(\boldsymbol{measured}) - \boldsymbol{u}\,(\boldsymbol{method})]$	Standard Deviation $[\boldsymbol{u}\,(\boldsymbol{measured})$ & $\boldsymbol{u}\,(\boldsymbol{method})]$
My method	0.4 ppg (0.5 kg/L)	2.3 ppg (0.28 kg/L)
Method 2	-3.0 ppg (-0.36 kg/L)	1.4 ppg (0.17 kg/L)
Method 3	2.5 ppg (0.30 kg/L)	5.5 ppg (0.66 kg/L)

Table 2.4: Prediction comparison tabulated. Comparison of DST (measured) pore pressures against my method, method 2, and method 3.

In Figure 2.8, I compare the three methods to the measured pressures (black squares). These are the final hydrostatic pressures recorded from drill-stem tests (DSTs) and are assumed to represent the true formation pressures. My method (orange dots) generally predicts pressures closer to the measured pore pressures. The average difference between my predictions and the measured is 0.4 ppg (0.05 kg/L) with a standard deviation of 2.3 ppg (0.28 kg/L) (Table 2.4). For method 3, the average difference between my predictions and the measured pressures is 2.5 ppg (0.30 kg/L) with a standard deviation of 5.5 ppg (0.66 kg/L). However, method 3 predicts similar values to the measured in the Harrison 1001, AG Hill Haley 1a, and R Cleveland et al wells. In these three wells, the average misfit is 0.3 ppg (0.04 kg/L) with a standard deviation of 3.9. Method 2 is consistently the most unsuccessful with an average misfit of -3.0 ppg (-0.36 kg/L) and with a standard deviation of 1.4 ppg (0.17 kg/L) (Table 2.4).

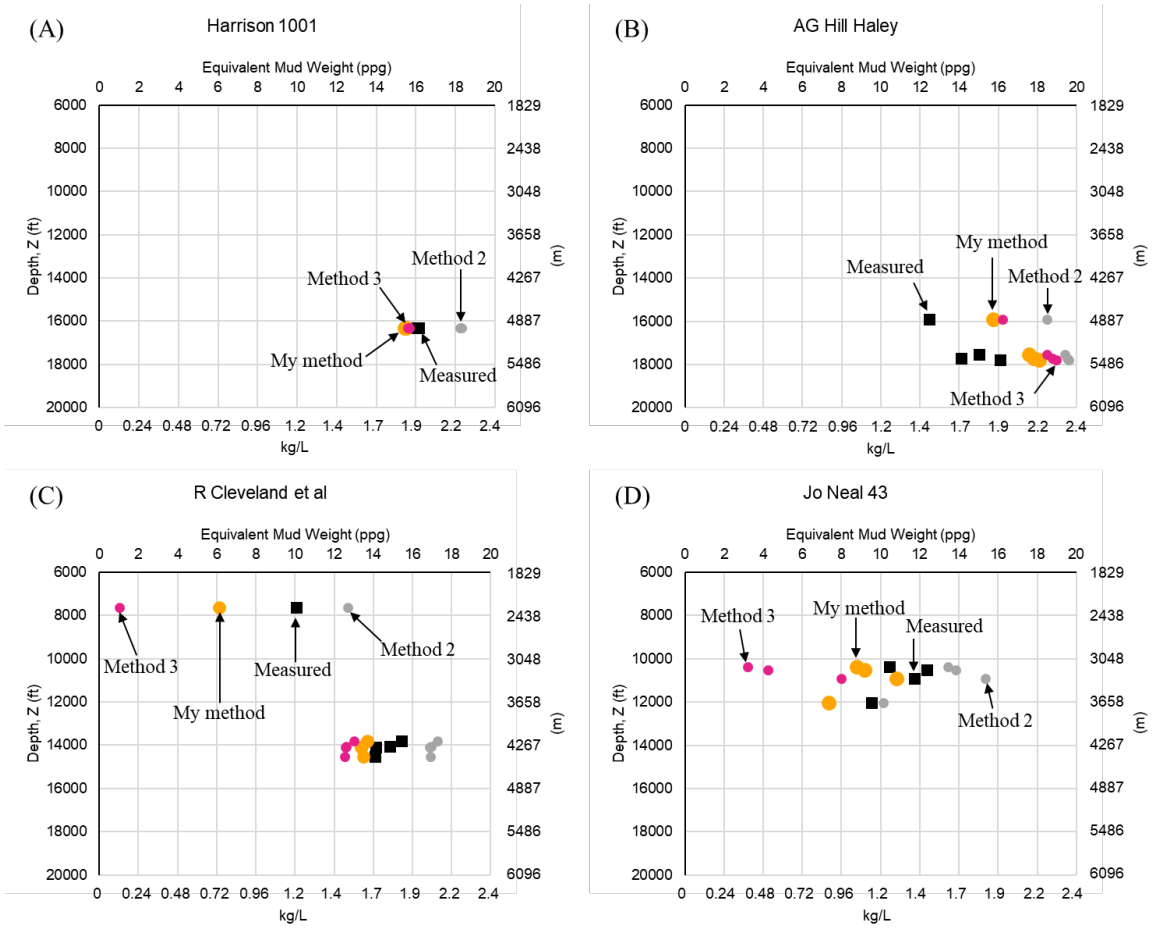

Figure 2.9: Prediction comparison in ppg. The predicted equivalent mud weight of my method versus the predicted equivalent mud weight for all methods. The orange line is my method is cross plotted against itself. Method 2 predicts higher pressures than my method. Relative to my method, method 3 predicts lower pressures at low overpressures (e.g., mud weight less than 10 ppg (1.20 kg/L)) and higher pressures at higher relative overpressures (e.g., mud weight greater than ~12 ppg (1.44 kg/L)).

Figure 2.9 compares the three methods to each other as a function of the predicted pressure gradient with my method. Once again, method 2 (gray dots) predicts higher pressures gradients in all cases. Relative to my method, method 3 predicts lower pressures at low overpressures (e.g., mud weight less than 10 ppg (1.20 kg/L)) and higher pressures at higher relative overpressures (e.g., mud weight greater than ~12 ppg (1.44 kg/L)).

2.5.3 Sub-hydrostatic Pressure Predicted in Shallow Section of Undrained Interval

My method predicts pressures that are less than the hydrostatic pressure at the top of the undrained interval (dashed line in Figure 2.4G and Figure 2.7). I use a forward model to illustrate why underpressures are possible (Figure 2.10). Consider a rock that is initially normally compacted (lies along its normal compaction trend and is overpressured at point A in Figure 2.10A. I then impose 10,000' (3,048 m) of erosion, which results in a decrease in total vertical stress of 10,400 psi (72 MPa). I assume that the rock is undrained and compute the change in pore pressure as a function of the undrained pore pressure buildup coefficient C through Eq. 2.9 (I assume C = 0.8, the same value I constrained in my calibration well (Table 2.3)). As a result, the depth and pressure shift from point A to point B in Figure 2.10A. At this depth, the pore pressure is 1,520 psi (10 MPa) less than the hydrostatic pressure (u_h). With this shift in pressure, the effective stress and velocity also decrease from point A to point B along the unloading curve (Figure 2.10B).

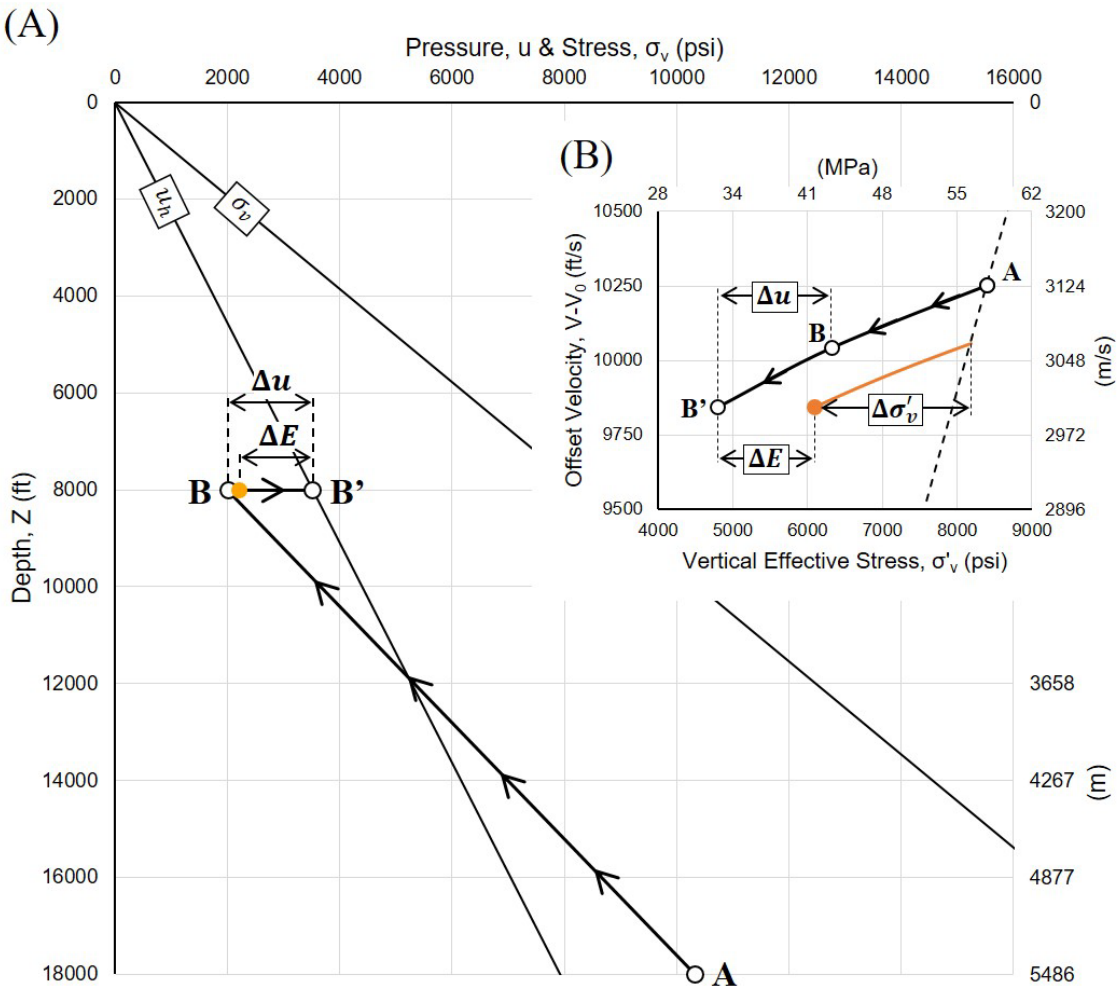

Figure 2.10: Forward model versus my method. White dots represent forward model. Orange dot represents pressure predicted from my method using the velocity of the forward model at point B'. (A) Loading and unloading path in depth versus pressure and stress plot. (B) Loading and unloading path in vertical effective stress versus offset velocity plot. $\Delta\sigma_v'$ is computed from Eq. 2.10.

With time, I would expect these underpressures to converge back to the hydrostatic pressure, ultimately shifting from point B to point B' in Figure 2.10A. When this occurs, further unloading will transpire, and my forward model predicts that the effective stress and velocity will decrease to point B' in Figure 10B.

In fact, I do not know whether underpressures are present and I have no data to suggest it. However, the basic physical mechanism of undrained loading causing underpressures in the manner I describe is well understood. Neuzil and Pollock (1983) present a very similar approach to describe the effect of unloading, although they assume a C equal to 1.0. Perhaps the most common occurrence of underpressures is in the Alberta foreland where large scale erosion adjacent to the Rockies has resulted in a significant amount of unloading and underpressures in the underlying reservoirs trapped by low permeability rocks (Bachu and Underschultz, 1995; Bekele et al., 2003).

I next use the velocity given by the forward model at point B', where pore pressure is hydrostatic, to predict pore pressure with my method. The forward model and my method share the same parameters (Table 2.3); however, my model predicts a pressure that is less than hydrostatic and only slightly greater than the undrained pressures (orange circle, Figure 2.10A). Thus, if the unloaded rock was originally sub-hydrostatic, then drained to hydrostatic, my model would still predict a sub-hydrostatic pore pressure. The error between the forward model and my method is ΔE (Figure 2.10 A and B). The reason for this is subtle. In my method, the change in effective stress ($\Delta\sigma_v'$) due to unloading in the undrained section is fixed by Eq. 2.13. I determine the present effective stress by unloading a distance σ'_v from the normal compaction curve such that the end point is the calculated velocity (Figure 2.10B). This places us at an effective stress only slight less than the undrained effective stress (point B in Figure 2.10B). As a result, the predicted pressure is only slightly greater than the undrained, sub-hydrostatic pressure. These results emphasize that my pore pressure prediction method cannot capture the effects of pore pressure dissipation from sub-hydrostatic pressures. I have also explored whether my model captures the effect of dissipation of overpressure after unloading. I find that this depends on both the amount of dissipation and the amount of unloading that has occurred.

2.5.4 Comparison of Pressure Prediction Models

At first glance, method 3 appears to work nearly as well as my method (Figure 2.8). However, as discussed, my method has a significantly lower average error (Figure 2.8, Table 2.4). In addition, as illustrated, there is a systematic misfit of this approach relative to my approach as a function of the degree of overpressure (Figure 2.9).

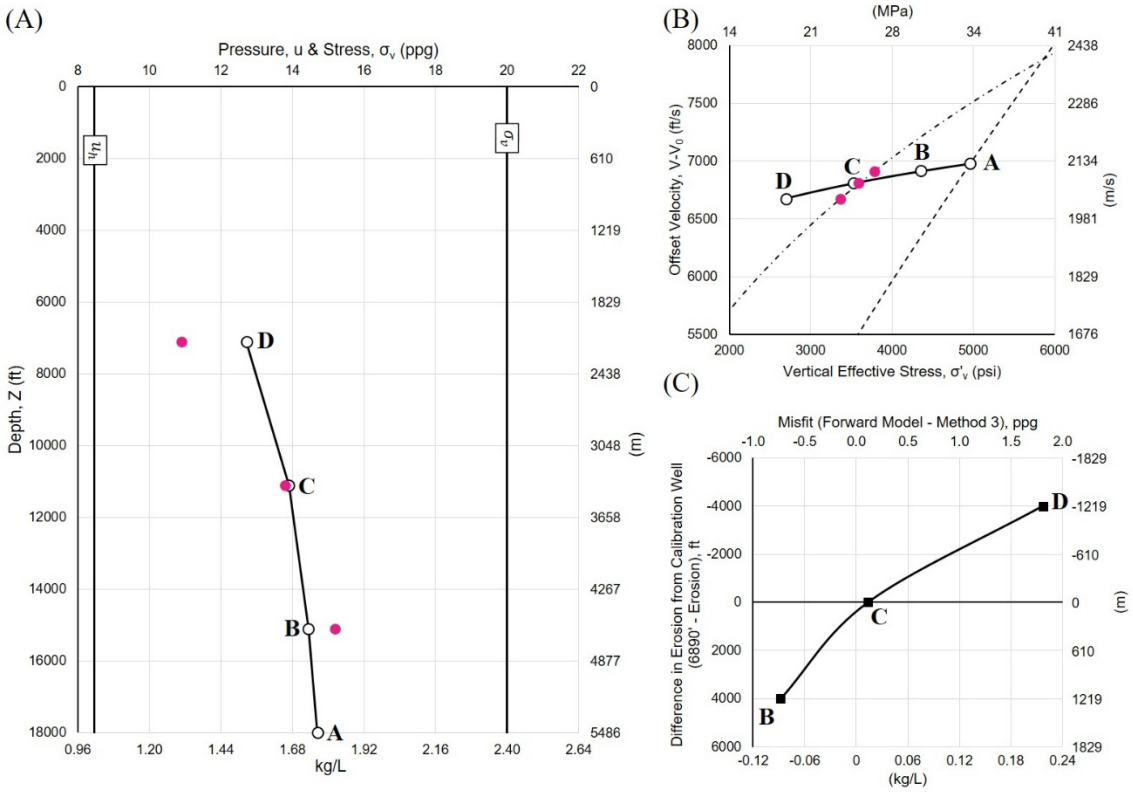

Figure 2.11: Forward model versus method 3. White dots represent forward model (my method). Magenta dots represent pressures predicted from method 3. (A) Loading and unloading path in depth versus pressure and stress plot. (B) Loading and unloading path in vertical effective stress versus offset velocity plot. (C) Pressure difference between my method and method 3 due to various amounts of erosional unloading.

I, once again, use a forward model to understand this behavior (illustrated in Figure 2.11). My starting point is my initial calibration wherein A, B, U, and C are determined at a well with 6,890' (2,100 m) of erosion (Table 2.3). I now consider a new well. At that location, consider a rock that is initially normally compacted (point A in Figure 2.11B) and

is overpressured (point A in Figure 2.11A). I model the effect of various amounts of erosion. At point B, erosion is 2,890' (881 m); at point C, erosion is 6,890' (2,100 m; equivalent to the amount of erosion at my calibration); at point D, erosion is 10,890' (3,319 m). I calculate the velocity at points B, C, and D (Figure 2.11B). I then use these values for velocity and predict pressures with the two approaches.

Not surprisingly, where the prediction well has the same amount of erosion as the calibration well (point C in Figure 2.11), both methods predict nearly the exact same pressure. However, if there is less erosion in the prediction well than the calibration well, then method 3 predicts higher pressures than my method (point B in Figure 2.11). In contrast, if there is more erosion in the prediction well than the calibration well, then my method predicts higher pressures than method 3 (point D in Figure 2.11). I would suggest that my method will be much more effective where there is significant variation in the eroded thickness. Unfortunately, I do not have significant variation in the eroded thickness at the wells I have available to use.

2.5.5 Model Limitations

My method assumes that velocity varies only as a function of the vertical effective stress. For normally compacted rocks under uniaxial strain, the ratio of horizontal effective stress to vertical effective stress is approximately constant; this allows one to use the vertical effective stress as a proxy for the general stress state. However, it is well understood that the ratio of horizontal to vertical effective stress rises sharply during unloading of elastoplastic material (Casey et al., 2015) . Thus, during unloading, I might expect the mean stress to more rapidly, and this will impact the velocity response. Future work could account for this unloading effect. Second, I have assumed that deformation is assumed to only occur uniaxially. For non-uniaxial basins, the changes in mean and shear

stresses must be considered. This has been documented by Heidari et al. (2018), Lockhart (2018), and Nikolinakou et al. (2016) in the Gulf of Mexico, but not in an unloaded basin.

I have assumed that the normal compaction trend is similar over the entire depth of the basin. This assumes that shallow and deeper mudrocks have the same velocity-effective stress behavior. Whether this is, in fact, the case is not known. In addition, if the compaction parameters vary across the basin, then this model will not be effective.

Finally, my method cannot fully account for the effects of dissipation after unloading has occurred. In cases where the dissipation results in a decrease in effective stress, my method will predict lower pressures than the in-situ pressure (e.g., Figure 2.10). However, in cases where there is an increase in effective stress after unloading (e.g., the overpressure has dissipated) my method will predict somewhat higher pressures than the in-situ pressures.

2.6 SUMMARY

Pore pressure prediction is challenging in unconventional basins due to the unloading that is caused by erosion. I have presented a systematic approach to account for the effects of erosion in pore pressure prediction. My approach includes the hysteresis that occurs in the velocity-effective stress relationship during unloading. In addition, for the first time, it considers the effect of unloading on the pore pressure by accounting for the pore pressure response due to a decrease in overburden stress under undrained conditions.

Once calibrated, my model can be used to estimate the amount of erosion that has occurred in a well and can predict the pore pressure throughout the entire well. My technique can be applied to any basin that has been unloaded. I validated my approach in the highly unloaded Delaware Basin in four prediction wells that span the eastern portion of the basin. Overall, my workflow provides a reliable and easy method to predict pore

pressures in unloaded basins. In addition to improving the safety and efficiency of drilling, this approach has the potential to provide further insight into important subsurface processes where the pore pressure is affected by unloading. I illustrated the approach on four wells. My method is shown to be more precise than previous methods that do not consider the effects of either hysteresis or pore pressure responses to unloading. I show that my model will be most effective in prediction where there is strong variation in the amount of erosion.

2.7 ACKNOWLEDGMENTS

The project was funded by the University of Texas at Austin (U.T.) Jackson School of Geosciences. The authors received additional support from the U.T. GeoFluids consortium. U.T. GeoFluids is supported by the following companies: BHP, BP, Chevron, Conoco-Phillips, Hess, Oxy, Petrobras, and Shell.

Symbol	Name	Dimensions	Units (Imperial)	Units (SI)
A	Parameter in velocity-vertical effective stress equation	$\frac{L^{B+1}T^{2B-1}}{M^B}$	$\frac{ft}{psi^B * s}$	$\frac{m}{MPa^B * s}$
B	Parameter in velocity-vertical effective stress equation	–	–	–
C	Uniaxial strain pore pressure buildup coefficient (loading efficiency)	–	–	–
c_f	Fluid compressibility	$\frac{L^2T}{M}$	$\frac{1}{psi}$	$\frac{1}{MPa}$
c_s	Solid grain compressibility	$\frac{L^2T}{M}$	$\frac{1}{psi}$	$\frac{1}{MPa}$
g	Acceleration of gravity	$\frac{L}{T^2}$	$\frac{ft}{s^2}$	$\frac{m}{s^2}$
ΔH	Thickness of eroded rock	L	ft	m
λ	Parameter in porosity-depth equation	–	–	
m_v	Coefficient of volume compressibility	$\frac{LT^2}{M}$	$\frac{1}{psi}$	$\frac{1}{MPa}$
n	Porosity	–	–	–
n_0	Surface porosity	–	–	–
ρ_f	Fluid density	$\frac{M}{L^3}$	$\frac{g}{cm^3}$	$\frac{g}{cm^3}$
ρ_b	Bulk density	$\frac{M}{L^3}$	$\frac{g}{cm^3}$	$\frac{g}{cm^3}$
ρ_m	Matrix density	$\frac{M}{L^3}$	$\frac{g}{cm^3}$	$\frac{g}{cm^3}$
σ_v	Vertical total stress	$\frac{M}{LT^2}$	psi	MPa
$\sigma_v^{'}$	Vertical effective stress	$\frac{M}{LT^2}$	psi	MPa
$\sigma_p^{'}$	Preconsolidation stress	$\frac{M}{LT^2}$	psi	MPa
$\sigma_{p,D}^{'}$	Drained preconsolidation stress	$\frac{M}{LT^2}$	psi	MPa
$\sigma_{p,UD}^{'}$	Undrained preconsolidation stress	$\frac{M}{LT^2}$	psi	MPa
u	Pore pressure	$\frac{M}{LT^2}$	psi	MPa
U	Slope of the velocity-effective stress unloading curve	$\frac{L^{B+1}T^{2B-1}}{M^B}$	$\frac{ft}{psi^B * s}$	$\frac{m}{MPa^B * s}$

u_h	Hydrostatic pressure	$\frac{M}{LT^2}$	psi	MPa
V	Velocity	$\frac{L}{T}$	$\frac{ft}{s}$	$\frac{m}{s}$
V_w	Velocity of sound in water	$\frac{L}{T}$	$\frac{ft}{s}$	$\frac{m}{s}$
Z	Depth	L	ft	m

Table 2.5: Nomenclature. This table provides a list of the symbols, names, dimensions, and units.

Chapter 3: Skempton's Pore Pressure Coefficient B in the Wolfcamp Fm., Delaware Basin

3.1 ABSTRACT

Pore pressure buildup coefficients describe changes in pore pressure due to changes in stress for undrained rock. They are a critical parameter for predicting pore pressure in basins that have been mechanically unloaded; however, determining these parameters can be challenging and time-consuming. Traditionally, these parameters are experimentally measured in undrained triaxial tests. I both compute and experimentally measure the Skempton's pore pressure buildup coefficient B on Wolfcamp mudrocks using data from a well located in the Delaware Basin. The computed Skempton's B coefficients ("$B_{comp.}$") are determined from the rock's bulk compressibility, solid aggregate phase compressibility, fluid compressibility, and porosity, yielding $B_{comp.}$ = 0.32, 0.31, and 0.39. The experimentally measured and corrected Skempton's B coefficients ($B_{corr.}$) are determined by superimposing an incremental change in confining stress on a pre-existing state of confining stress and pore pressure, resulting in $B_{corr.}$ = 0.31, 0.30, 0.42 at the same respective depths as $B_{comp.}$. Whereas both techniques yield comparable results, I demonstrate that experimental measurements are challenging and laborious, and the primary challenge with the experimental measurements is achieving truly undrained conditions. Thus, computation of Skempton's B using petrophysical data provides a more cost-effective and efficient approach compared to the traditional way of determining this coefficient in undrained triaxial tests.

3.2 INTRODUCTION

Abnormal pressures are observed in most basins worldwide (Law and Spencer, 1998). Many of these basins, particularly unconventional ones, have experienced mechanical unloading due to erosion (Xia et al., 2013), and this can have a significant impact on pore pressure. Understanding these changes is essential for explaining and predicting the subsurface pressures that exist in such basins today (Bowers, 1995).

The undrained change in pore pressure due to a change in isotropic stress is defined by Skempton's pore pressure buildup coefficient B (Skempton, 1954):

$$\Delta u = B\Delta\sigma_m, \tag{3.1}$$

where u is pore pressure and σ_m is mean total stress.

Bishop (1976) derived a formula to express Skempton's B coefficient in terms of the porosity and relative compressibilities:

$$B = \frac{1}{1+\mathrm{n}\left(\frac{\mathrm{c_f}-c_s}{c_b-c_s}\right)}, \tag{3.2}$$

where n is porosity, c_f is fluid compressibility, c_b is isotropic bulk compressibility of the rock skeleton, and c_s is compressibility of the solid aggregate phase. Eq. 3.2 assumes the rock has interconnected pores, a statistically random pore space distribution within the skeleton, an elastic and isotropic solid aggregate phase, bulk behavior exhibiting elastic isotropic properties under boundary stress changes with no change in pore pressure, and a linearly compressible pore fluid.

Skempton's B coefficient has application both experimentally and geologically. Experimentally, it is regularly used to assess sample saturation (Makhnenko and Labuz, 2013; Wissa, 1969). Others have used Skempton's B to understand changes in pore pressure related to glaciation (Neuzil and Provost, 2014) and glacial retreat (Corbet and Bethke, 1992). More recent work has focused on experimental measurements of Skempton's B to understand the coupling between poromechanical behavior and fluid flow

(Kim and Makhnenko, 2020), the behavior of injection-induced seismicity (Bondarenko et al., 2022), and to characterize reservoirs targeted for CO_2 injection (Kim and Makhnenko, 2023; Kim and Makhnenko, 2022).

I present an effective medium petrophysical approach to compute Skempton's B coefficient in unconventional mudrocks with erosional unloading. This offers a more cost-effective and efficient way to determine Skempton's B compared to traditional experimental methods, which are challenging, time-consuming, and require expensive testing equipment. Moreover, it is not always possible to obtain test samples on which to perform B measurements.

I begin with my approach using data from a well located in the Delaware Basin. I then compare my results with experimental measurements I performed on the mudrocks acquired from the same depths I petrophysically computed Skempton's B. I end by discussing the process for comparing the computational results of Skempton's B against the experimental measurments. Overall, my work shows the efficacy of my effective medium computational approach using petrophysical data and its potential application for predicting and understanding the pore pressure in unconventional basins with erosional unloading.

3.3 Materials, Methods & Results

3.3.1 Description of Test Samples

The rocks I present in this paper are from a well (Figure 3.1) located in the Delaware Basin in Pecos County, Texas. Approximately 430 feet of core was recovered that comprise the Lower 3rd Bone Spring, Wolfcamp A, and Wolfcamp B. The core, originally extracted with a diameter of 4 inches, was cut along its axis into two distinct sections. The smaller section constitutes approximately one-third of the core axis; this section is referred to as

the “archive” portion and was reserved for visual examination. The remaining two-thirds, termed “core butt,” was specifically allocated for sampling purposes.

The lithofacies of the core were independently determined by a commercial lab. The rock predominantly consists of silty mudstone, siltstone, argillaceous siltstone, and limestone. The silty mudstones range from calcareous to non-calcareous, organic-rich to organic-lean (when bioturbated), and locally siliceous to dolomitic. They contain abundant agglutinated foraminifera, algal cysts, and pyrite. The argillaceous siltstones are calcareous to non-calcareous, cyclically interbedded, commonly bioturbated, and locally exhibit soft sediment deformation features. The limestones are composed of matrix-supported wackestone and floatstone, and grain-supported packstone, rudstone, and grainstone of deep water, sediment gravity-flow origin. These lithofacies are similar to the descriptions of Ramiro-Ramirez et al. (2024) for the Wolfcamp interval.

In this study, three Wolfcamp A test samples were extracted from the core. Each of the test samples is an organic-rich silty mudstone. Within the depth interval of the test samples, the overburden gradient is 24.2 KPa/m, the total horizontal stress gradient is 17.2 KPa/m, and the pore pressure gradient is 16.5 KPa/m. A detailed discussion on the determination of these gradients is presented below.

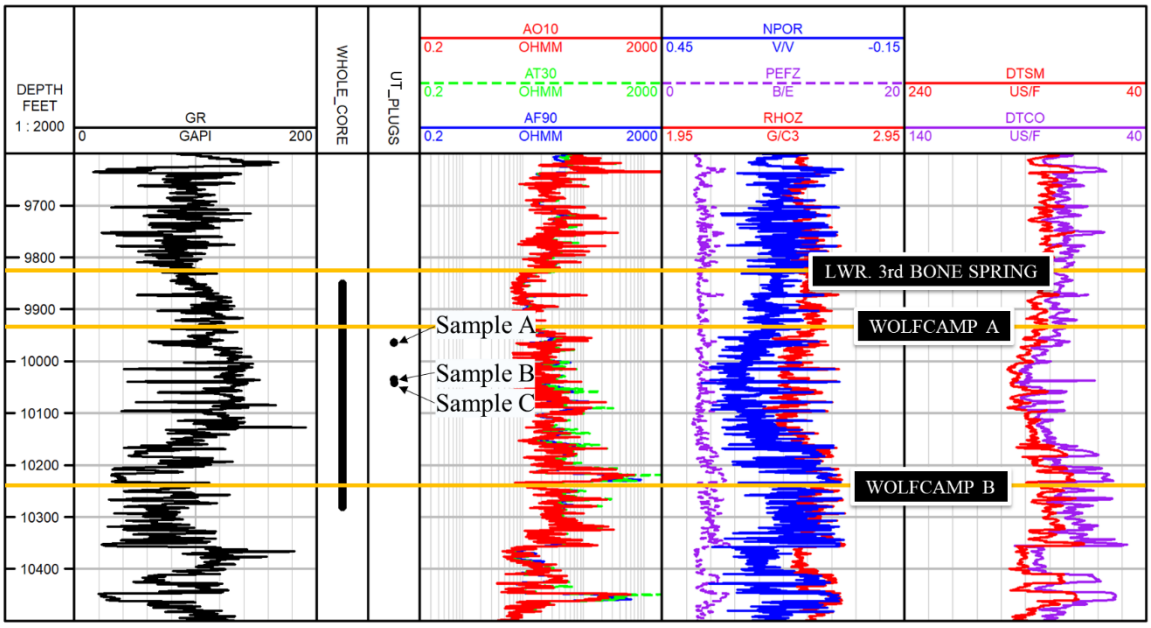

Figure 3.1: Wireline logs with cored interval and test sample locations. All samples were obtained from the Wolfcamp A.

3.3.2 Computation of Skempton's *B* Coefficient: Method & Results

I compute Skempton's B from Eq. 3.2, hereinafter referred to as "$B_{comp.}$," using an effective medium approach with petrophysical data commonly available. I first estimate bulk compressibility (c_b) from the wireline sonic velocities and the wireline bulk density using the following relation (Fjaer et al., 2008):

$$c_b = \frac{1}{\rho_b\left(V_p^2 - \frac{4}{3}V_s^2\right)}, \tag{3.3}$$

where V_p is the compressional wave, V_s is the shear wave, and ρ_b is the bulk density. The resulting c_b determined for each sample is listed in Table 3.1.

Eq. 3.3, derived for a linearly elastic, isotropic, and homogenous material, is the dynamic c_b, and it is different than its static counterpart. Normally, dynamic compressibilities are lower than static ones, and thus represent a lower bound (Zimmer, 2004). A discussion of this parameter is provided at the end of this chapter.

Parameter	Sample A	Sample B	Sample C
c_b (GPa^{-1})	6.41E-02	5.86E-02	6.93E-02
$c_s[VRH]$ (GPa^{-1})	3.41E-02	2.76E-02	3.26E-02
ρ_b (g/cc)	2.48	2.52	2.50
ρ_s (g/cc)	2.61	2.67	2.63
ρ_f (g/cc)	0.89	0.89	0.89
c_f (GPa^{-1})	8.98E-01	9.02E-01	8.98E-01
n [Eq. 3.8] (%)	7.81	8.46	7.05
$B_{comp.}$	0.31	0.30	0.38

Table 3.1: Petrophysically-determined parameters. Determination of the bulk compressibility (c_b), solid aggregate phase compressibility (c_s), and porosity are described in the text. The individual solid phase compressibilities used in the computation of c_s are from Mavko et al. (2020): dolomite = 1.25E-02 GPa^{-1}, calcite = 1.41E-02 GPa^{-1}, quartz = 2.70E-02 GPa^{-1}, and kerogen = 3.42E-01 GPa^{-1}; the remaining grain compressibility is from Wang et al. (2001): illite = 1.67E-02 GPa^{-1}. The individual solid phase densities used in the computation of n are: dolomite = 2.84 g/cc, calcite = 2.71 g/cc, quartz = 2.65 g/cc, illite = 2.76 g/cc, and kerogen = 1.20 g/cc.

To determine the compressibility of the solid aggregate phase (c_s), I first determine the rock's mineralogic and organic content. These were analyzed with X-ray diffraction at thirty-three locations along the core, but not at the precise location of my experimental test samples. I therefore estimate the solid aggregate phase composition at my test sample depths using X-ray fluorescence (XRF) measurements of elemental content, which were collected along the entire core at 15 cm sample spacing using Niton 950t Goldd+ hand-held XRF analyzer in mining mode.

I use stoichiometric relationships between elements and the dominant minerals to determine the mineral composition (see Appendix A). The dominant minerals in the organic-rich silty mudstones, which are the lithofacies of the test samples, as determined by the XRD analysis, are quartz, dolomite, illite, and calcite. For prediction of the TOC (kerogen), I develop a simple relationship between TOC and element concentration. Various trace elements, such as bromine, molybdenum, nickel, uranium, and vanadium are

recognized proxies of TOC in source rocks (Mayer et al., 1981; Tribovillard et al., 2006). I determined that vanadium exhibits the strongest correlation to the measured TOC (see Appendix A).

	Estimated from X-Ray Fluorescence					
Sample	**Quartz**	**Calcite**	**Dolomite**	**Illite**	**TOC**	**Total**
[-]	**wt.%**	**wt.%**	**wt.%**	**wt.%**	**wt.%**	**wt.%**
A	41%	1%	8%	28%	5%	84%
B	52%	15%	9%	20%	1%	98%
C	53%	0%	8%	31%	4%	97%
	Estimated from X-Ray Fluorescence (Normalized)					
Sample	**Quartz**	**Calcite**	**Dolomite**	**Illite**	**TOC**	**Total**
[-]	**wt.%**	**wt.%**	**wt.%**	**wt.%**	**wt.%**	**wt.%**
A	50%	2%	9%	33%	6%	100%
B	53%	15%	9%	21%	2%	100%
C	55%	0%	9%	32%	5%	100%

Table 3.2: Solid aggregate phase composition of the test samples. Upper: Solid aggregate phase estimated from XFR. Lower: Solid aggregate phase estimated from XFR that have been normalized such that wt.% = 100.

After determining the XRF-estimated concentration of the minerals and TOC at the sample locations (upper portion of Table 3.2), I normalize these so the sum of the weight fractions is 100% (lower portion of Table 3.2). A pie chart of the normalized solid aggregate phase concentrations is shown in Figure 3.2.

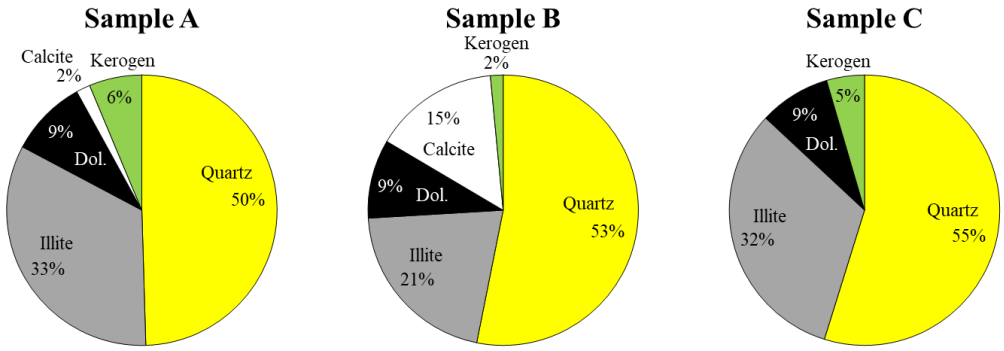

Figure 3.2: Solid aggregate phase composition of the test samples. The values are in weight percent (wt.%).

I combine these normalized concentrations with the respective compressibilities of each component (listed in the caption of Table 3.1) to compute the compressibility of the solid aggregate phase using the Voight-Reuss-Hill averaging technique (Hill, 1952):

$$c_s[VRH] = \frac{c_s[Voigt]+c_s[Reuss]}{2}, \quad (3.4)$$

with the Voigt compressibility ($c_s[Voigt]$) and the Reuss compressibility ($c_s[Reuss]$), respectively, computed as:

$$c_s[Voigt] = \sum_{i=1}^{N} f_i * c_{s,i}, \quad (3.5)$$

and

$$c_s[Reuss] = \left[\sum_{i=1}^{N} \frac{f_i}{c_{s,i}}\right]^{-1}, \quad (3.6)$$

where N represents the number of solid components which comprise the solid aggregate phase (minerals + TOC), and f_i and $c_{s,i}$ represent the normalized weight fraction and the compressibility, respectively, of the *i*th solid component. Sample A has the highest solid aggregate compressibility (c_s [VHR]= 3.41E-02 GPa^{-1}), followed by sample C (c_s = 3.26E-02 GPa^{-1}), then sample B (c_s = 2.76E-02 GPa^{-1}) (Table 3.1).

I next determined the density of the solid aggregate phase (ρ_s). ρ_s is computed by summing the products of the normalized weight fractions, previously computed, and the respective densities of each component:

$$\rho_s = \sum_{i=1}^{N} f_i * \rho_i, \quad (3.7)$$

where ρ_i represents the density of the *i*th solid component. The resulting ρ_s for samples A, B, and C is 2.61 g/cm^3, 2.67 g/cm^3, and 2.63, g/cm^3, respectively (Table 3.1). In order to evaluate these values, experimental measurements of ρ_s were also conducted in accordance with ASTM D550 Specific Gravity of Soil Solids by Gas Pycnometer, yielding 2.60 g/cm^3, 2.65 g/cm^3, and 2.63 g/cm^3 for samples A, B, and C, respectively.

I estimated the in-situ fluid densities and compressibilities for a gas saturated oil (live oil) and brine fluid mixture using the Batzle and Wang (1992) equations. I use an oil API of 40 and a gas density of 0.60 g/cm^3, both of which are obtained from publicly available well test data at my testing location, and assume a pure water velocity of 1500 m/s, a salinity of 100,000 ppm (Dvorkin et al., 2021), and a temperature gradient of 21.8 ^{o}C/km (Sinclair, 2007). The fluid saturations were determined in a commercial lab using the Dean Stark method (Luffel and Guidry, 1992): 33.5% oil (average) and 65.9% brine (average). The resultant fluid density (ρ_f) is 0.89 g/cc for each of the samples, and the fluid compressibility (c_f) is 8.98E-01 GPa^{-1} for sample A, 9.02E-01 GPa^{-1} for sample B, and 8.98E-01 GPa^{-1} for sample C.

I then combine ρ_s and ρ_f with the wireline bulk density (ρ_b) to compute porosity (n) using the mass-balance equation:

$$n = \frac{\rho_s - \rho_b}{\rho_s - \rho_f}. \quad (3.8)$$

The porosities I calculated for samples A, B, and C are 7.81%, 4.92%, and 7.05%, respectively (Table 3.1). Whereas ρ_f is the same for each sample, the difference in porosities is the result of different ρ_s and ρ_b for each sample. In addition, the GRI (crushed

rock) porosity was independently determined by a commercial lab on other sections of the core. The GRI porosity was measured on the same lithology as my test samples and ranges between 5.1 to 12.6%, with an average of 9.6%.

I finally compute Skempton's B at each sample depth using Eq. 3.2. The Skempton's B coefficient I computed for sample A is $B_{comp.}$ = 0.31, sample B is $B_{comp.}$ = 0.30 and sample C is $B_{comp.}$ = 0.38 (Table 3.1).

3.3.3 Experimental Measurements of Skempton's *B* Coefficient: Method & Results

I next experimentally measured Skempton's B coefficient at the same depths where I previously computed it theoretical counterpart. I followed the experimental approach according to ASTM D7181, with slight modifications to accommodate the experimental apparatus I used and the low-permeability nature of my test samples.

The experimental apparatus is schematically depicted in Figure 3.3. The cell is a standard biaxial-type core holder built by Core Lab (Model RCHT-1.0) that is housed in an insulated cabinet. A climate control system maintains a temperature of 28ºC ($\pm$0.5ºC). The sample is set between two 1-inch steel endcaps, one of which is fixed. The endcaps are designed with flow distribution channels on the contact faces abutting the sample and drainage lines connecting to the pore fluid system. The back pressure is controlled by a pair of positive displacement pumps manufactured by Chandler Engineering (Quizix QX-6K) with a working pressure of 41 MPa and a flow rate resolution of 0.001 mL/min. They are positioned above the cell and have an air release valve to allow air to be purged from the fluid lines. The saturating fluid is dodecane ($C_{12}H_{26}$).

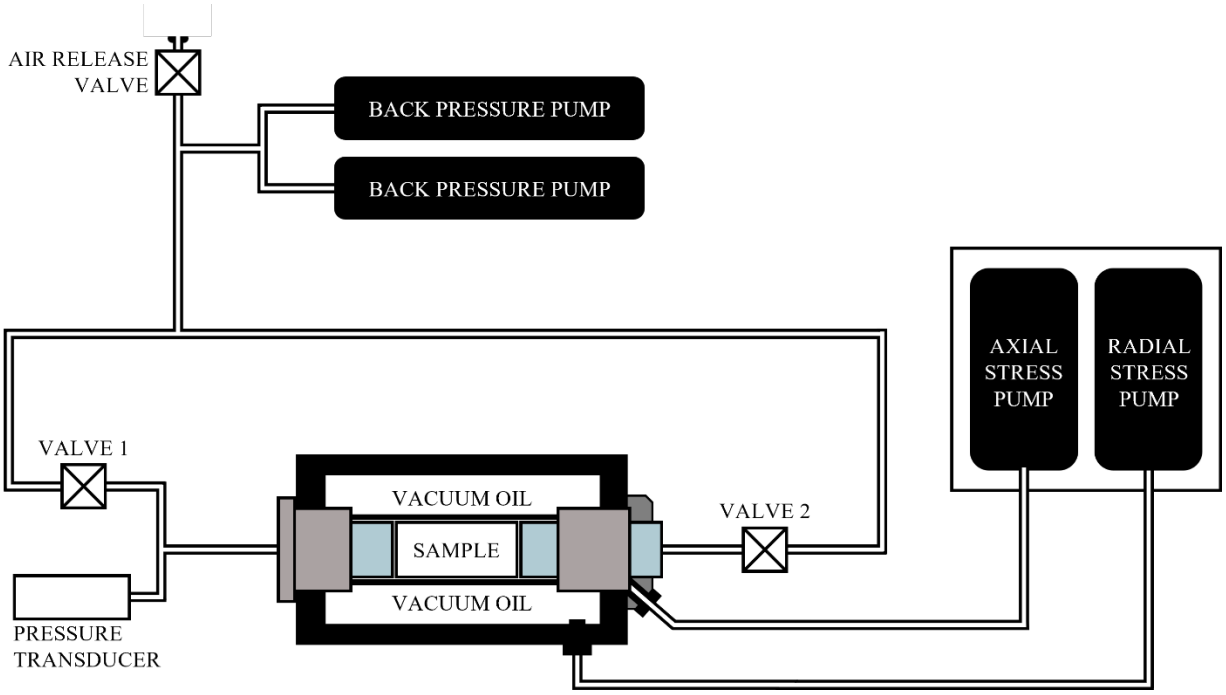

Figure 3.3: Schematic diagram of experimental equipment for *B* measurements. The equipment is housed in a climate-controlled cabinet.

The non-fixed endcap functions as a piston. It transmits application of the axial stress by a positive displacement pump (Quizix Q5K) that has a working pressure of 69 MPa and a flow rate resolution of 0.000031 mL/min. The radial stress is applied around the sample by hydraulic fluid (vacuum oil). The hydraulic fluid occupies the annular space of the cell, and a 5.1 mm (0.2") thick 70 Durometer Viton sleeve isolates the sample and endcaps from the hydraulic fluid. The pump that controls the axial stress also controls the radial stress. Bounding each side of the cell is a fluid line valve. A pressure transducer is connected between one of the fluid line valves and the cell. It has a measuring range of 0-35 MPa with 0.04% full scale accuracy. The fluid line volume between valves 1 and 2 is 2.77 mL.

I extracted 2.54 cm diameter test samples from the core using an air-cooled drill press. I cut the test samples to a length slightly over 2.54 cm, and sanded the ends until the

length at any point measured within a tolerance of ± 0.05 mm. I then recorded the dimensions ("*V*" in Figure 3.4), after which I imaged the samples using high-resolution X-ray computed tomography (CT) (Figure 3.4).

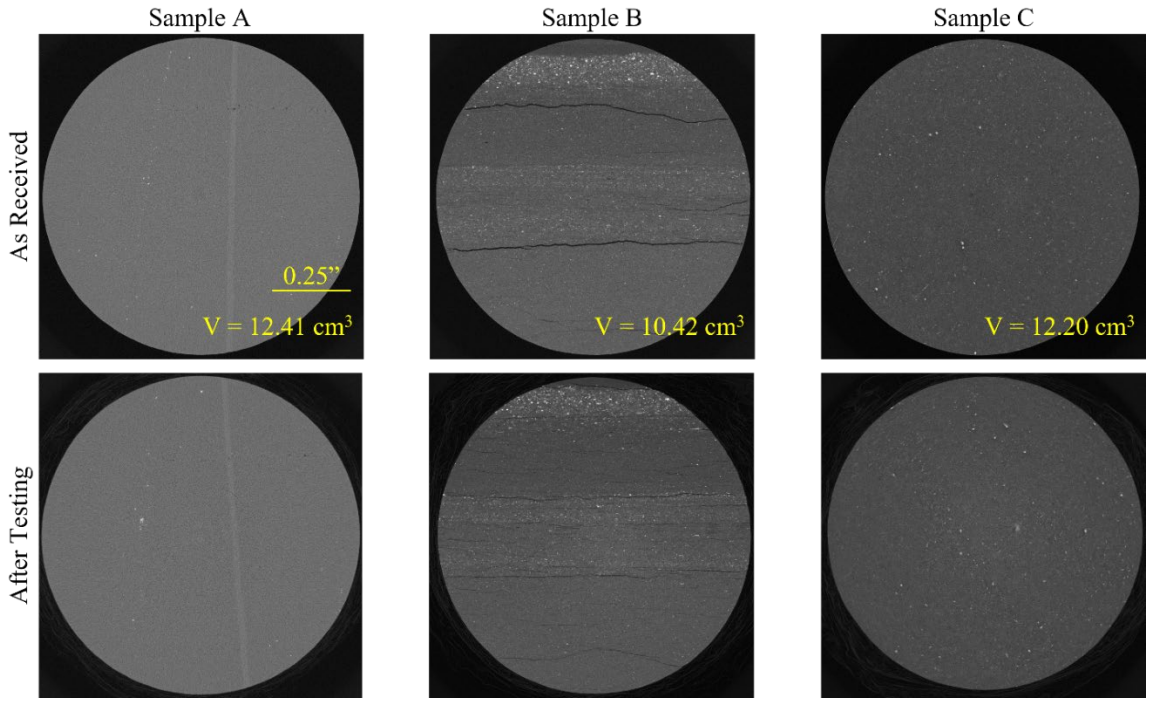

Figure 3.4: CT images of samples. The images measured before (top row) and after (bottom row) the experimental testing for samples A, B, and C (left, middle, and right columns, respectively). The pre-testing volume (V) of each sample is also recorded.

I then applied a vacuum to each sample for 5 minutes, after which I flooded the sample with saturant (dodecane) while still in the vacuum chamber. This causes the saturant to be driven into the sample's pore spaces. After the sample had sat immersed in dodecane for 24 hours, I placed it into the experimental cell.

Next, I subjected the sample to a pore pressure of 5.2 MPa and a confining stress of 6.9 MPa for 5 days to force any remaining gas into solution. Upon completion, I performed a series of "Skempton's *B* checks" to verify sample saturation (Makhnenko and

Labuz, 2013). I began each Skempton's B check by closing the fluid drainage valves that bound the experimental cell (Figure 3.3). This isolates the sample from the pore pressure pumps. I gave a period of serval minutes to allow the sample's pore pressure to equilibrate with the system, after which I increased the confining stress by 1.4 MPa. I measured the resulting change in the sample's pore pressure over a period of 20 minutes, then I decreased the confining stress back to the value at the start of the Skempton's B check. I next opened the fluid line drainage values and uniformly increased the pore pressure and confining stress by 0.7-1.0 MPa. I allowed the system to equilibrate for 24 hours, after which I performed the next Skempton's B check by following the same procedure previously described. I performed these measurements at least three times at successively higher confining stresses and pore pressures, with 24 hours given between each test to facilitate interpretation of the results.

Following each Skempton's B check, I determined the resulting Skempton's B coefficient using Eq. 3.1. According to Wissa (1969), Skempton's B for a saturated rock should be constant and independent of the pore pressure for soils of low compressibility. Thus, I considered the sample to be fully saturated if Skempton's B did not change with each successive increase in pressure and stress. If, however, Skempton's B did change (e.g., because gas is still being forced into solution), I continued this process of successively increasing the pore pressure and confining stress until a consistent Skempton's B coefficient could be achieved. I interpreted each sample to be fully saturated at a pore pressure of 6.9 MPa.

I next "seasoned" the sample by subjecting it to two stress cycles of loading and unloading (Bernabe, 1986; Warplnski and Teufel, 1992). I did this by increasing the confining stress to 62 MPa, which is the approximate capacity of the measuring system,

while maintaining a fixed pore pressure. This state was held for 24 hours before I reduced the confining stress, waited another 24 hours, and repeated the stress cycle.

After an additional 24 hours, I measured the Skempton's B coefficient at each samples' in-situ effective stress. I determined the in-situ effective stress in the following way. I first computed the total vertical stress (σ_v) by integrating the weight of the overlying material:

$$\sigma_v = \int_0^Z \rho_b(Z) g dZ, \tag{3.9}$$

where Z is depth, $\rho_b(Z)$ is the wireline bulk density determined at depth Z, and g is gravity.

I then estimated the in-situ pore pressure using the DFIT measurements. From these measurements, I established a local pore pressure gradient $\left(\frac{\Delta u}{\Delta Z}\right)$, then I recorded the pressure at the sample depths.

I computed the in-situ vertical effective stress (σ_v') at each sample depth as the difference between the total vertical stress and the estimated pore pressure (u):

$$\sigma'_v = \sigma_v - u. \tag{3.10}$$

I then interpreted the least principal stresses from the DFIT, and using these values I established a total horizontal stress gradient ($\frac{\Delta \sigma_h}{\Delta Z}$) (assuming radially symmetric horizontal stresses), after which I calculated the horizontal effective at each sample depth as the difference between the estimated total horizontal stress and the estimated pore pressure):

$$\sigma'_h = \sigma_h - u. \tag{3.11}$$

I finally computed the in-situ mean effective stress (σ_m') using:

$$\sigma'_m = \frac{\sigma_v' + 2\sigma_h'}{3}. \tag{3.12}$$

The mean effective stress I computed for each sample is tabulate in Table 3.3.

Parameter	Sample A	Sample B	Sample C
σ'_m (MPa)	10.3	10.7	10.3
$c_f[dodecane]$ (KPa^{-1})	8.35E-01	8.35E-01	8.35E-01
n (%)	11.11	5.02	4.87
$B_{meas.}$	0.11	0.10	0.13
$B_{corr.}$	0.31	0.30	0.42

Table 3.3: Experimental parameters. Skempton's B measurements "$B_{meas.}$" and corrected Skempton's B measurements "$B_{corr.}$".

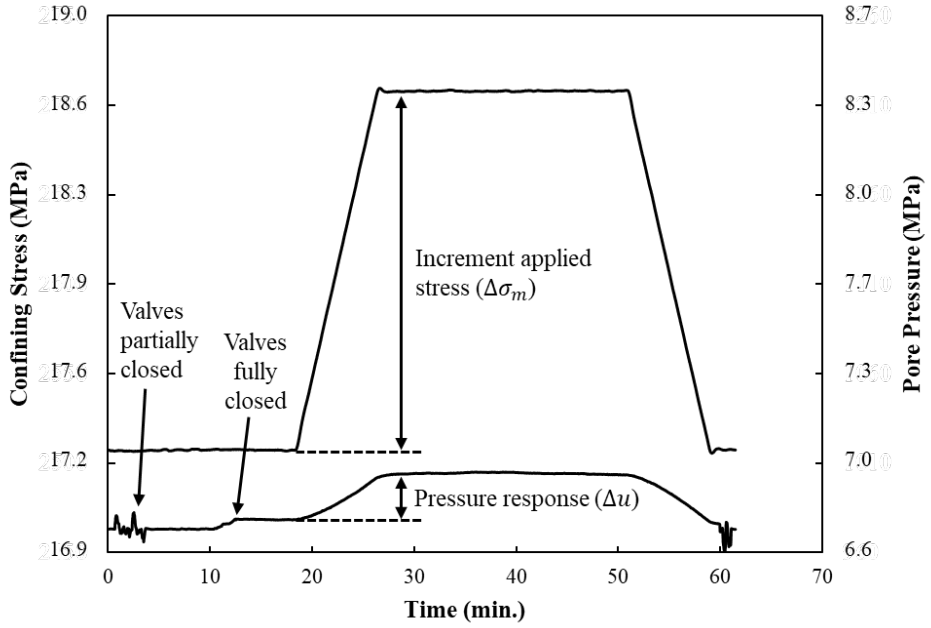

Figure 3.5: A typical Skempton's B test. The upper black line is the confining stress, and the lower black line is the pore pressure.

I repeated each Skempton's B test three times by following the same procedure as described above in the "Skempton's B check;" however, after each Skempton's B test, I did not increase the confining stress and pore pressure (thus, the B tests were each made at a pore pressure of 6.9 MPa). A typical Skempton's B test is shown in Figure 3.5. The average measured Skempton's B coefficient for sample A is $B_{meas.}$ = 0.11; sample B is $B_{meas.}$ = 0.10; and sample C is $B_{meas.}$ = 0.13 (Table 3.3).

Lastly, I removed the existing pore pressure and confining stress over a 24-hour period, extracted the sample from the experimental cell, and recorded its mass. Immediately following this, I wrapped the sample in plastic wrap, assessed the porosity using nuclear magnetic testing (NRM) (Table 3.3), and imaged the sample a final time using high-resolution X-ray computed tomography (CT) (Figure 3.4).

3.3.4 Correcting Experimental Measurements for System Compressibility

Once the Skempton's B coefficient had been experimentally measured, I made a correction to account for the compressibility of the measuring system. This is a critical step, since in practice it is impossible to maintain truly undrained conditions with any experimental setup. Bishop (1976) recognized that when Skempton's B is measured experimentally, the changes in pore pressure will not only be influenced by the applied load, but also by the compressibility of the pore pressure measuring system. He derived an equation to correct $B_{meas.}$ for the system compressibility:

$$B_{corr.} = \frac{1}{\frac{1}{B_{meas}} - \frac{V_L}{V} * \frac{c_f}{c_b - c_s} - \frac{c_L + c_M}{V(c_b - c_s)}}, \qquad (3.13)$$

where $B_{corr.}$ is the measured B coefficient ($B_{meas.}$) corrected for system compressibility, V_L is the volume of the drainage lines, V is the sample volume, c_L is the compressibility of the drainage lines and valves, and c_M is the compressibility of the pore pressure transducer.

I measured the compressibility of the system (Appendix B) and the drainage line volume. The results yield $c_L + c_M$ = 1.42E-02 KPa^{-1} and V_L = 2.77 mL. I derived the fluid compressibility (c_f) of the saturant (dodecane) at conditions representative of the experimental parameters (experiments were conducted at a pore pressure of 6.9 MPa and a temperature of 28.5°C; at these conditions, the compressibility of dodecane is 8.35E-01 GPa^{-1}; from dos Santos Junior et al. (2022)). I then combined each of these parameters with the c_b and c_s values I determined petrophysically for each sample (Table 3.1) and V (Figure

3.4), and computed $B_{corr.}$ with Eq. 3.13 (Table 3.3). For Sample A, $B_{corr.}$ is 0.31; for Sample B, $B_{corr.}$ is 0.30; and for Sample C, $B_{corr.}$ is 0.42 (Table 3.3)

3.4 DISCUSSION

A comparison of the experimental measurements of Skempton's B ($B_{meas.}$ vs. $B_{corr.}$ in Figure 3.6) underscores the influence the equation to correct for system compressibility (Eq. 3.13) can have on the corrected B coefficient ($B_{corr.}$).

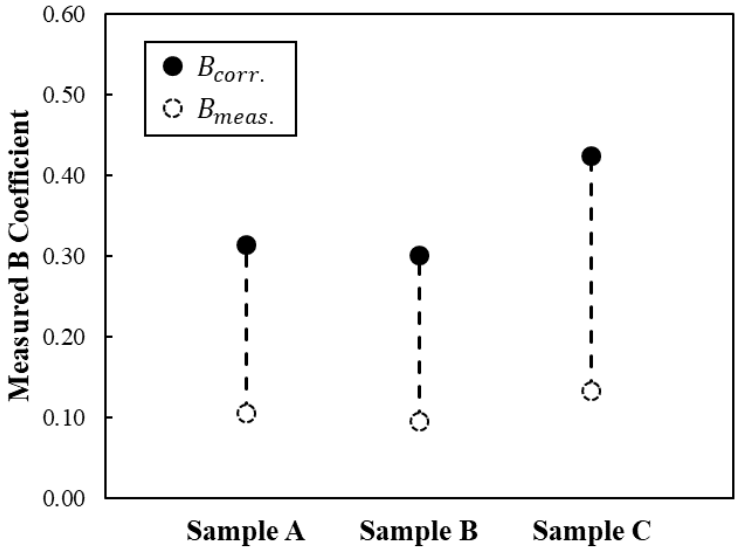

Figure 3.6: Experimental B measurements. The white dashed-dot represents the measured B coefficient ($B_{meas.}$), and the black dot represents $B_{meas.}$ corrected for system compliance ($B_{corr.}$).

After applying this correction, $B_{meas.}$ for samples A and B is increased by 0.21. The largest increase is observed in sample C, with $B_{meas.}$ increasing by 0.29. This is primarily driven by the difference in the bulk (c_b) and solid compressibilities (c_s) determined for each sample.

The ratio of c_b to c_s introduces a complication into the equation to correct $B_{meas.}$ for system compressibility (Eq. 3.13). Small changes in this ratio can have a prodigious impact on $B_{corr.}$ To illustrate this, I calculated $B_{corr.}$ as a function of c_b to c_s for sample A (blue line in Figure 3.7), sample B (orange line in Figure 3.7), and sample C (red line in Figure 3.7). It can be seen in the case of all three samples that changes in this ratio results in exponential changes in $B_{corr.}$. As the ratio increases, $B_{corr.}$ asymptotically approaches $B_{meas.}$ Conversely, as the ratio decreases, $B_{corr.}$ approaches infinity.

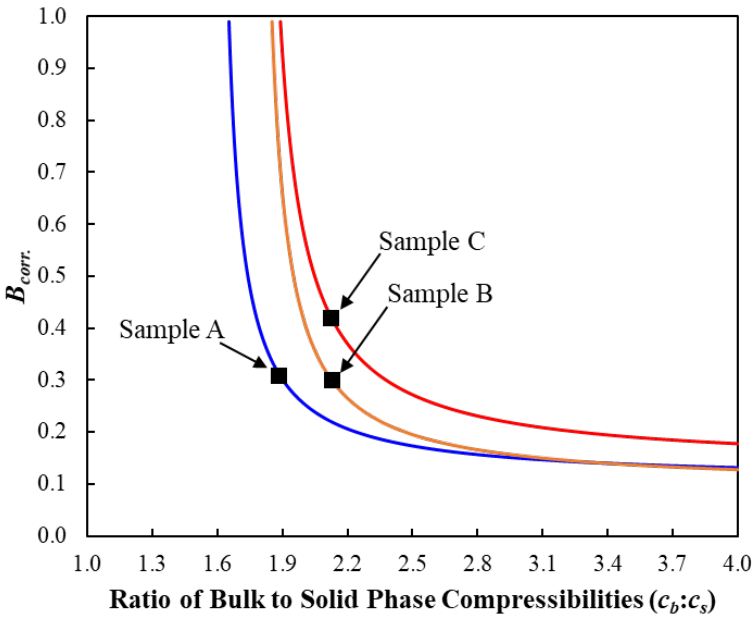

Figure 3.7: $B_{corr.}$ vs. c_b: c_s. The blue line is sample A, the orange line is sample B, and the red line is sample C. The black square represents $B_{corr.}$ determined with c_b and c_s I computed for each sample.

The question arises as to the accuracy of the c_b and c_s values I computed for the test samples. As documented earlier, I computed the dynamic c_b using Eq. 3.3. There is much experimental evidence showing that dynamic elastic parameters obtained from acoustic velocities and density can greatly differ from those determined from static

experimental measurements of stress and strain. These differences are largely attributed to the mechanical properties of the materials involved (Fjær et al., 2013). While the exact reasons for these discrepancies are not fully understood, evidence suggests they tend to diminish under certain conditions applicable to the rocks studied in this paper.

For one, in a standard rock mechanical test, the material behavior is measured during initial loading. My test samples, both in-situ and during the experimental tests, are not at their past maximum stress state and thus lie inside their yield surface. Plona and Cook (1995) showed that, during unloading-reloading cycles, the elastic and dynamic parameters begin to converge as the strain amplitude is reduced.

A second is that the difference in static and dynamic parameters is more pronounced in weak, unconsolidated materials and in test samples with core disturbances (micro-cracks), which can reduce the velocity. My rocks, in contrast, are geologically old and buried deep in the subsurface and thus exhibit high stiffness. Furthermore, through the process of stress cycling ("seasoning"), I mitigated the core disturbances in my test samples. King (1969) demonstrated that the difference in static and dynamic parameters is reduced with increasing confining stress; this increases the rock stiffness and further minimizes core disturbances.

I compared the c_b values I derived from the wireline velocities and bulk densities with static and dynamic measurements of c_b made on different sections of the core (blue and orange dots, respectively, in Figure 3.8); these measurements were independently determined in a commercial lab. I also compared my values determined from the elastic properties presented in Zheng and Sharma (2021) on Wolfcamp mudrock (yellow dots in Figure 3.8). The c_b values I determined fall within the range of both the static measurements and Zheng and Sharma (2021). Interestingly, my c_b values exhibit a higher

compressibility than the dynamic values that were independently determined in a commercial lab.

For c_s, the model I developed to estimate the solid aggregate phase components of my test samples, which I then used to calculate c_s, shows excellent agreement with the actual XRD and TOC measurements (Figure C.1 and Figure C.2 in Appendix C). However, as I previously demonstrated, even slight changes in c_b relative to c_s can significantly impact $B_{corr.}$.

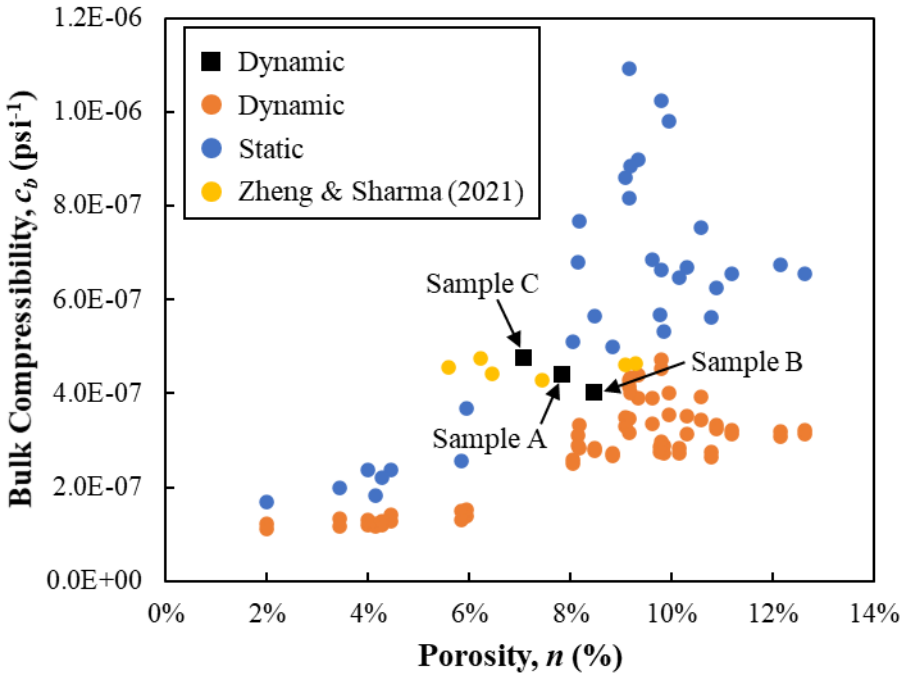

Figure 3.8: Comparison of bulk compressibilities. Black squares represent dynamic c_b computed from wireline velocities and densities for samples A, B, and C; blue and orange dots represent bulk compressibility computed from dynamic and static measurements, respectively, made on other sections of the core by an independent commercial lab; and yellow dots represent bulk compressibilty from literature determined in Wolfcamp (Zheng and Sharma, 2021).

Finally, I compared my experimental Skempton's B measurements corrected for system compressibilty ($B_{corr.}$) with my computed Skempton's B coefficients ($B_{comp.}$) determined at the test sample depths. $B_{corr.}$ with dodecane as the pore fluid (black circles in Figure 3.9) generally match $B_{comp.}$ with the in-situ fluid properties (gray squares in Figure 3.9). However, in order to make a precise comparison, the fluid compressibility used in the computation of $B_{comp.}$ needs to be replaced with the fluid compressibility in $B_{corr.}$; the remaining parameters, c_b, c_s, and n (Table 3.1), remain unchanged. In $B_{corr.}$, the fluid compressibility of dodecane (the pore fluid in the test samples) at the experimental conditions (pore pressure of 1,000 psi and temperature of 28.5ºC) is c_f = 8.35E-01 KPa^{-1}. By using this value in lieu of the in-situ fluid compressibilities, $B_{comp.}$ is increased by 0.01 for each sample.

With the fluid compressibilities matching, my experimental and computational determinations of Skempton's B show a strong agreement for samples A and B (black circles vs. black squares in Figure 3.9). However, sample C shows a greater discrepancy.

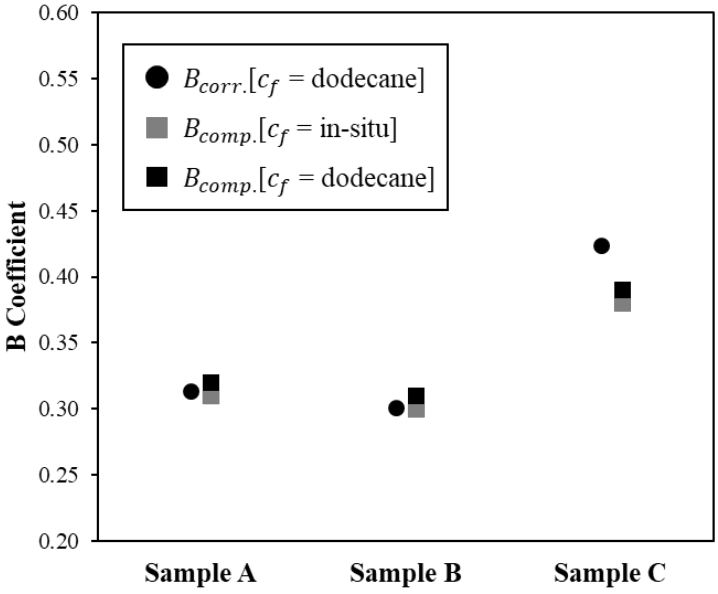

Figure 3.9: Comparison of $B_{meas.}$ and $B_{corr.}$ with different pore fluids. The black shapes represent the computations made with dodecane at the experimental conditions. The gray squares represent the computations made with the in-situ fluids.

There are multiple potential reasons for this difference, including the accuracy of the determined solid and fluid compressibilities, as previously discussed, the assumptions underlying the derivations of $B_{comp.}$ (Eq. 3.2) and $B_{corr.}$ (Eq. 3.13), which are beyond the scope of this paper, and the compressibility of the measuring system.

In terms of system compressibility, the compressibility of the stainless-steel tubing, valves, and the pressure transducer ($c_L + c_M$ in Eq. 3.2) contributes to ~1% of the system compressibility; the dead volume (V_L in Eq. 3.2) contributes to the remaining ~99%. The dead volume is the volume of the pore pressure lines between the fluid line valves and the experimental cell. The degree to which dead volume impacts the changes in measured pressure during a B test is a function of the ratio of dead volume to sample volume ($V_L : V$).

Although Eq. 3.13 should theoretically correct for dead volume, I examined the influence of this on $B_{corr.}$. I calculated $B_{corr.}$ as a function of $B_{meas.}$ for sample C's

measured volume (V = 12.20 cm^3) (red line in Figure 3.10), and for the maximum volume the system can accommodate (V = 25.74 cm^3) (blue line in Figure 3.10); the arrows represent the corrected B value for three measurements that were made on sample C ($B_{meas.}$ = 0.125, 0.122, and 0.150) for both values of V. Using the measured V of sample C, $B_{corr.}$ ranges from 0.33 to 0.68. For the maximum V the system can accommodate, $B_{corr.}$ ranges from 0.17 to 0.24. Thus, the range is much smaller with the higher V relative to the dead volume.

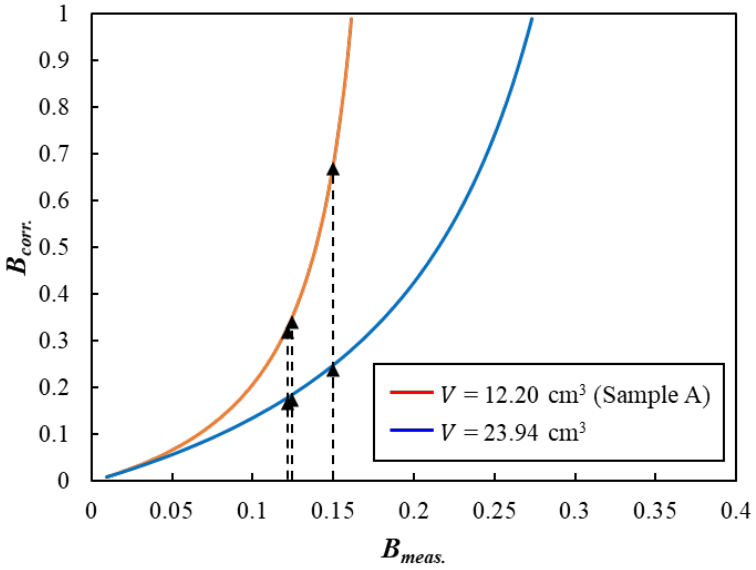

Figure 3.10: $B_{corr.}$ as a function of $B_{meas.}$. Red line represents relationship with sample C's measured volume (V = 12.20 cm^3); blue line represents the maximum sample volume the experimental equipment can accommodate (V = 25.74 cm^3). The arrows show $B_{corr.}$ for the three $B_{meas.}$ made on sample C.

Other literature has examined this problem. Green and Wang (1986) used an experimental apparatus with the pore pressure transducer built into one endcap, thereby eliminating the dead volume. However, the limitations of the equipment I used in my experiments make it impossible to reduce the dead volume any further. Makhnenko and Podladchikov (2018) used an experimental apparatus with a dead volume of 9.5 mL. This

is approximately 3.5 times the dead volume of my experimental equipment; however, the volume of their test samples was greatly larger than mine, with their V = 206 cm^3, thus the ratio of their dead volume to sample volume was relatively small (V_L: V = 0.05). Even if I were to use the maximum volume that the experimental system I used can accommodate, the ratio of dead volume to sample volume would still be 2x that of Makhnenko and Podladchikov (2018). Unfortunately, due to the brittle nature of the core from which I extracted the test samples, I was not able to obtain any larger samples. Therefore, with the dead volume of my experimental system, there is a degree of uncertainty in my measured Skempton's B coefficients corrected for system compressibilty.

Despite this difference in sample C, I have demonstrated that comparable Skempton's B coefficients can be determined with two different techniques. Whereas the experimental approach is challenging, time-consuming, requires expensive testing equipment and samples on which to perform the tests, the effective medium computational approach offers a cost-effective and efficient alternative to determine Skempton's B with similar precision.

3.5 Summary and Conclusions

In this work, I presented two distinct approaches to determine Skempton's pore pressure buildup coefficient B on Wolfacamp mudrock: effective medium petrophysical computation and experimental measurements. Using data from a well in the Delaware Basin, the effective medium petrophysical computations with dodecane as the pore fluid yielded $B_{comp.}$ = 0.32, 0.31, and 0.39. The experimental measurements, which were corrected for system compressibility, resulted in $B_{corr.}$ = 0.31, 0.30, and 0.42, at the same respective depths as $B_{comp.}$. These results show that comparable Skempton's B coefficients can be obtained using these two different techniques. However, my work underscores that

the effective medium computational approach offers an efficient alternative for determining Skempton's B that avoids the complexities and challenges associated with experimental testing, of which the most challenging (and can be the most consequential) is the difficulty of achieving truly undrained conditions.

Symbol	Name	Unit
B	Skempton's pore pressure buildup coefficient	$-$
$B_{corr.}$	$B_{meas.}$ corrected to account for compressibility of measuring system	$-$
$B_{comp.}$	Computed B coefficient	$-$
C	Uniaxial strain pore pressure buildup coefficient	$-$
c_b	Bulk compressibility	KPa^{-1}
c_f	Fluid compressibility	KPa^{-1}
c_s	Solid grain compressibility	KPa^{-1}
C_L	Drainage lines and valves compressibilities	mL^3/KPa
C_M	Pore pressure transducer compressibility	mL^3/KPa
g	Acceleration of gravity	m/s^2
n	Porosity	$-$
ρ_f	Fluid density	g/cm
ρ_b	Bulk density	g/cm
σ	Isotropic total stress	MPa
σ_h	Horizontal total stress	MPa
σ_v	Vertical total stress	MPa
σ'_h	Horizontal effective stress	MPa
σ'_m	Mean effective stress	MPa
σ'_v	Vertical effective stress	MPa
u	Pore pressure	MPa
V	Sample bulk volume	mL
V_L	Fluid line, drainage valves, and pore pressure transducer volume	mL
V_p	Compressional wave velocity	m/s
V_s	Shear wave velocity	m/s
Z	Depth	m
Δ	Change = final - initial	$-$

Table 3.4: Nomenclature. This table provides a list of the symbols, names, and units.

Parameter	Sample A	Sample B	Sample C
c_b (GPa^{-1})	6.41E-02	5.86E-02	6.93E-02
$c_s[VRH]$ (GPa^{-1})	3.41E-02	2.76E-02	3.26E-02
ρ_b (g/cc)	2.48	2.59	2.50
ρ_s (g/cc)	2.61	2.67	2.63
ρ_f (g/cc)	0.89	0.89	0.89
c_f[in-situ] (GPa^{-1})	8.98E-01	9.02E-01	8.98E-01
c_f[dodecane] (GPa^{-1})	8.35E-01	8.35E-01	8.35E-01
n[Eq. 3.8] (%)	7.81	8.46	7.05
n[NMR] (%)	11.11	5.02	4.87
σ'_m (MPa)	10.3	10.7	10.3
$B_{comp.}$[in-situ]	0.31	0.30	0.38
$B_{comp.}$[dodecane*]	0.32	0.31	0.39
$B_{meas.}$	0.11	0.10	0.13
$B_{corr.}$	0.31	0.30	0.42

Table 3.5: Combined experimental and petrophysical parameters. * Derived at experimental conditions (pore pressure = 6.9 MPa & temperature = 30 deg. C) from dos Santos Junior et al. (2022). Other parameters used in $B_{corr.}$ include V_L = 1.42E-02 GPa^{-1} and V = 2.77 mL.

Chapter 4: A Petrophysical Approach for Predicting Pore Pressure in the Unloaded Delaware Basin

4.1 ABSTRACT

I refine the velocity-based model I developed and fully constrained to field data in Chapter 2 with an effective medium approach for computing the uniaxial strain pore pressure buildup coefficient C and the thermal pressure coefficient α in each prediction well using petrophysical data. C defines the undrained changes in pore pressure due to mechanical changes in stress (e.g., erosion); α defines the undrained changes in pore pressure. This approach accounts for the undrained changes in pore pressure resulting from mechanical unloading (due to erosion) and temperature changes (due to uplift). I apply this approach to predict pore pressure in the calibration well and four prediction wells. The differences in predicted pore pressures compared with the measured pressures is 352 psi in the calibration well, 771 psi in well "a," 499 psi in well "g," and 367 psi in well "e."

4.2 INTRODUCTION

In this last chapter, I integrate and build upon the equations and concepts I developed in Chapters 2 and 3 to present a final approach for predicting pore pressure in unloaded basins. I use the velocity-effective stress formulation I developed in Chapter 2:

$$V = V_w + A\left[\sigma_p'\left(\frac{\sigma_v'}{\sigma_p'}\right)^{\frac{1}{U}}\right]^B, \qquad (4.14)$$

and, as I will show, I refine the computation of σ_p' in the undrained section.

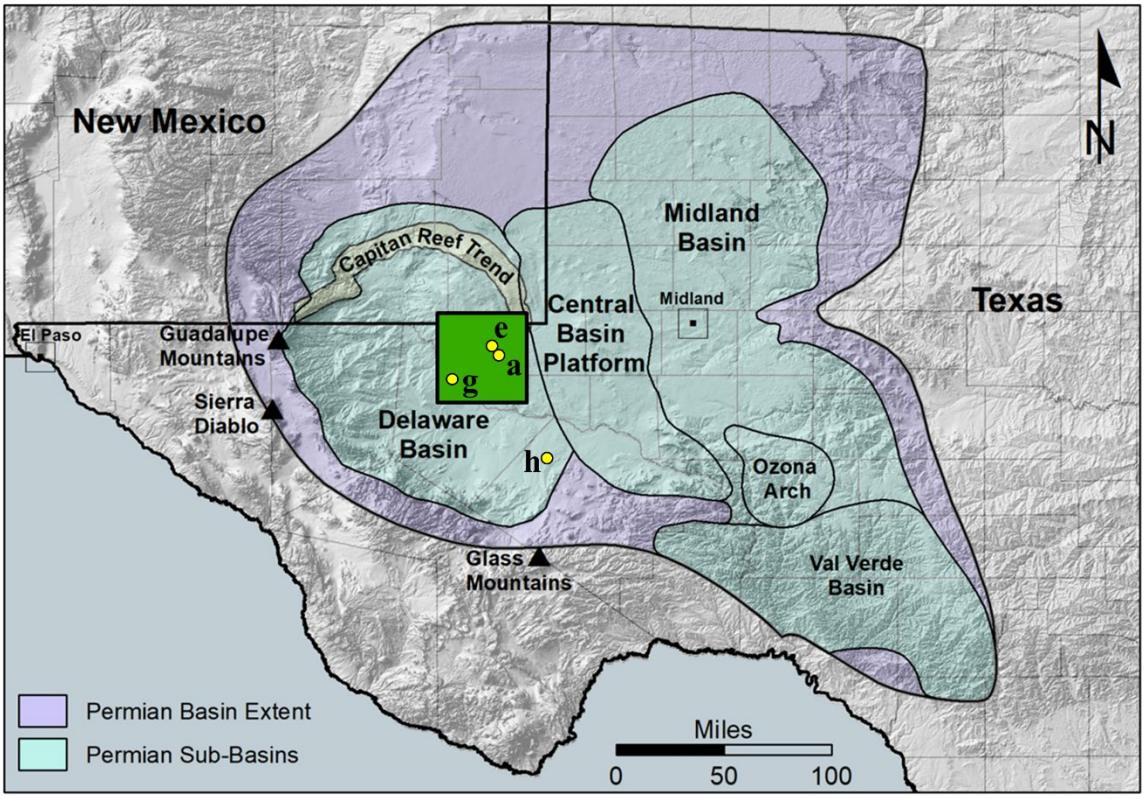

Figure 4.1: Map of calibration well and prediction wells. Calibration well is located within the green box.

A key assumption underlying my approach in Chapter 2 is that A, B, U, C, V_w, and $\frac{\Delta\sigma_v}{\Delta Z}$ in Eq. 4.14 are constant across the basin. I documented my process to calibrate these parameters to field data, and I presented the values I determined in the calibration well (located within the green box in Figure 4.1), which are tabulated in Table 4.1.

Parameter	Value
$A\left(\frac{ft}{psi^B * s}\right)$	14
B	0.73
$U\left(\frac{ft}{psi^B * s}\right)$	10
C	0.80
$V_w\left(\frac{ft}{s}\right)$	5,000
$\frac{\Delta\sigma_v}{\Delta Z}\left(\frac{psi}{ft}\right)$	1.04

Table 4.1: Model parameters. A, B, U, and $\Delta\sigma_v/\Delta Z$ are constrained in the calibration well.

I then presented a process to determine ΔH in the prediction wells, after which I determined σ_v' and subsequently computed u. My results showed that the predicted pore pressures in each prediction well aligned more closely with the measured pressures than the traditional approaches, which fundamentally assume the rock's compaction state is described by the normal compaction trend (and thus assumes a single relationship between velocity and effective stress), regardless of its burial history (Chapter 2, Figure 2.7). However, my approach did not offer a solution to determine the uniaxial strain pore pressure buildup C coefficient independently in each well; instead, I had constrained it to measured pressures in the calibration well and assumed it was constant across the basin.

Thus, in chapter 3, I introduced an effective medium approach to determine Skempton's B coefficient using petrophysical data. As I will demonstrate in this chapter, the computation of Skempton's B allows for the uniaxial strain pore pressure buildup coefficient C to be individually determined in each prediction well. Still, as I will also show, this approach of determining Skempton's B and mapping it to C results in values that are too small to describe the observed behavior in the prediction wells. Thus, another physical process needs to be included: one that accounts for the temperatures changes that

occur during erosion when a basin is uplifted from a deeper, warmer depth to a shallower, cooler depth. This is defined by the thermal pressure coefficient α.

I begin this final chapter of my dissertation by describing α. I derive an expression to integrate this coefficient into my undrained pore pressure prediction model (Eq. 4.14), and provide an effective medium approach to determine this parameter using petrophysical data. I then compute α and C in the calibration well and in each prediction well, after which I predict pore pressure. I compare these results against the pressures predicted in Chapter 2 (which, again, assumes all of the parameters listed in Table 4.1 are constant across the basin). Additionally, I perform a sensitivity analysis on the A and B parameters.

4.3 Study Area, Prediction Wells, and Data

The study area and prediction wells in this chapter are shown in Figure 4.1. In each well, I utilize the wireline gamma ray, P- and S-wave velocities, and bulk densities. I also incorporate the X-ray diffraction (XRD) and total organic content (TOC) measurements determined on the core from each well. In the wells where there is an absence of XRD and TOC data, I use the X-ray fluorescence data that was collected on the core. Where available, I also use the oil API and gas densities acquired during the well tests, and the water and hydrocarbon saturation numbers that were independently determined by a commercial lab using the Dean Stark method (Luffel and Guidry, 1992).

4.5 Thermal Pressure Coefficient α

Pore pressure buildup coefficients describe the undrained changes in pore pressure due to mechanical changes in stress. For the case of a uniaxial strain enviornment, this is represented by the uniaxial strain pore pressure buildup coefficient C and the change in total vertical stress ($\Delta\sigma_v$):

$$\Delta u_{mech.} = C\Delta\sigma_v, \quad (4.15)$$

where $\Delta u_{mech.}$ is the undrained change in pore pressure due to a change in mechanical stress (e.g., erosion), which I introduced in Chapter 2 (section 2.2.1).

What pore pressure buildup coefficients do not capture is the additional changes in pore pressure caused by temperature changes when a rock is structurally uplifted from a deeper, warmer depth to a shallower, cooler depth. In a completely sealed system, fluid pressure will change with temperature. The thermodynamic relationship between pressure ($u_{therm.}$) and temperature (T) for an undrained rock is defined by the thermal pressure coefficient α (Wang et al., 1997):

$$\Delta u_{therm.} = \alpha\Delta T. \quad (4.16)$$

Palciauskas and Domenico (1989) show that α is a function of the porosity (n), the compressibilities (c_s is solid and c_f is fluid), and the thermal coefficients of expansion such that:

$$\alpha = \frac{n(\alpha_f+\alpha_s)}{c_s+nc_f}. \quad (4.17)$$

where α_f is the fluid expansion coefficient and α_s is the solid expansion coefficient.

Eqns. 4.15 and 4.16 can be combined to capture the undrained changes in pore pressure in a rock with a burial history of erosion (mechanical effects) and structural uplift (thermal effects):

$$\Delta u = \Delta u_{mech.} + \Delta u_{therm.}, \quad (4.18)$$

which can be rewritten as:

$$\Delta u = C\Delta\sigma_v + \alpha\Delta T. \quad (4.19)$$

The total undrained change in pore pressure is illustrated in Figure 4.2, which shows the undrained pore pressure changes if only the mechanical effects are considered (defined by C and represented by the orange dot in Figure 4.2), the changes if only the thermal

effects are considered (represented by the yellow dot in Figure 4.2), and the changes if both the mechanical and thermal effects are combined (represented by the brown dot in Figure 4.2).

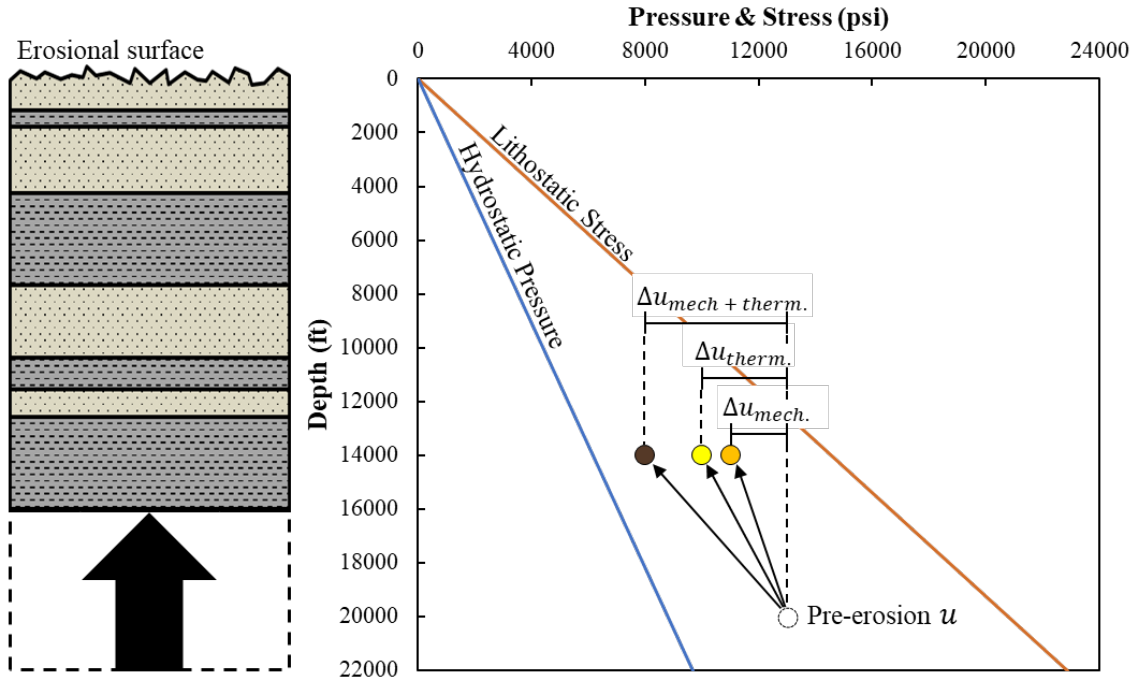

Figure 4.2: Schematic of undrained changes in pressure due to mechanical and thermal effects. The orange dot represents the change if only the mechanical effects are considered, as determined by the pore pressure buildup coefficient C; the yellow dot represents the change if only the thermal effects are considered, as defined by the thermal pressure coefficient; the brown dot represents a sum of the mechanical and thermal effects.

The relative ratio of the undrained changes in pore pressure due to the mechanical and thermal effects is Λ:

$$\Lambda = \frac{\Delta u_{mech.}}{\Delta u_{therm.}} = \frac{C}{\alpha}\left(\frac{\Delta\sigma_v/\Delta Z}{\Delta T/\Delta Z}\right). \tag{4.20}$$

In Figure 4.2, C is 0.32, α is 41.67, and the temperature gradient is 0.012 °F/ft. With 6,000 ft of erosion, $\Delta u_{mech.}$ is 2,000 psi (orange dot in Figure 4.2), $\Delta u_{therm.}$ is 3,000 psi (yellow dot in Figure 4.2), and the total change in undrained pressure is 5,000 psi (brown

dot in Figure 4.2). The resultant relative ratio of mechanical to thermal effects (Λ; Eq. 4.20) is 0.67. If $\Lambda = 1$, that means the undrained changes in pore pressure due to mechanical and thermal effects is equal. If, on the other hand, $\Lambda = 2$, that means the mechanical effects is twice that of the thermal.

To integrate Eq. 4.19 into the undrained pore pressure prediction model (Eq. 4.14), it must be recast in terms of the preconsolidation stress for undrained mudrock ($\sigma'_{p,UD}$). $\sigma'_{p,UD}$ in the context of a basin with erosional unloading is defined as the present day vertical effective stress (σ'_v) plus the change in vertical effective stress due to erosional unloading ($\Delta\sigma'_v$):

$$\sigma'_{p,UD} = \sigma'_v + \Delta\sigma'_v. \tag{4.21}$$

Using Terzaghi's effective stress concept (Terzaghi, 1923), $\Delta\sigma'_v$ can be expressed as:

$$\Delta\sigma'_v = \Delta\sigma_v - \Delta u. \tag{4.22}$$

Substituting this expression for $\Delta\sigma'_v$ into Eq. 4.21 provides:

$$\sigma'_{p,UD} = \sigma'_v + \Delta\sigma_v - \Delta u. \tag{4.23}$$

Next, by substituting Δu in Eq. 4.23 with the expression for Δu in Eq. 4.19, $\sigma'_{p,UD}$ becomes:

$$\sigma'_{p,UD} = \sigma'_v + \Delta\sigma_v(1 - C) - \alpha\Delta T. \tag{4.24}$$

By recasting the reduction in overburden ($\Delta\sigma_v$) due to erosion in terms of the thickness of rock eroded (ΔH) and the overburden gradient ($\Delta\sigma_v/\Delta Z$), $\Delta\sigma_v$ becomes:

$$\Delta\sigma_v = \Delta H \frac{\Delta\sigma_v}{\Delta Z}, \tag{4.25}$$

and, in a similar way, the change in temperature (ΔT) becomes:

$$\Delta T = \Delta H \frac{\Delta T}{\Delta Z}. \tag{4.26}$$

This allows for $\sigma'_{p,UD}$ to be written in terms of both the mechanical and thermal effects by substituting $\Delta\sigma_v$ in Eq. 4.24 with the expression for $\Delta\sigma_v$ in 4.25, and substituting ΔT in Eq. 4.24 with the expression for ΔT in Eq. 4.26:

$$\sigma'_{p,UD} = \sigma'_v + \Delta H \frac{\Delta\sigma_v}{\Delta Z}(1 - C) - \alpha\Delta H \frac{\Delta T}{\Delta Z}. \qquad (4.27)$$

Finally, by combining Eqns. 4.14 and 4.27, the equation to predict vertical effective stress from velocity (sonic P-wave) for undrained rock is:

$$V = V_w + A\left[\left(\sigma'_v + \Delta H \frac{\Delta\sigma_v}{\Delta Z}(1 - C) - \alpha\Delta H \frac{\Delta T}{\Delta Z}\right)\left(\frac{\sigma'_v}{\sigma'_v + \Delta H \frac{\Delta\sigma_v}{\Delta Z}(1-C) - \alpha\Delta T}\right)^{\frac{1}{U}}\right]^B. \quad (4.28)$$

4.4 Computation of C and α in Calibration and Prediction Wells

I determine the uniaxial strain pore pressure buildup coefficient C and the thermal pressure coefficient α in each prediction well (Figure 4.1) using an effective medium approach.

I first determine the weight fractions of the mineral constituents using the x-ray diffraction (XRD) analyses. The XRD data from the wells presented in this chapter reveal that the rock primarily consists of quartz, illite, dolomite, and calcite (Table 4.2):

Constituent	Calibration Well Range (Wt. %)	Well "a" Range (Wt. %)	Well "e" Range (Wt. %)	Well "g" Range (Wt. %)	Well "h" Range (Wt. %)
Quartz	1-79	22-55	35-54	17-64	1-79
Illite	0-60	15-44	11-27	13-46	0-27
Dolomite	1-67	2-10	2-14	0-55	1-8
Calcite	1-88	0-50	2-36	0-48	1-92
Plagioclase	0-18	3-16	5-11	2-23	0-10
K-Feldspar	1-6	0-3	1-2	0-1.5	0-3
Apatite	0-16	0-1	0-1		
Barite	0-3				
Anatase	0-1		0-1		
Pyrite	0-8	1-4	1-2	1-5	0-4
Chlorite	0-14		0-1		
Muscovite	0-2				
Marcasite		0-1	0-1	0-1	
Sphalerite		0-3			

Table 4.2: Mineral ranges for each well. The mineral composition primarily consists of quartz, illite, dolomite, and calcite (lighter gray boxes).

I assume these 4 minerals constitute the mineral composition of the rock. I combine these with the measured total organic content TOC (kerogen) to determine the solid aggregate phase components of the rock. In the wells where there is an absence of measured TOC data, I estimate TOC from the x-ray fluorescence (XRF) XRF data using the following relationship:

$$TOC\ (wt.\%) = 0.046 * Ni(XRF\ ppm). \qquad (4.29)$$

I normalize the weight fractions of these components (quartz, illite, dolomite, calcite, and TOC) at the XRD depths such that the sum is 100%.

In the calibration well, I use Eq. 4.29 to determine TOC at the XRD depths. In wells "a" and "h," I utilize the TOC measurements acquired at the XRD depths. The individual normalized weight fractions are plotted in Figure 4.3.

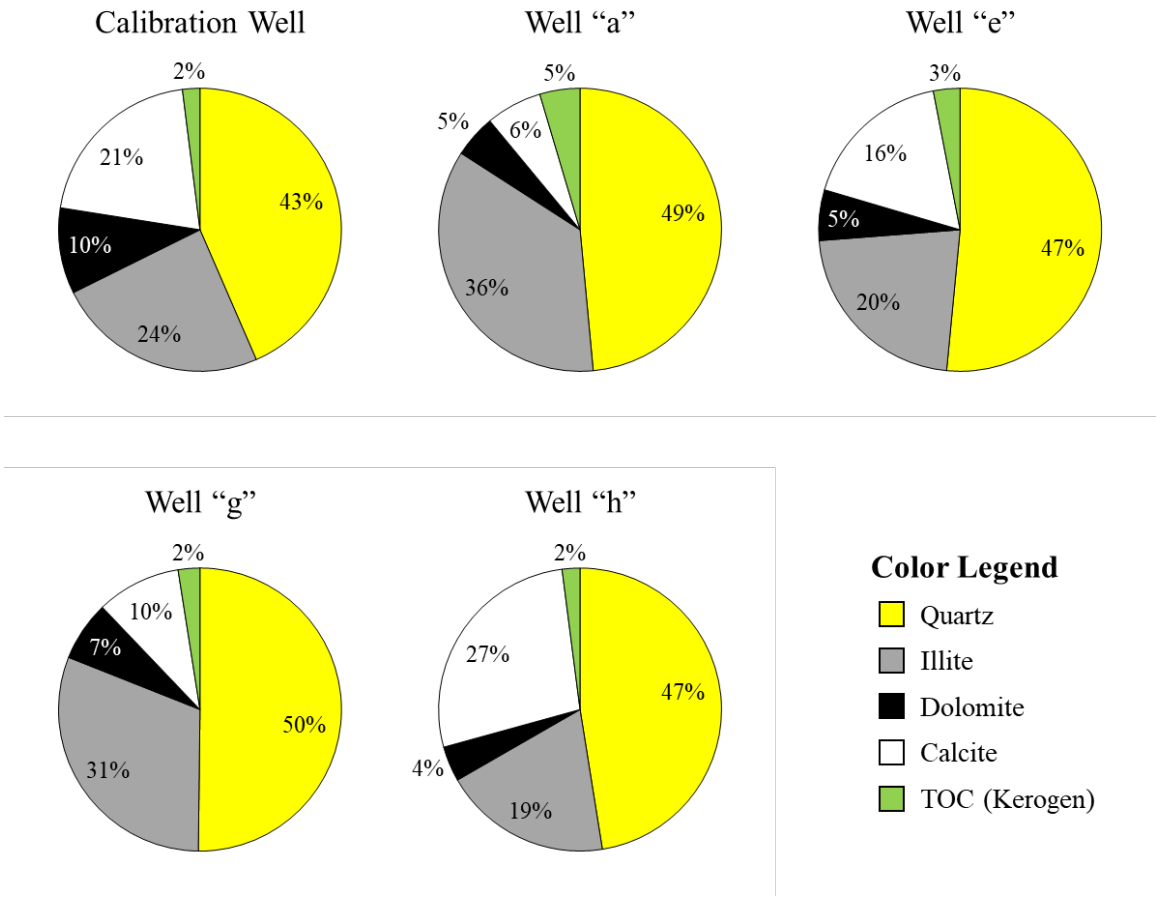

Figure 4.3: Solid aggregate phase composition of samples. The weight percent (wt.%) was individually determined in each well in and is determined from the XRD and TOC core measurements and represent an average value.

I next combine the normalized weight fractions with the corresponding compressibilities of the individual solid components to determine the Voight bound:

$$c_s[Voigt] = \sum_{i=1}^{N} f_i * c_{s,i}, \qquad (4.30)$$

and the Reuss bound:

$$c_s[Reuss] = \left[\sum_{i=1}^{N} \frac{f_i}{c_{s,i}}\right]^{-1}, \qquad (4.31)$$

where N represents the number of the solid components which comprise the solid aggregate phase (minerals + TOC), and f_i and $c_{s,i}$ represent the normalized weight fraction and the

compressibilty, respectively, of the *i*th solid component. (Refer to Chapter 3, Table 3.1 for compressibility values of the individual solid components.)

I then combine Eqns. 3.5 and 3.6 to calculate the Voigt-Reuss-Hill average compressibility of the solid aggregate phase:

$$c_s[VRH] = \frac{c_s[Voigt]+c_s[Reuss]}{2}. \quad (4.32)$$

The $c_s[VHR]$ determined in the calibration well and the prediction wells are tabulated in Table 4.3.

Parameter	Calibration Well	Well "a"	Well "e"	Well "g"	Well "h"
c_b (psi^{-1})	3.64E-07	3.18E-07	3.53E-07	3.73E-08	3.35E-07
$c_s[VRH]$ (psi^{-1})	1.85E-07	2.19E-07	1.88E-07	1.95E-07	1.88E-07
c_f (psi^{-1})	5.83E-06	5.27E-06	5.79E-06	9.15E-06	5.71E-06
ρ_f (g/cm^3)	0.77	0.68	0.74	0.73	0.89
n (%)	7.63	6.09	6.44	6.27	7.70
α_f (^{o}F^{-1})	3.28E-04	3.38E-04	3.19-04	3.33E-04	3.19-04

Table 4.3: Average parameters determined in each well. See text for computatoin of each parameter.

I determine the density of the solid aggregate phase (ρ_s) by summing the products of the normalized weight fractions and the respective densities of each component:

$$\rho_s = \sum_{i=1}^{N} f_i * \rho_i. \quad (4.33)$$

I calculate the in-situ fluid density (ρ_f) and fluid compressibility (c_f) using the Batzle and Wang (1992) equations for a gas saturated oil ("live oil") and brine fluid mixture. In these equations, I assume a pure water velocity of 1,500 m/s, a salinity of 100,000 ppm (Dvorkin et al., 2021), and a temperature gradient of 21.8 ^{o}C/km (Sinclair, 2007). For the oil API and the gas density, I obtain these values from each well's publicly available well test data; if a gas density is not provided, which in some well tests this number is not determined, I assume a value of 0.6 g/cm^3. For the oil and water saturations,

I use the average values that were independently determined by a commercial laboratory using the Dean Stark method (Luffel and Guidry, 1992) on test samples extracted from each well's core.

Next, I shift the wireline depths to match the core depths using the gamma ray curves. I then combine the wireline bulk density (ρ_b) with ρ_s and ρ_f to calculate porosity (n) using the mass-balance equation:

$$n = \frac{\rho_s - \rho_b}{\rho_s - \rho_f}. \tag{4.34}$$

The average porosity for each well is recorded in Table 4.3.

I calculate the dynamic bulk compressibility (c_b) from the shifted wireline velocities and bulk density using the following relationship (Fjaer et al., 2008):

$$c_b = \frac{1}{\rho_b\left(V_p^2 - \frac{4}{3}V_s^2\right)}, \tag{4.35}$$

where V_p is the P-wave velocity, V_s is the S-wave velocity, and ρ_b is bulk density. The average c_b determined in each well is shown in Table 4.3.

I then combine n (Eq. 2.16), $c_s[VRH]$ (Eq. 3.4), c_b (Eq. 3.3), and c_f (Batzle and Wang, 1992) to compute the Skempton's pore pressure buildup coefficient (denoted as $B_{comp.}$ to signify it is computed):

$$B_{comp.} = \frac{1}{1+\mathrm{n}\left(\frac{c_f - c_s}{c_b - c_s}\right)}. \tag{4.36}$$

Table 4.4 shows the average B computed in each well.

Parameter	Calibration Well	Well "a"	Well "e"	Well "g"	Well "h"
$B_{comp.}$	0.54	0.45	0.32	0.24	0.30
$C_{comp.}$	0.18	0.17	0.17	0.12	0.16
α (psi/^{o}F)	47.09	48.85	37.76	28.24	40.95

Table 4.4: Average values computed in each well. See text for description of parameters.

I map the computed Skempton's B ($B_{comp.}$) to the uniaxial strain pore pressure buildup coefficient C (which I denote as $C_{comp.}$ to signify it is computed) using the formula derived by Wang (2000a):

$$C = \frac{B(1+\nu_u)}{3(1-\nu_u)} \tag{4.37}$$

where ν_u is the undrained Poisson's ratio. I determine ν_u from the dynamic Poisson's ratio (ν_{dyn}) using the wireline P- and S-wave velocities (Fjaer et al., 2008):

$$\nu_{dyn} = \frac{V_p^2 - 2V_s^2}{2(V_p^2 - V_s^2)}. \tag{4.38}$$

with the assumption that velocity measurements reflect undrained rock deformation (Fjaer et al., 2008), hence $\nu_u = \nu_{dyn}$. The average $C_{comp.}$ determined in each well is listed in Table 4.4.

I lastly determine the thermal pressure coefficient α using Eq. 4.17. To compute the fluid expansion coefficient (α_f), I use a water expansion coefficient of 2.97E-04 $^oF^{-1}$ (Chiu, 1996), an oil expansion coefficient of 3.61E-04 $^oF^{-1}$ (Bearce and Peffer, 1916), and I multiply the respective coefficients by the water and oil saturations determine in each well; I then sum these together to determine α_f (Table 4.3). I assume a solid expansion coefficient of quartz, with α_s of 1.81E-05 $^oF^{-1}$ (Palciauskas and Domenico, 1982), and use the porosity, solid compressibility, and fluid compressibility tabulate in Table 4.3. The resultant α computed in each well is listed in Table 4.4.

Well	$B_{comp.}$	ν_u	C	Λ
Calibration well	0.54	0.21	0.18	0.33
Well "a"	0.45	0.24	0.17	0.30
Well "e"	0.32	0.23	0.17	0.39
Well "g"	0.24	0.20	0.12	0.37
Well "h"	0.30	0.21	0.16	0.34

Table 4.5: Mapping of Skempton's B to the uniaxial strain C. Λ is the relative ratio of the total undrained changes in pore pressure due to the mechanical effects (Eq. 4.20)

Error! Reference source not found. includes the relative ratio of the total undrained changes in pore pressure due to the mechanical and thermal effects (Λ; Eq. 4.20). In the calibration well, the relative ratio of mechanical to thermal effects on the total change in undrained pressure (Λ; Eq. 4.20) is 0.33. This means that 25% of the total changes in pore pressure are due to the mechanical effects, and the remaining 75% is due to the thermal effects. In well "a," Λ is 0.30; 23% of the total changes in pressure are due to mechanical, and 77% are due to thermal. In well "e," Λ is 0.39; 28% of the total changes in pressure are due to mechanical, and 72% are due to thermal. In well "g," Λ is 0.37; 27% of the total changes in pore pressure are due to mechanical, and 73% are due to thermal. Finally, in well "h," Λ is 0.34; 25% of the total changes in pressure are due to mechanical, and 75% are due to thermal.

4.5 Pore Pressure Prediction

4.5.1 Approach Incorporating C and α in each Prediction Well

I predict pore pressure in the wells shown in Figure 4.1 in the following way. First, I pick the mudrock depths, define the drained (hydrostatically pressured) and undrained (abnormally pressured) boundary, and estimate the amount of erosion (refer to Chapter 2 for the detailed process of picking the mudrock depths, defining the boundary, and estimating erosion).

I then predict pore pressure in the drained section using the approach documented in Chapter 2 and the parameters listed in Table 4.1.

Next, in the undrained interval, I use Eq. 4.28 with the mudrock velocities (picked in the undrained section), the parameters from Table 4.1 (except for C), and the erosion value (ΔH), the uniaxial strain pore pressure buildup coefficient (C), and the thermal

pressure coefficient (α) inferred in each prediction well (Table 4.4); for $\Delta T/\Delta Z$, I assume a temperature gradient of 0.012 ºF/ft (Sinclair, 2007). I refer to this approach as "Method 4."

For comparison, I also predict pore pressure in the undrained section by following a similar approach; however, I assume an α of 0; this eliminates consideration of the undrained changes in pore pressure due to temperature changes and only considers the undrained changes in pore pressure due to mechanical changes in stress (as defined by C). I refer to this approach as "Method 4*."

Furthermore, also in the undrained section, I include the pore pressure prediction results documented in Chapter 2. This approach predicts pressures from velocity using Eq. 4.14 with all the parameters listed in Table 4.1 (which are constrained in the calibration well). This method is in contrast to Method 4, since the C parameter is assumed constant across the basin and α is not included. I refer to this as "Method 1" (in chapter 2 I refer to this approach as "my approach").

4.5.2 Results

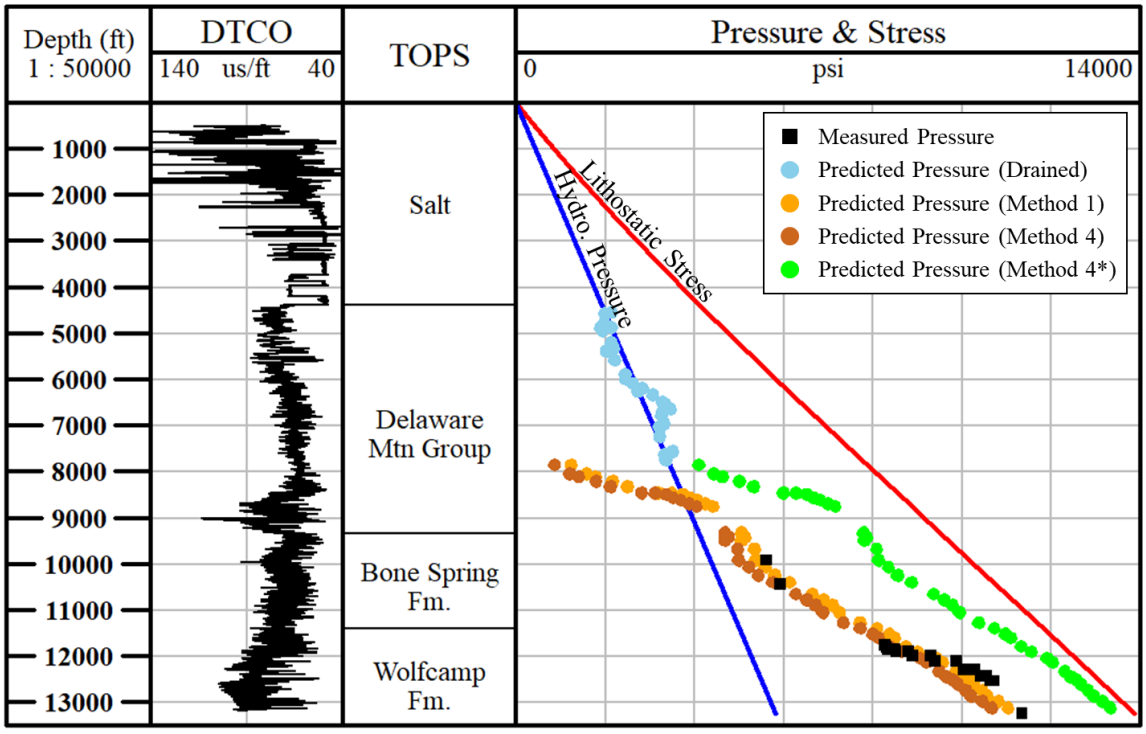

Figure 4.4: Calibration well pore pressure prediction. Blue dots represent the predicted pressures in the drained section; orange dots represent the predicted pressures with the assumption that C is constrained to the measured pressures in the calibration well and assumed constant across the basin with $\alpha = 0$; green dots represent predicted pressures using the computed C coefficient and with $\alpha = 0$; brown dots represent predicted pressures using the computed C and α coefficients (See Figure 4.1 for approximate location.)

In the calibration well, the drained predicted pressures (blue dots in Figure 4.4) are approximately hydrostatic above the drained/undrained boundary (~8,000 ft), after which there is a clear shift to the undrained predicted pressures.

In the undrained section, the predicted pressures of Method 4 (brown dots in Figure 4.4) are slightly less than Method 1 (orange dots in Figure 4.4). In contrast, Method 4* (green dots in Figure 4.4) systematically predicts higher pressures.

Directly below the drained/undrained boundary the predicted pressures of Method 4 are nearly ~2,000 psi below the hydrostatic pressures. Due to a lack of pressure data at these depths, it is not clear if the actual pressures in this interval are sub-hydrostatic; a discussion of these pressures is presented in Chapter 2. At approximately 8,500 ft, Method 4 predicts the onset of overpressure. Then for the remainder of the well, the predicted pressures are slightly lower than the measured pressures (black squares in Figure 4.4) by an average of 352 psi. In addition, for Method 4, the relative ratio of mechanical to thermal effects on the total change in undrained pressure (Λ; Eq. 4.20) is 0.33. This means that 25% of the total changes in pore pressure are due to the mechanical effects, and the remaining 75% is due to the thermal effects.

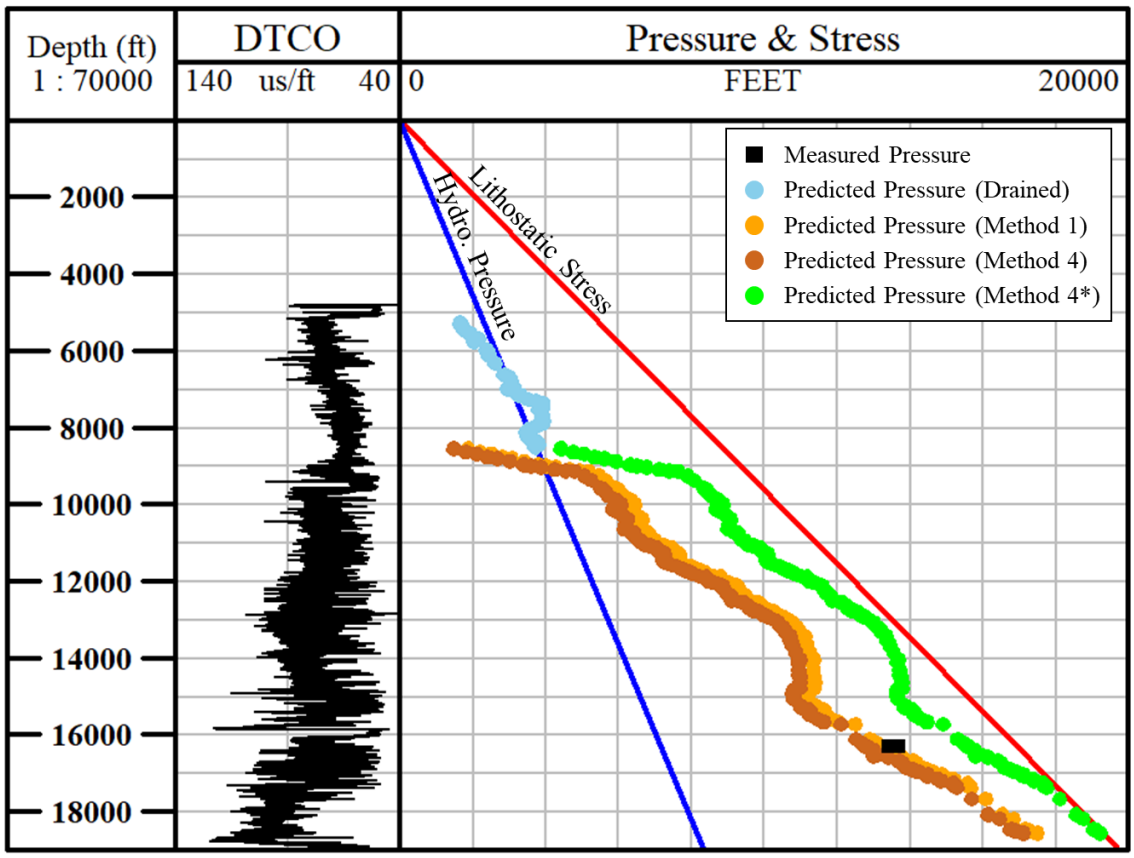

Figure 4.5: Well "a" pore pressure prediction. Blue dots represent the predicted pressures in the drained section; orange dots represent the predicted pressures with the assumption that C is constrained to the measured pressures in the calibration well and assumed constant across the basin with $\alpha = 0$; green dots represent predicted pressures using the computed C coefficient and with $\alpha = 0$; brown dots represent predicted pressures using the computed C and α coefficients (See Figure 4.1 for well location.)

I next explore the predicted pressures for well "a." Method 4 (brown dots in Figure 4.5) and Method 1 (orange dots in Figure 4.5) both predict the onset of overpressure at 9,000 ft, after which they predict a pressure gradient of ~5.00 psi/ft for the next ~500 ft, which is significantly in excess of the lithostatic gradient of 1.04 psi/ft. Then, from ~9,000 to 11,500 ft, both methods predict pressures that approximately follow the hydrostatic gradient of 0.44 psi/ft. The pressures then undulate from above the lithostatic gradient to

below the hydrostatic gradient until 15,000 ft. For the remainder of the well, the predicted pressures are in excess of the lithostatic gradient.

At ~16,500 ft, there are two measured pressures (black squares in Figure 4.5). Method 1 predicts pressures that are approximately 380 psi below the measured pressures, whereas Method 4 predicts pressures that are approximately 771 psi below the measured pressures. For the entirety of the well, Method 4 predicts slightly higher pressures than Method 1, and Method 4* (green dots in Figure 4.5) predicts the highest pressures. Lastly, for Method 4, the relative ratio of mechanical to thermal effects on the total change in undrained pressure (Λ; Eq. 4.20) is 0.30. Thus, 23% of the total changes in pore pressure are due to the mechanical effects, and the remaining 77% is due to the thermal effects.

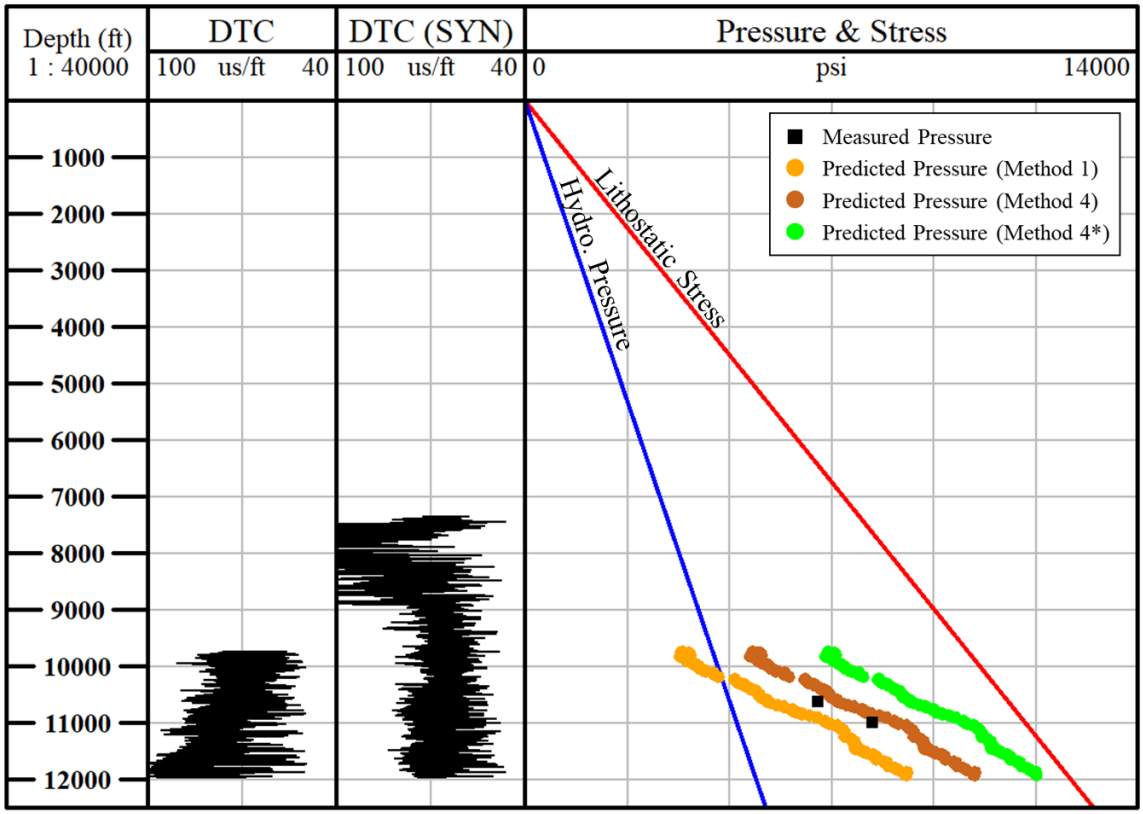

Figure 4.6: Well "g" pore pressure prediction. Blue dots represent the predicted pressures in the drained section; orange dots represent the predicted pressures with the assumption that C is constrained to the measured pressures in the calibration well and assumed constant across the basin with $\alpha = 0$; green dots represent predicted pressures using the computed C coefficient and with $\alpha = 0$; brown dots represent predicted pressures using the computed C and α coefficients (See Figure 4.1 for well location.)

In well "g," Method 1 (brown dots in Figure 4.6) predicts sub-hydrostatic pressures in the shallowest depths, whereas Method 4 (brown dots in Figure 4.6) predicts hydrostatic pressures. Then, for the remainder of the well, both predict pressures that trend toward the lithostatic stress gradient (red line in Figure 4.6).

At the shallowest measured pressure depth of 10,620 ft (black square in Figure 4.6), Method 1 predicts a pore pressure that is 1,100 psi below the measured pressure. At this depth, Method 4 predicts a pressure that is 436 psi above the measured pressure. Then, at the deeper measured pressure depth of 11,000 ft, Method 1 predicts a pore pressure that is

1,025 below the measured pressure, and Method 4 predicts a pore pressure that is 560 psi above the measured pressures. Like in the previous wells, Method 4* (green dots in Figure 4.6) predicts the highest pressures. For Method 4, the relative ratio of mechanical to thermal effects on the total change in undrained pressure (Λ; Eq. 4.20) is 0.37. Hence, 27% of the total changes in pore pressure are due to the mechanical effects, and the remaining 73% is due to the thermal effects.

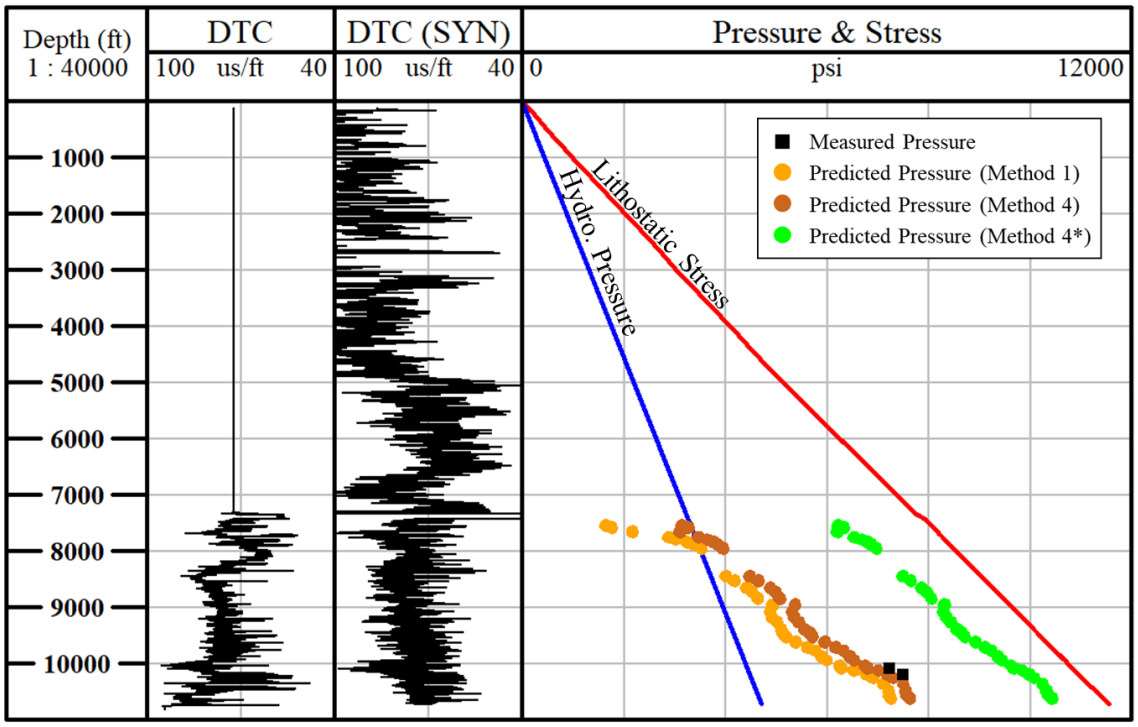

Figure 4.7: Well "h" pore pressure prediction. Blue dots represent the predicted pressures in the drained section; orange dots represent the predicted pressures with the assumption that C is constrained to the measured pressures in the calibration well and assumed constant across the basin with $\alpha = 0$; green dots represent predicted pressures using the computed C coefficient and with $\alpha = 0$; brown dots represent predicted pressures using the computed C and α coefficients (See Figure 4.1 for well location.)

Well "h" is the farthest from the calibration well. In the shallowest depths (~7,000—8,000 ft), Method 1 (orange dots in Figure 4.7) predicts pressures that are sub-

hydrostatic; this is in contrast to Method 4 (orange dots in Figure 4.7), which predicts the onset of overpressure at these depths. For the remainder of the well, both predict pressures that overall trend toward the lithostatic stress.

At approximately 10,000 ft there are two measured pressures (black squares in Figure 4.8). Method 1 predicts pressures that are ~830 psi below the measured pressures, and Method 4 predicts pressures that are ~367 psi below the measured pressures.

Method 4 predicts higher pressures than Method 1; however, the difference in this well is greater than in the previous wells. In the shallowest depth (7,500 to 9,200 ft) where both methods are predicting a relatively higher vertical effective stress, the average pressure difference is 900 psi, and for the remainder of the well (9,200 to 10,600 ft) where both methods are predicting a relatively lower vertical effective stress, the average pressure difference is 735 psi. For the entirety of the well Method 4* (green dots in Figure 4.7) predicts substantially higher pressures than Methods 1 and 4. Finally, for Method 4, the relative ratio of mechanical to thermal effects on the total change in undrained pressure (Λ; Eq. 4.20) is 0.34. Thus, 25% of the total changes in pore pressure are due to the mechanical effects, and the remaining 75% is due to the thermal effects.

4.6 DISCUSSION

In this discussion, I evaluate the sensitivity of my pore pressure prediction approach by varying the parameters that are assumed: A and B.

4.6.1 Sensitivity of A and B Parameters

A and B, which were introduced in Chapter 2, are lithology-dependent parameters that define the mudrock normal compaction path:

$$V = 5000 + A\sigma_v'^{B}, \tag{4.39}$$

where V is velocity; A and B are the same parameters in Eq. 4.28.

As documented in Chapter 2, A and B are assumed from the normal compaction behavior of illitic mudrocks (Heppard and Ebrom, 2010) and assumed constant. This yields A = 14.00, B = 0.73, and a calibrated U of 10 (Table 4.1).

I explore the predictive capability of my approach in well "a" by increasing both A and B first by 2.0%, then by 3.5%. With an increase of 2.0%, this yields A = 14.28, B = 0.74, a resulting U of 3.6 (constrained in the drained section of the calibration well), and an erosional value of 5,007 ft (determined in prediction well "a"); increasing these by 3.5% yields A = 14.49, B = 0.76, a U of 2.0 (also constrained in the drained section of the calibration well), and an erosional value of 4,012 ft (also determined in prediction well "a").

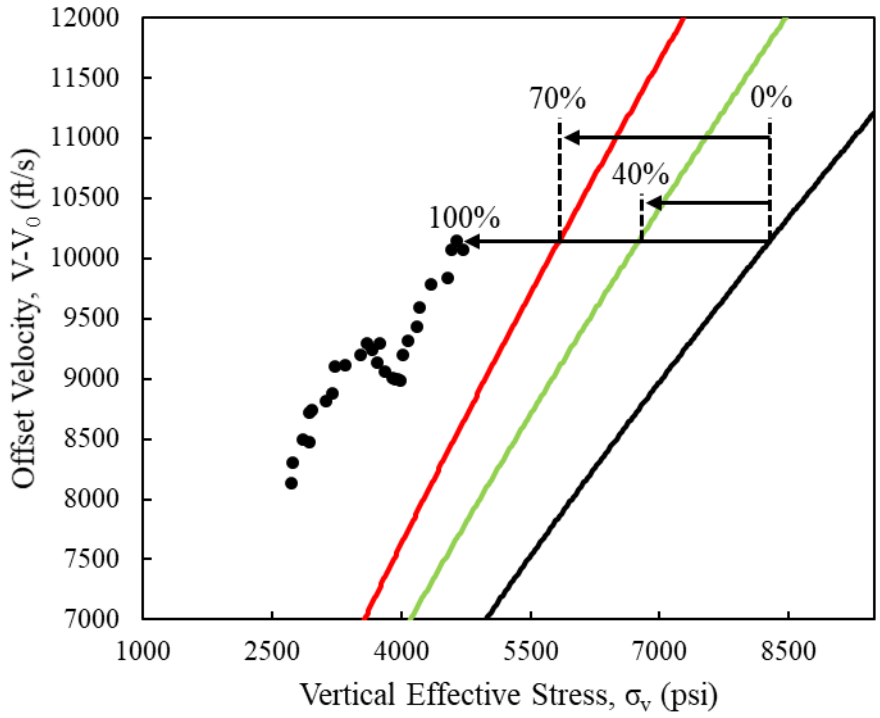

Figure 4.8: Normal compaction curves well with various A and B values. The black curve represents the values assumed from illitic mudrock with A = and B = 0.73 (Table 4.1). The green curve represents an increase of 2.0%, yielding A = 14.28 and B = 0.74; this curve is approximately 40% between the black curve and the measured pressures (black circles). The red curve represents an increase of 3.5%, yielding A = 14.49 and B = 0.76; this curve is approximately 70% between the black curve and the measured pressures.

Although the A and B increase of 2.0% and 3.5% might seem small, it results in a significant shift in the normal compaction curves (green curve represents an increase of 2.0% and red curve represents an increase of 2.5%, respectively, in Figure 4.8), with the changes in B having a much larger affect on the shift in the normal compaction curve than changes in A. The increase of 2.0% shifts the normal compaction curve to approximately 40% of the way from the curve with the prior assumed A and B values (black curve in Figure 4.8) to σ_v' determined from the drained pressures in the calibration well (black dots in Figure 4.8); likewise, the increase of 3.5% shifts the curve to approximately 70% from

the curve with the prior assumed A and B values to σ_v' determined from the drained pressures.

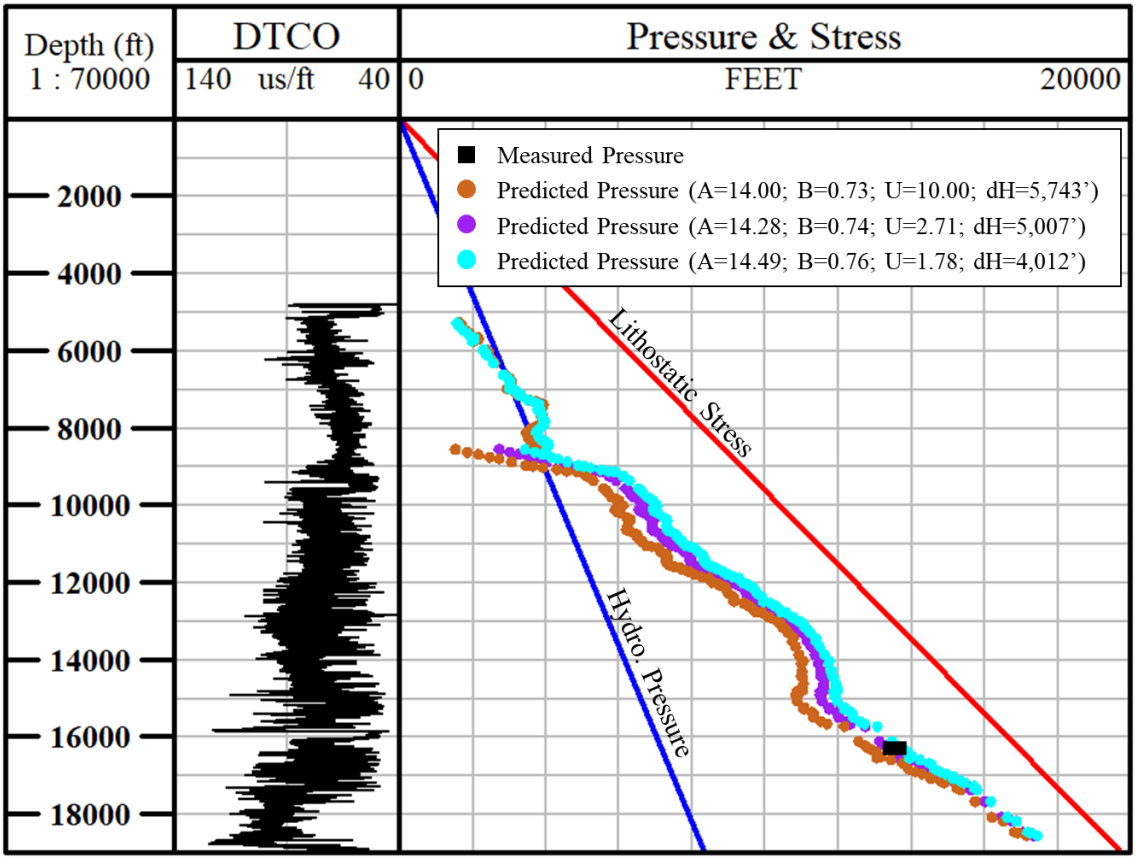

Figure 4.9: Prediction well "a" with various A and B values. The A, B, U, and ΔH values are listed in the figure; in each prediction, C = 0.30 and α = 39.16 (Table 4.3).

In prediction well "a" with the A and B increase of 2.0% (A = 14.28, B = 0.74, U of 2.71, and ΔH of 5,007 ft) and the increase of 3.5% (A = 14.49, B = 0.76, U of 1.78, and ΔH of 4,012 ft), the predicted pore pressures are similar to the predicted pressures with the values previously assumed and determined (A = 14.00, B = 0.73, U of 10.00, and ΔH of 5,743 ft), as shown in Figure 4.9. With respect to the measured pressures (black squares in Figure 4.9), the previously assumed values of A and B predicts pore pressures (brown dots

in Figure 4.9) that are approximately 220 psi less than the measured pressures. With the 2.0% increase in A and B, the predicted pressures (purple dots in Figure 4.9) are 125 psi below the measured pressures. Lastly, with the 3.5% increase in A and B, the predicted pressures (cyan dots in Figure 4.9) are 200 psi above the measured pressures.

The results show that, despite the significant shift in the normal compaction curve with various A and B values, the predicted pore pressures change very little. This is because with each different A and B value, a new U value is constrained in the calibration well to compensate for the shift in the normal compaction curve, and this value is smaller so that the slope of the unloading curve is steeper, and a new erosion value (ΔH) estimated in the prediction well. Thus, while U and ΔH are sensitive to A and B, the predicted pore pressure are not.

4.7 CONCLUSIONS

I have demonstrated how to refine the undrained pore pressure prediction model presented in Chapter 2 with the uniaxial pore pressure buildup coefficient C and the thermal pressure coefficient α determined in each prediction well. Both C and α are determined using an effective medium approach from petrophysical data. This approach accounts for the undrained changes in pore pressure in a basin that has experienced uplift (thermal effects) and erosion (mechanical effects), and thus captures the underlying physics of the mudrock behavior. I presented this approach in a calibration well and four prediction wells. In each of the wells, my approach successfully predicts the pore pressures. A summary of the results is as follows:

1. Calibration well: Predicted pressures are, on average, 352 psi less than the measured pressures. The relative ratio of the mechanical to thermal undrained changes in pore pressure (Λ) is 0.61; this means that 38% of the total changes

in pore pressure are due to the mechanical effects, and 62% is due to the thermal effects.

2. Well “a”: Predicted pressure are, on average, 771 psi less than the measured pressures. Λ is 0.53; 35% of the total changes in pore pressure are due to the mechanical effects, and 65% is due to the thermal effects.
3. Well “g”: Predicted pressure are, on average, 499 above the measured pressures. Λ is 0.68; 40% of the total changes in pore pressure are due to the mechanical effects, and 60% is due to the thermal effects.
4. Well “h”: Predicted pressure are, on average, 367 psi less than the measured pressures. Λ is 0.51; 34% of the total changes in pore pressure are due to the mechanical effects, and 66% is due to the thermal effects.

I also demonstrated the sensitivity of the A and B parameters. Although small changes in these parameters (especially B) can significantly shift the position of the normal compaction curve, the predicted pore pressures, regardless of A and B, remain relatively consistent. This is because when A and B are changed, a new U is subsequently constrained in the drained section of the calibration well, and new erosion values are accordingly determined in the prediction wells.

Appendix A: Chapter 2 Additional Results

In this appendix, I provide the estimated erosion values and the estimated drained/undrained boundaries for the wells that are presented in Chapter 4 but are not included in Chapter 2; I also predict pore pressure in these wells. The approaches I used to determine these are fully described in Chapter 2.

A.1 Estimated Erosion and Drained/Undrained Boundary

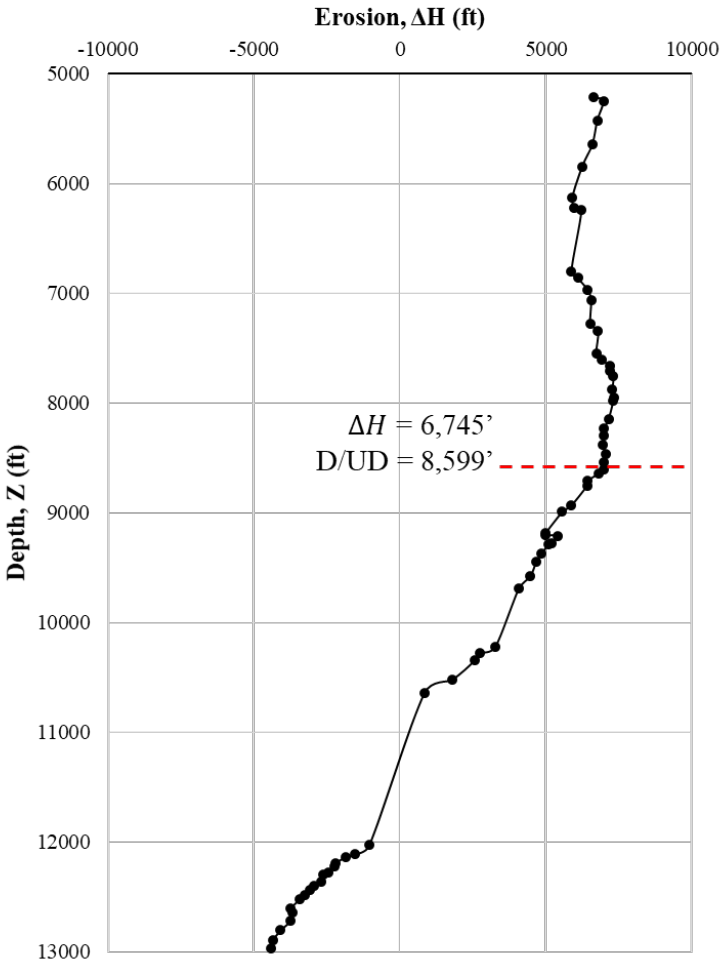

Figure A.1: Well "e" estimated erosion. The approach to define the drained/undrained (D/UD) boundary and the erosion value is describe in Chapter 2.

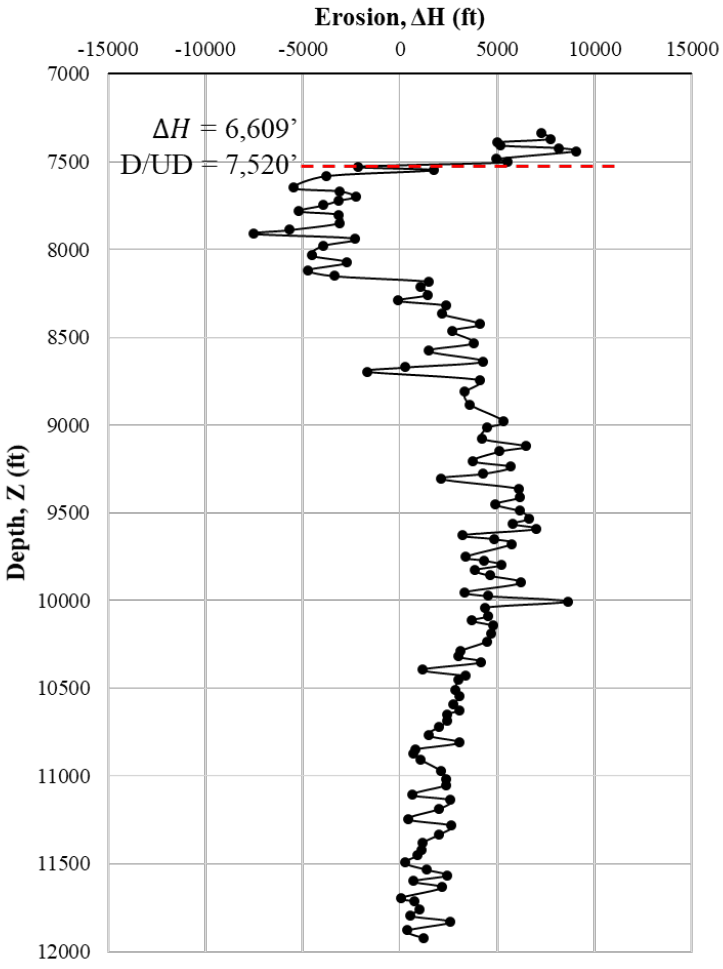

Figure A.2: Well "g" estimated erosion. The velocities used in the computation of erosion (ΔH) for this well are derived from the wireline density log (refer to Appendix E). The approach to define the drained/undrained (D/UD) boundary and the erosion value is describe in Chapter 2.

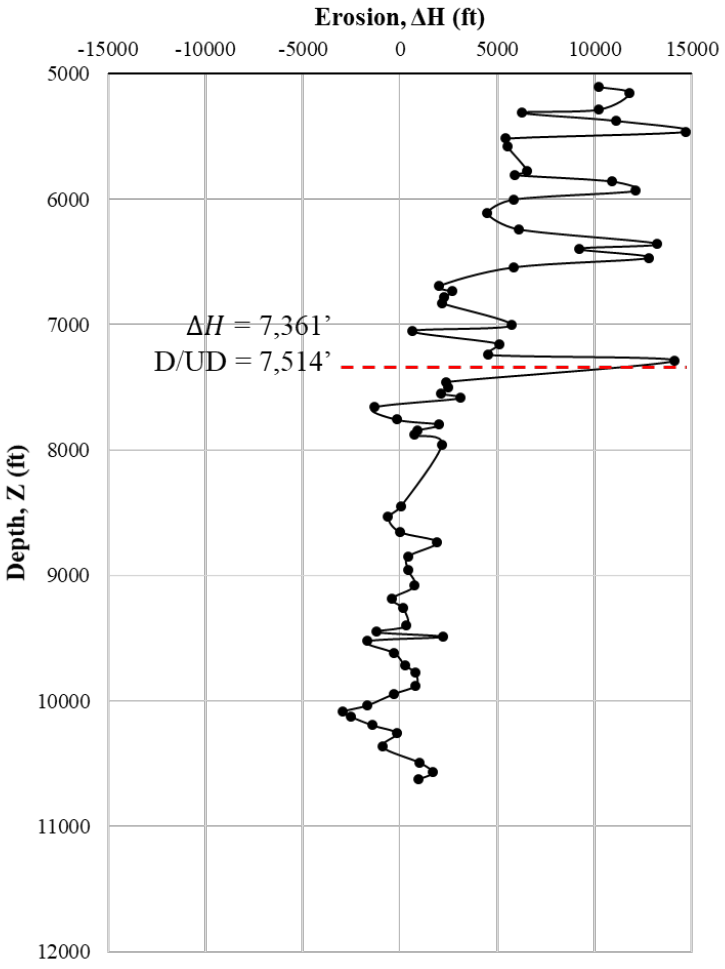

Figure A.3: Well "h" estimated erosion. The velocities used in the computation of erosion (ΔH) for this well are derived from the wireline density log (refer to Appendix E).

A.2 Pore Pressure Prediction

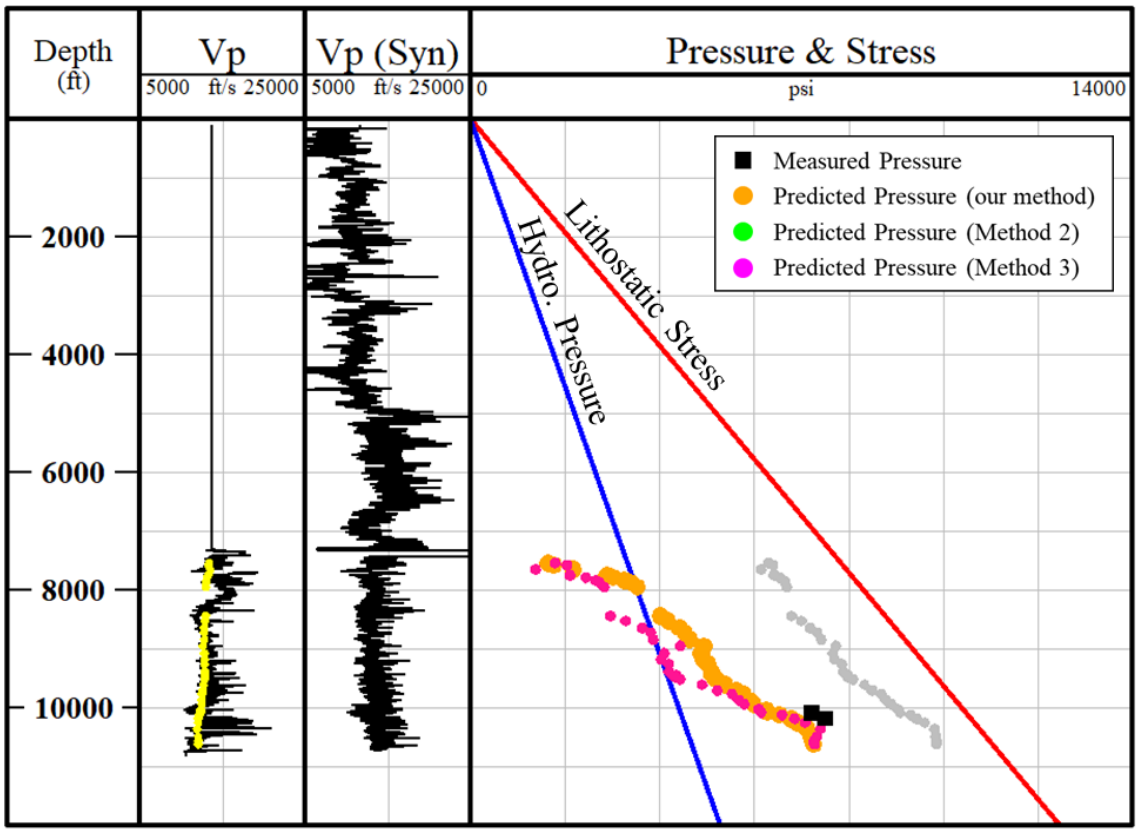

Figure A.4: Well "h" pore pressure prediction. See Chapter 2 for "my method," "Method 2," and "Method 3."

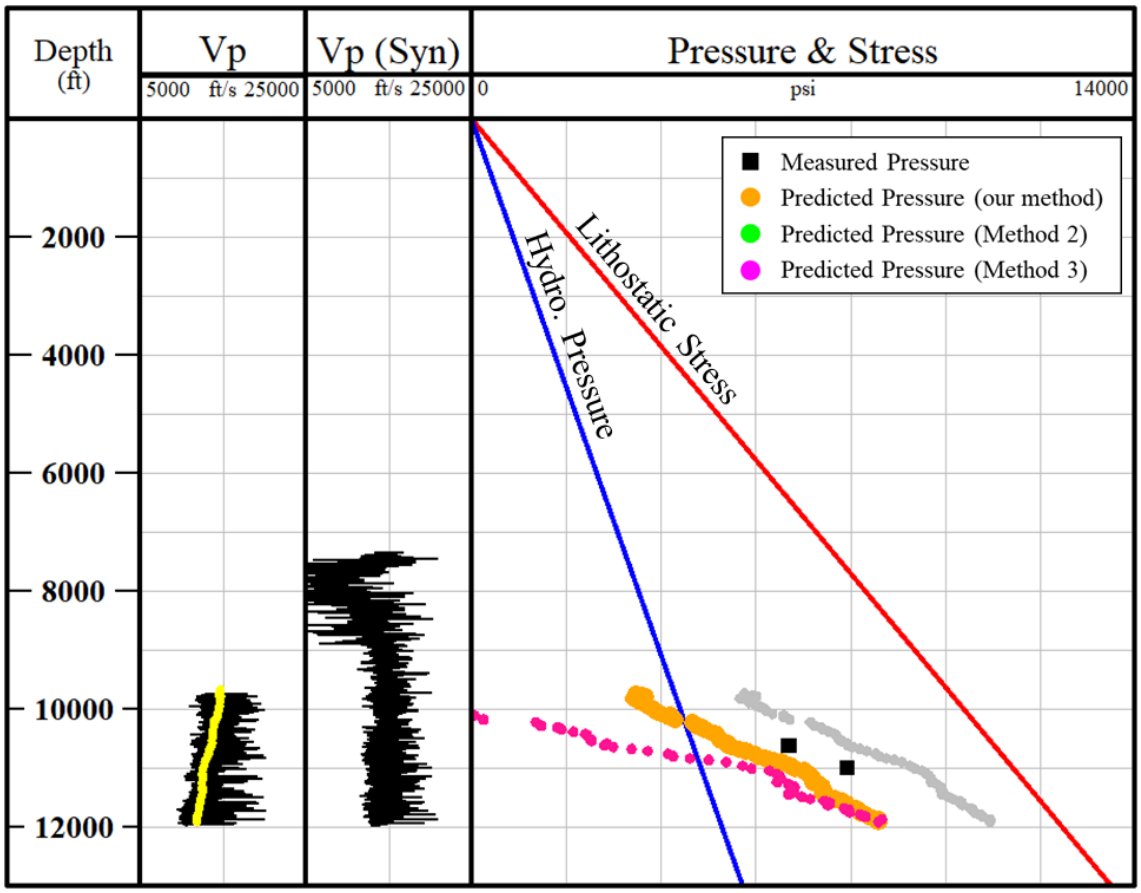

Figure A.5: Well "g" pore pressure prediction. See Chapter 2 for "my method," "Method 2," and "Method 3."

Appendix B: Determining System Compressibility

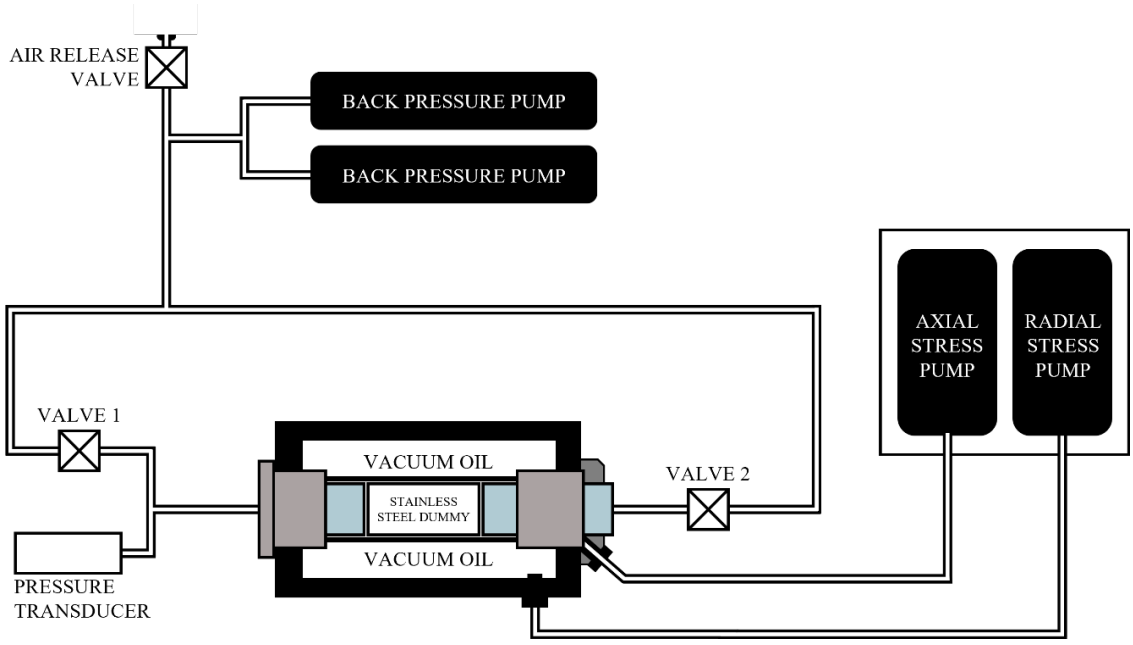

Figure B.1: Schematic depiction of the experimental system used to measure B. A correction is applied to account for the components of the system that expand as a result of an increase in fluid pressure in the fluid lines. These comprise the fluid lines, the drainage valves, and the pore pressure transducer.

The equation for correcting the experimentally measured Skempton's B coefficient ($B_{meas.}$) measured in a system that is not perfectly rigid is:

$$B_{corr.} = \frac{1}{\frac{1}{B_{meas.}} - \frac{V_L}{V} * \frac{c_f}{c_b - c_s} - \frac{c_L + c_M}{V(c_b - c_s)}} \qquad \text{(B.1)}$$

Application of this equation requires the expansion of the measuring system $c_L + c_M$, in which the dimensions are defined as the change in volume per unit change in pressure. This is determined by measuring the fluid volume required to increase the pressure within the fluid lines to 3,000 psi, and subtracting from this the amount of volume by which the fluid in the fluid lines compresses. The resulting volume divided by the pressure increase of 3,000 psi yields $c_L + c_M$.

The steps to measure $c_L + c_M$ are as follows. First, a stainless steel dummy with a small hole bored radially through its center and with a size approximate to that of the samples measured in this study is inserted into the triaxial cell. Since the rigidity of stainless steel is 16-17 times greater than the rigidity of a typical mudrock, it is assumed that the compressibility of the stainless steel dummy is negligible, and the only volume changes are thus a function of the fluid lines, the fluid in the fluid lines, the valves, and the pressure transducer.

Then, two test are performed. The first involves pressuring the system with the drainage valves open, and the second is with the drainage valves closed. During both tests, the back pressure pump is raised from 100 psi to 3,000 psi at a rate of 25 psi/min while an effective stress (controlled by the axial and radial stress pumps) of 1,000 psi is maintained. A plot of the results is shown in Figure B.2.

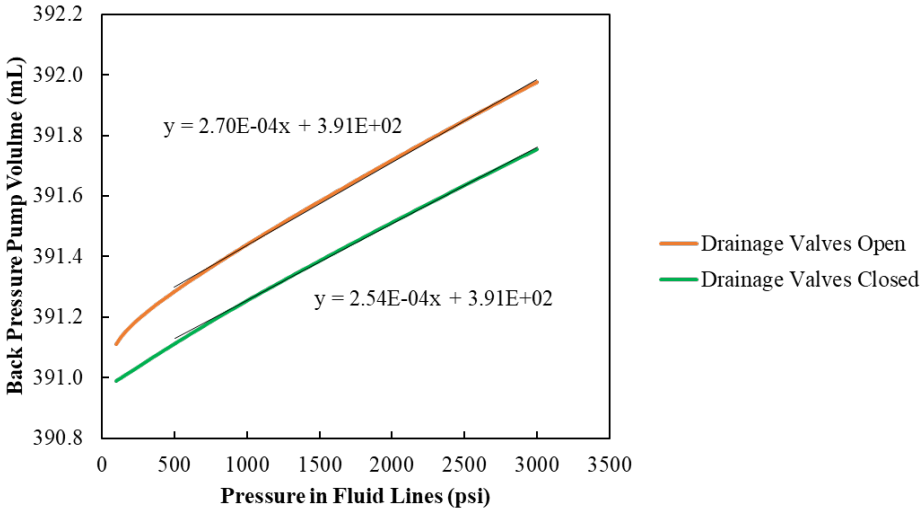

Figure B.2: Pump volume change. Both lines represent the change in back pressure pump volume as the pressure is increased from 100 psi to 3,000 psi. The upper orange line represents the test run with the drainage valves open, and the lower green line the drainage valves closed. The difference in slopes (not shown) yields the rate for the system contained within the bounds of the drainage valves.

A line of best fit is then determined for each test over an interval that is approximately linear. For both tests, this was determined between the pressure range of 500 psi to 3000 psi. The slope with the valves open is 2.70E-04 mL/psi, and the slope with the valves closed is 2.54E-04 mL/psi.

Next, the difference of the slopes is computed to estimate the rate of change of the total volume of the system contained within the bounds of the drainage. This comprises the terms involving the expansion of the fluid lines, the drainage valves, and the pore pressure transducer, as well as the volume reduction of the fluid in the fluid lines. The resulting value is 1.61E-05 mL/psi (represented by the black line in Figure B.3).

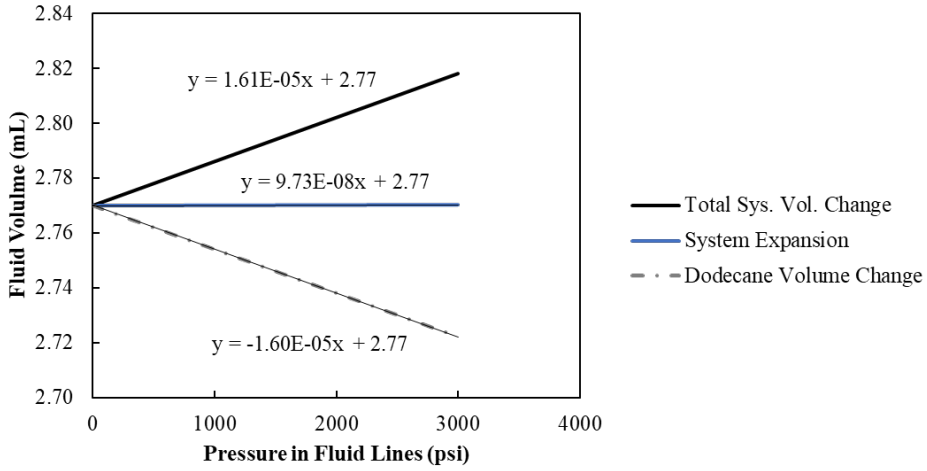

Figure B.3: Measurement of system compliance. Each line represents the change in volume within the bounds of the drainage valves (Figure B.1) as the fluid pressure is increased from 0 psi to 3,000 psi. The upper black line represents the change in total volume of the system (comprising the fluid lines, drainage valves, pore pressure transducer, and the fluid), the lower gray dash dot line represents the change in volume of the fluid (dodecane) in the fluid lines, and the middle blue line represents the change in volume of the measuring system (comprising the fluid lines, drainage valves, and pore pressure transducer).

Subsequently, the rate at which the fluid volume in the fluid lines changes as the pressure is increased from 0 psi to 3,000 psi is determined. Given the equation for fluid compressiblity:

$$c_f = \frac{-1}{V_i}\left(\frac{\Delta V}{\Delta u}\right) \tag{B.2}$$

where V_i is the initial volume, ΔV is the change in volume ($\Delta V = V_f - V_i$), and Δu is the change in pressure ($\Delta u = u_f - u_i$), the amount of volume by which the fluid in the fluid lines is reduced over a change in pressure can be computed as:

$$V_f = V_i\left(1 - c_f \Delta u\right) \tag{B.3}$$

The initial fluid volume within the bounds of the drainage valves V_i is 2.770 mL, and the compressiblity of dodecane at a pressure of 1,000 psi (which is congruent to the pore pressure at which the B tests in this study were performed) and a temperature of 30 deg. C is c_f = 5.76E-06 psi^{-1} (dos Santos Junior et al., 2022). Hence, as the pressure is increased from 0 psi to 3,000 psi, the fluid volume is reduced to 2.722 mL, and the rate at which the fluid volume in the fluid lines changes is thus -1.60E-05 mL/psi (represented by the gray line in Figure B.3).

Finally, the terms comprising the expansion of the measuring system $c_L + c_M$ (fluid lines, drainage valves, and pore pressure transducer) are computed as the sum of the rate of the total volume change (the fluid lines, drainage valves, pore pressure transducer, and the fluid volume) and the rate of volume change of the fluid in the fluid lines (it is the sum because as the fluid pressure in the drainage lines is increased, the fluid compresses and the measuring system expands). The result is $c_L + c_M$ = 9.73E-08 mL/psi (represented by the blue line in Figure B.3).

Appendix C: Mineral & TOC Models

C.1 Introduction

X-Ray Fluorescence (XRF) and X-Ray Diffraction (XRD) analyses were collected on the core presented in this study. The XRF provided the concentration of 27 elements using Niton 950t Goldd+ hand-held XRF analyzer in mining mode across the entire core at 0.5 ft sample spacing. The XRD was analyzed on selected sections of the core to document the mineral content, and the TOC was analyzed from rotary sidewall samples.

Constituent	Range (%)
Quartz	6-64
K-Feldspar	0-3
Plagioclase	0-10
Calcite	1-92
Dolomite & Fe-Dolomite	1-8
Aragonite	0-0
Pyrite	0-4
Sphalerite	0-0
Illite/Smectite *	0-8
Illite & Mica	0-27
Chlorite	0-0
Kerogen	0.4-11.2

Table C.1: Mineral content from XRD analyses and total organic content. * Mixed-layer illite/smectite contains 10-20% smectite layers.

C.2 Mineral Model

XRD analysis shows that the bulk mineralogy predominantly consists of dolomite, calcite, illite, and quartz. A mineral model is developed to estimate these minerals from the XRF element content (wt.%) using the following stoichiometric relationships and published molecular weight percentages of potassium and silicon in illite:

1. Magnesium (Mg) comprises 13.18% of dolomite ($CaMg(CO_3)_2$), thus:

$$Dolomite\ wt.\% = \frac{Mg\ (XRF\ wt.\%)}{13.18\%} \quad \text{(C.1)}$$

2. Calcium (Ca) comprises 21.73% of dolomite and 40.04% of calcite ($CaCO_3$), thus:

$$Calcite\ wt.\% = \frac{[Ca\ (XRF\ wt.\%)] - [21.73\% * dolomite\ wt.\%]}{40.04\%} \quad \text{(C.2)}$$

3. Potassium (K) comprises 8.75% of illite (Weaver, 1965), thus:

$$Illite\ wt.\% = \frac{K\ (XRF\ wt.\%)}{8.75\%} \quad \text{(C.3)}$$

4. Silicon (Si) comprises 24.44% of illite (using the illite formula presented by Rieder et al. (1998): $K_{0.65}Al_2(Al_{0.65}SI_{3.35}O_{10})(OH)_2$) and 46.74% of quartz ($SiO_2$), thus:

$$Quartz\ wt.\% = \frac{[Si\ (XRF\ wt.\%)] - [24.44\% * illite\ wt.\%]}{46.74\%} \quad \text{(C.4)}$$

Application of the mineral model on the section of core where XRF and XRD data were collected demonstrate a successful correlation. The correlation with the highest amount of scatter is dolomite ($R^2 = 0.80$), whereas the weakest correlation is found in illite; here it is assumed that the clay content only consists of illite. The mineral model predicts a slightly lower weight percent of illite that is on average 4% less than in the intervals where the XRD clay content is above 30%. In the remaining intervals, the model predicts a weight percent of illite that is within 2% of the XRD-measured clay content.

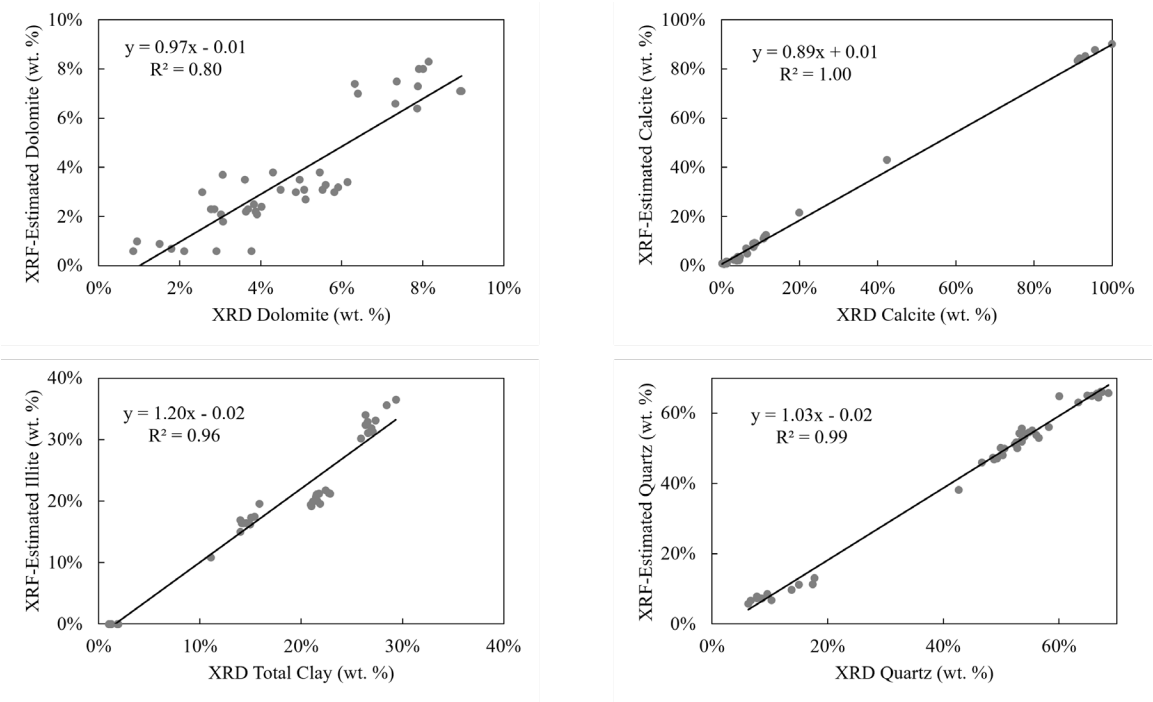

Figure C.1: Results of mineral model (XRF-estimated) vs. actual mineral content analyzed by XRD. The gray circles represent mineral content determined by XRD analysis.

C.3 TOC MODEL

Various trace elements such as bromine, molybdenum, nickel, uranium, and vanadium have been recognized as a proxy of TOC in source rocks (Mayer et al., 1981; Tribovillard et al., 2006). A simple model is developed to estimate TOC from XRF element concentration. TOC (wt. %) is cross-plotted against each aforementioned trace element (wt. %), of which vanadium (V) exhibits the strongest correlation (R^2 = 0.83). The following relationship is then established, as shown in Figure C.2:

$$TOC\ wt.\% = 239 * V(XRF\ wt.\%) \qquad \text{(C.5)}$$

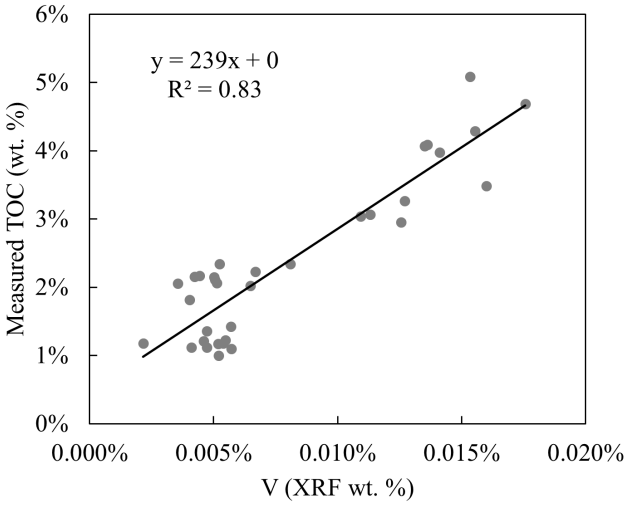

Figure C.2: Cross-plot of vanadium (V) as measured by XRF (wt. %) vs. total organic content (TOC) (wt. %). The gray circles represent TOC measurements.

Appendix D: Experimental Apparatus, Detailed Procedure to Measure Skempton's *B*, & Skempton's *B* Interpretation

D.1 Experimental Apparatus

The experimental apparatus used to measure the Skempton's pore pressure buildup coefficient *B* is schematically depicted in Figure D.1. The apparatus was designed for the original purpose of permeability measurements. I adapted it to measure Skempton's *B* by closing the fluid line drainage valves (valves 1 and 2 in Figure D.1) and superimposing an incremental change in confining stress on a pre-existing state of confining stress and pore pressure. I conducted all tests in this dissertation with the experimental cell housed inside a climate-controlled cabinet set to 28ºC (±0.5ºC).

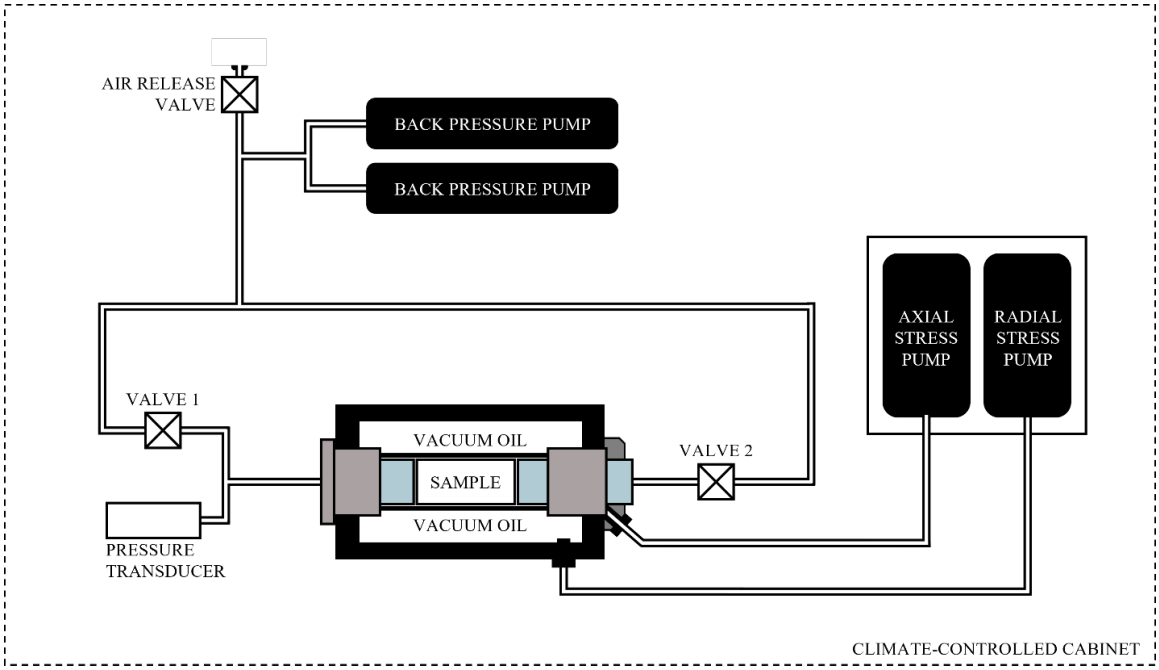

Figure D.1: Schematic depiction of experimental equipment for B tests. The equipment is housed in a climate-controlled cabinet.

D.2 CONFINING STRESS

The system is configured to allow for independent control of the radial and axial stresses. The radial stress is created inside the annular space of the core holder. The working pressure of the core holder is 10,500 psi. A positive displacement pump is used to inject the pressurizing fluid (vacuum oil) into the vessel. A 70 Durometer Viton sleeve (0.2 in. thick) isolates the pressurizing fluid from the sample. The axial stress is controlled by a movable piston driven by a second positive displacement pump. Both pumps have a working pressure of 10,000 psi and a flow rate resolution of 0.000031 mL/min.

D.3 PORE PRESSURE

The endcaps, one of which contains the movable piston, are connected to the pore fluid lines. A small hole is bored through the center of each endcap to facilitate transmission of the pore fluid (dodecane) into the sample. The pore pressure is controlled by a pair of positive displacement pumps with a working pressure 6,000 psi and a flow rate resolution of 0.001 mL/min. A fluid line valve is located on each side of the vessel to allow the system to be isolated from the pore pressure pumps. A pore pressure transducer with a measuring range of 0-5,000 psi with 0.04% full scale accuracy is connected between the fluid line valve and fluid line connected to the fixed endcap. The fluid line volume contained between the fluid line valves, the pressure transducer, and the sample is 2.77 mL.

D.4 TEST SAMPLES

The first step is to extract a cylindrical sample with a diameter of 1-inch from intact core using an air-cooled drill press. Next, cut the sample's length to approximately 1.25" using a gravity-fed tabletop cutter. It is recommended to have a professional service with ample experience to perform the extraction and cutting steps, since the samples are prone to breaking.

Then, sand the ends of the sample until a tolerance of ± 0.05 mm measured at any given point along the sample's length can be achieved. Once done, measure the sample's exact dimensions with digital calibers to determine bulk volume, then measure the sample's dry mass. Next, image the sample using high resolution X-ray computed tomography (CT). (CT images were conducted at the University of Texas High-Resolution X-Ray Computed Tomography Facility. The reader is referred to Appendix C.3.2 in Ramiro-Ramirez (2022) for detailed instructions on how to visualize the CT images.)

Prior to the placing the sample into the experimental triaxial cell, the sample must be evacuated and subsequently saturated with dodecane inside a vacuum chamber. A schematic depiction of the experimental equipment used for this is seen in Figure D.2. This is done by first placing the sample into a glass beaker. Place the beaker with the sample inside into the vacuum chamber such that it would lie directly below the liquid deliver valve attached to the chamber lid. Wet the rim of the vacuum chamber lid and place it onto the vacuum chamber. Open the liquid delivery valve and the vacuum pump valve, close the dodecane valve, and subject the sample to a vacuum for 5 minutes. Next, close the vacuum pump valve, open the dodecane valve, and proceed to slowly open the liquid delivery valve attached to the chamber lid. Continue this until the sample is fully immersed in dodecane, after which close the liquid delivery valve. Give a period of 24 hours to facilitate imbibition, then remove the sample and record its wet mass.

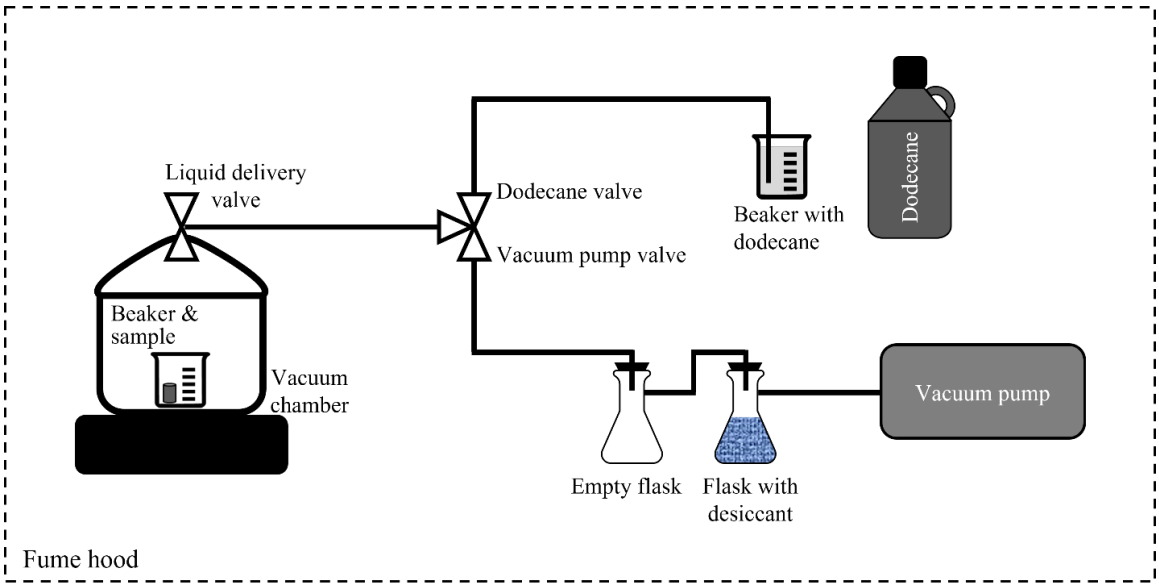

Figure D.2: Schematic depiction of experimental equipment for initial saturation. The equipment is contained within a fume hood.

D.5 Experimental Procedure

Before the sample is placed into the experimental cell (immediately following initial saturation), the downstream axial displacement piston must be fully retracted by inserting a steel plug into the cell and tightening the upstream endcap with a pin spanner wrench until the piston can no longer retract. Then, replace the steel plug with the initially saturated sample, and fit the upstream endcap onto the core holder. Hand-tightened it until it comes in contact with the sample. Then, unscrew the retainer by ~2-3 threads.

With the sample inside the core holder, the first step is to displace any air trapped inside the fluid lines. Operate the pore pressure pump (operating mode is set to IND. CP-C) at a pressure of 25 psi with one fluid line valve open and the other closed (e.g., valve 1 open and valve 2 closed, as seen in Figure D.1). Continue this while closely monitoring the cell until dodecane begins to drain from the vessel. After sufficient efflux is observed (~2-5 mL), open the fluid line valve that was previously closed and close opposite fluid line

valve that was previously opened. The pore pressure pump should continue to remain running. Monitor the cell until dodecane can once again be observed draining from the vessel. At this point, with the pore pressure pump still running, reopen the closed fluid line valve (such that both fluid line valves are now open), and operate the pump that controls that axial stress at a pressure set to 44 psi (operating mode set to INC. CP-C). Note that once the piston comes into contact with the sample, the axial stress will build up pressure very quickly. The pump is stopped and restarted once the desired value is achieved to prevent the stress from exceeding the prescribed amount. This is an important step that is carried out every time the stress or pore pressure is manually prescribed.

Once the axial stress has reached a pressure of 44 psi, increase it to 88 psi. At this point, it should no longer be possible to tighten the endcap any further. This confirms that the piston is in contact with the sample. Next, increase the axial stress to a pressure of 200 psi (operating mode set to INC. CP-C), and increase the pore pressure to a pressure of 50 psi. Closely monitored both pumps during this time to prevent the pressures from exceeding their prescribed values. (Note that for this system configuration, a uniform isotropic stress is achieved with an axial stress that is 44% of the radial stress. Henceforth, the isotropic stress state will be denoted by the specified confining stress, which corresponds to the magnitude of the radial stress. For instance, if the confining stress is noted as 500 psi, this implies a radial stress of 500 psi and an axial stress of 220 psi. All subsequent testing procedures listed below are conducted under this uniform isotropic stress state.)

Once all the pumps have reached a stable value, purge any potential air remaining in the fluid lines using the pore fluid line bleeding valve. This is done by slowly opening the pore pressure bleeding valve until a small amount of fluid (~3-5 drops) begins to drain

from the fluid line drainage outlet, upon which the valve is immediately closed. Repeat this process 2-3 times to ensure the fluid lines are completely saturated with dodecane.

The final stage of sample saturation is achieved by subjecting the sample to a pore pressure of 750 psi and a confining stress of 1,000 psi for a period of 5 days. It is imperative to operate the pumps during this stage using the "Set Up and Control Ramping Operation" feature in PumpWorks to increase the pressures at a rate of 25 psi/min. This prevents the pressure and stress from exceeding the prescribed amount.

Finally, verify the sample's saturation by performing a series of B checks at successively higher pore pressures while maintaining a constant effective stress of 250 psi. The first B check is initiated by opening a new data log in PumpWorks (using a log interval of 0.5 minutes) and in LabView (using a moving average of 1). Next, slowly close the fluid line valves bounding the experimental cell to prevent the pore pressure from changing beyond ± 10 psi of the prescribed value. Give a period of 5-10 minutes for the pore pressure to equilibrate, after which increase the confining stress by an increment of 200 psi. In order for the B check to be interpretable, it is desirable to observe the change in pore pressure for a period of ~20-30 minutes. The optimal test will yield a pore pressure that reaches a value that is approximately constant shortly after the confining stress increment is fully applied. Once this can be confirmed, remove the increment of confining stress by decreasing it back down to its value prior to the start of the B test. Re-open the fluid line valves bounding the cell at a controlled speed to ensure the pore pressure does not change by an amount that is ± 10 psi of the prescribed value, then set up a new data log in both PumpWorks (log interval of 10 minutes) and LabView (moving average of 300).

Next, increase the pore pressure and confining stress uniformly by 100-200 psi. After a period of 24 hours, perform the next B check by following the same procedure previously described. Continue this process of uniformly increasing the pore pressure and

confining stress of 100-200 psi, waiting 24 hours, and performing the *B* check until three *B* checks have been performed.

At the conclusion of each *B* check, analyze the resulting *B* value (see "*B* Test Interpretation" below) and compare the results to the other *B* check *B* values. According to Wissa (1969), the *B* value for a saturated rock should be constant and independent of the pore pressure for soils of low compressibility. Thus, the sample is considered fully saturated if the *B* value does not change with each successive increase in pressure and stress. If, however, the *B* value does change (because, e.g., gas is still being forced into solution), continue the process of uniformly increasing the pore pressure and confining stress and measuring the *B* value until a consistent *B* value can be achieved.

The final step in the experimental procedure before the *B* coefficient is measured at an effective stress representative of the field is to subject the sample to a series of stress cycles. With both fluid line valves open, increase the confining stress to 9,500 psi (which is 500 psi below the system's working capacity) and hold it at this state for 24 hours (the pore pressure pump should continue to operate during this process to maintain a fixed pore pressure). After this period, reduce the confining stress to achieve an effective stress that matches the sample's in situ effective stress. Thereupon allow the sample to sit for an additional 24 hours before performing a second a final stress cycle.

The sample is now ready for its *B* coefficient to be measured. *B* is measured at the samples in-situ effective stress by following the same procedure described in the "*B* check." The only difference is the confining stress and pore pressure are not progressively increased after each *B* test. Perform the *B* test ~3-5 times to determine an average *B* coefficient, and provide a period of 24 hours in between each test.

The final procedure involves removing the confining stress and back pressure over a 24-hour period. Once done, extract the sample from the cell and transport it to a fume

hood. Use a paper towel saturated with dodecane to absorb any excess dodecane. Immediately following this, record the sample's wet mass, wrap the sample in plastic wrap, and assess its porosity using nuclear magnetic resonance (NMR) testing (the reader is referred to Appendix D.2 in Ramiro-Ramirez (2022) for detailed instruction on NMR testing). Then, image the sample a final time with CT scans (the reader is referred to Appendix D.2 in Ramiro-Ramirez (2022) for detailed instruction on NMR testing).

D.6 SKEMPTON'S *B* TEST INTERPRETATION

The process to interpret the results of a B test is next outlined using an example test depicted in Figure D.3. Time is plotted against the confining stress and the pore pressure. Record both the initial confining stress (σ_i) and the initial pore pressure (u_i) at the moment before application of the applied load. The incremental change in confining stress is then computed at each subsequent measurment of confining stress (σ_n) as:

$$\Delta\sigma = \sigma_i - \sigma_n \tag{D.1}$$

and, in a similar manner, the incremental change in pore pressure is calculate at each subsequent measurement of pore pressure (u_n) as:

$$\Delta u = u_i - u_n \tag{D.2}$$

The resulting B coefficient is then calculated at each datapoint using Eqs. (D.1) and (D.2):

$$B = \frac{\Delta u}{\Delta \sigma} \tag{D.3}$$

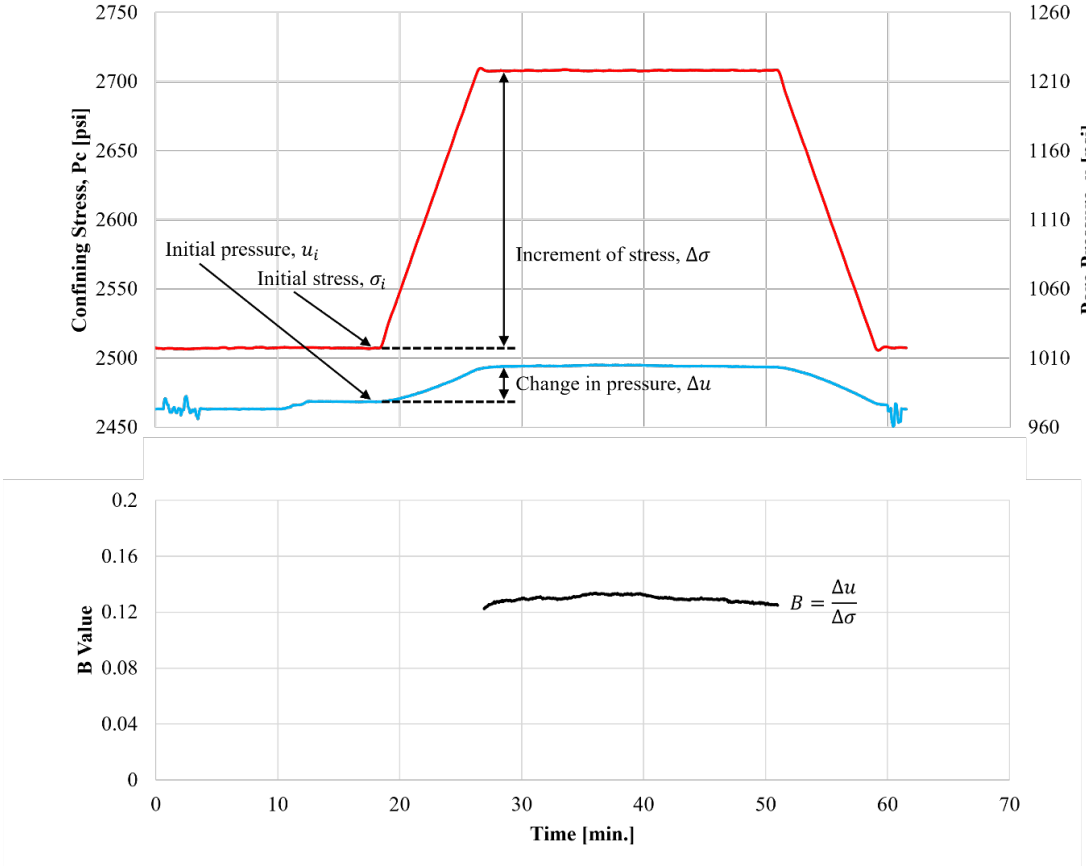

Figure D.3: Experimental results of a B test. The red curve represents the confining stress, the blue curve represents the pore pressure, and the black line represents the ratio of pore pressure to confining stress.

In the example presented above, there is a slight degree of scatter in the resulting *B* coefficient. This is commonly observed among the experimental *B* measurements that were conducted, and is probably due to small changes in temperature (here the changes in pore pressure due to the viscous nature of the test sample is not considered; see Makhnenko and Podladchikov (2018) for a discussion on this behavior). The final *B* coefficient was determined at the maximum calculated value. This interpretation technique aligns with the method determined by the American Society for Testing and Material (ASTM) D7181, and

it was found to be a consistent approach to interpret B across the numerous experimental B tests that were conducted.

Appendix E: P-Wave Velocity from Density

Some well intervals contain density measurements but lack P-wave velocity data. This is observed in the shallow section of wells "h" and "g." I use the empirical relation proposed by Gardner et al. (1974) to derive P-wave velocity from density:

$$Vp = \left(\frac{\rho_b}{a}\right)^{b^{-1}} \quad \text{(E.1)}$$

where Vp is the P-wave velocity in ft/s, ρ_b is the bulk density in g/cm^3, a is an empirical constant with dimensions $\frac{g*s}{cm^3*ft^b}$, and b is a dimensionless empirical constant.

I determine a and b by fitting a curve that best fits the data in a cross-plot of velocity against density in the sections where both measurements are available (Figure E.2). For well "g," the results yield a = 0.234 $\frac{g*s}{cm^3*ft^b}$ and b = 0.250 (Figure E.1); well "h", a = 0.236 $\frac{g*s}{cm^3*ft^b}$ and b = 0.250 (Figure E.2).

I then apply Eq. E.1 to estimate the P-wave velocity in the shallow section of the wells where it is missing. Figure E.3 and Figure E.4 show a comparison of the P-wave velocity estimated from density (orange line) and the measured P-wave velocity (black line) for wells "g" and "h," respectively.

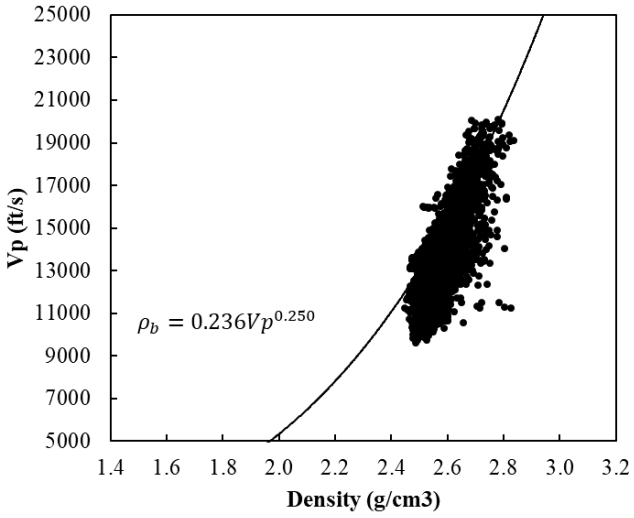

Figure E.1: Well "g" cross-plot of P-wave velocity vs. density. The black dots represent measured data points.

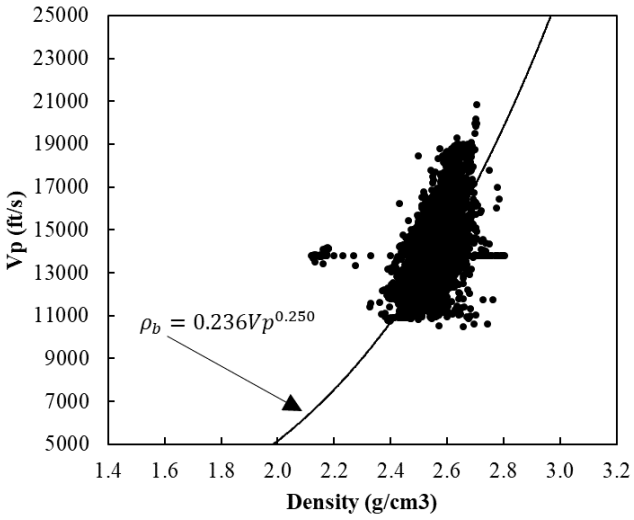

Figure E.2: Well “h” cross-plot of P-wave velocity vs. density. The black dots represent measured data points.

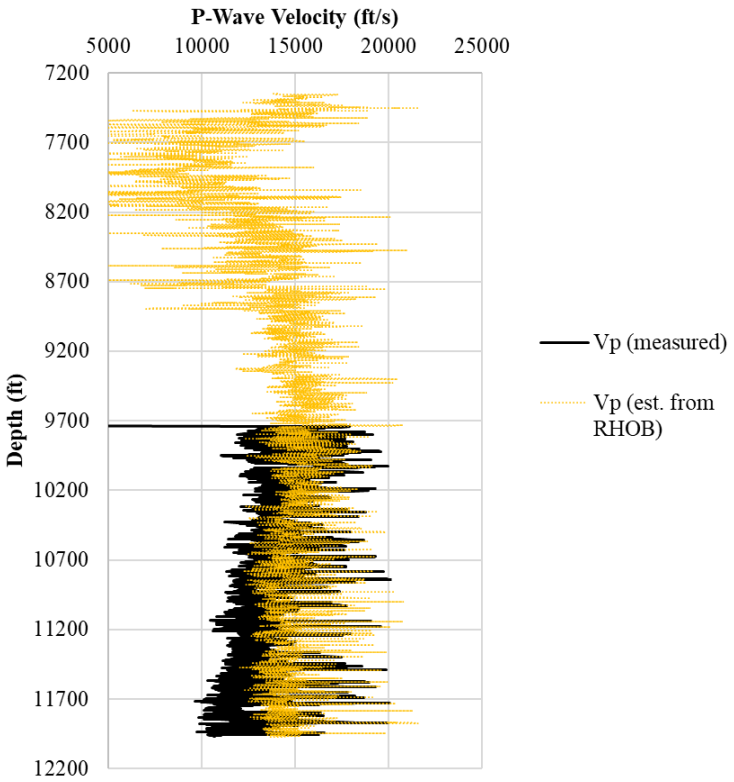

Figure E.3: Well “g” estimated P-wave velocity from density. Estimated P-wave velocity from density (orange); measured P-wave velocity (black).

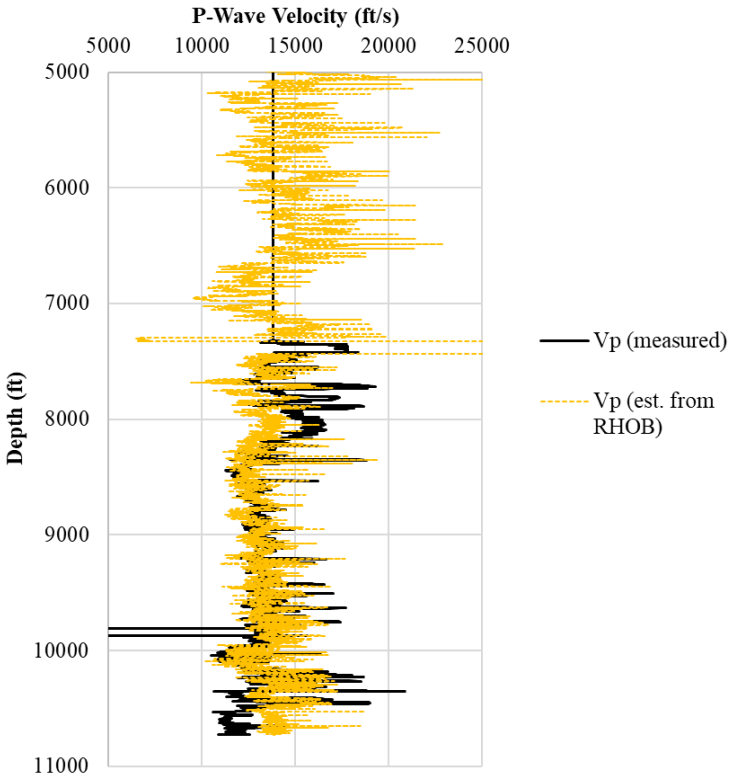

Figure E.4: Well “h” estimated P-wave velocity from density. Estimated P-wave velocity from density (orange); measured P-wave velocity (black).

Appendix F: Porosity to Velocity Discussion

Pore pressure is determined from the mudrock compaction state, and the most direct measure of the mudrock compaction state is porosity. Under increasing stress, porosity will decrease and effective stress will correspondingly increase. With the known effective stress, pore pressure can be determined using Terzaghi's relationship (Eq. 2.2).

While there exist numerous ways to relate effective stress to porosity, and likewise many that relate porosity to velocity (or some other proxy of porosity, such as resistivity or density), it is common in pore pressure prediction to bypass the mapping of velocity to porosity to effective stress, and instead directly relate velocity to effective stress. However, it is important to note that, despite this common approach, there is not a simple one-to-one mapping between velocity and porosity.

As discussed in Dutta (2002), rock velocity depends on a number of parameters beyond porosity: fluid saturation, stress state, confining stress, pore structure, lithology, clay content, cementation, and wave frequency. A key technique of most pore pressure prediction approaches is to pick consistent mudrocks on which to perform pressure analysis (Merrell, 2012). This allows for effective stress to be related to velocity as a function of the type of mudrock picked. In the equation I developed to predict pore pressure in this dissertation, this is handled by the lithology-dependent A and B coefficients (introduced in chapter 2 (Eqns. 2.1 and 2.3), and presented in the final pore pressure prediction equation in Chapter 4 as Eq. 4.28).

However, my work extends beyond lithological constraints. I use the principles of elastoplasticity to account for the stress state of an unloaded mudrock. Within this framework, I quantify the undrained change in pore pressure due to both mechanical

changes in stress (through the uniaxial strain pore pressure buildup coefficient C) and the changes in temperature (through the thermal pressure coefficient α).

Despite the complexity of the relationship between velocity and porosity, I have shown in my dissertation that velocity can practically reflect the compaction state of a mudrock with a history of uplift and erosion if the causal mechanisms of overpressure are formally taken into account. However, further work would be required to better understand the exact relationship between velocity and porosity in unloaded basins.

Works Cited

Athy, L. F., 1930, Density, porosity, and compaction of sedimentary rocks: AAPG Bulletin, v. 14, no. 1, p. 1-24.

Bachman, G. O., 1984, Regional geology of Ochoan evaporites, northern part of Delaware Basin, New Mexico Bureau of Mines & Mineral Resources.

Bachu, S., and Underschultz, J. R., 1995, Large-scale underpressuring in the Mississippian-Cretaceous succession, southwestern Alberta Basin: AAPG bulletin, v. 79, no. 7, p. 989-1004.

Batzle, M., and Wang, Z., 1992, Seismic properties of pore fluids: Geophysics, v. 57, no. 11, p. 1396-1408.

Bearce, H. W., and Peffer, E. L., 1916, Density and thermal expansion of American petroleum oils, US Government Printing Office, v. 77.

Bekele, E. B., Rostron, B. J., and Person, M. A., 2003, Fluid pressure implications of erosional unloading, basin hydrodynamics and glaciation in the Alberta Basin, Western Canada: Journal of Geochemical Exploration, v. 78, p. 143-147.

Bernabe, Y., The effective pressure law for permeability in Chelmsford granite and Barre granite, *in* Proceedings International Journal of Rock Mechanics and Mining Sciences & Geomechanics Abstracts1986, Volume 23, Elsevier, p. 267-275.

Bishop, A., 1976, The influence of system compressibility on the observed pore-pressure response to an undrained change in stress in saturated rock: Géotechnique, v. 26, no. 2, p. 371-375.

Bondarenko, N., Podladchikov, Y., and Makhnenko, R., 2022, Hydromechanical impact of basement rock on injection-induced seismicity in Illinois Basin: Scientific reports, v. 12, no. 1, p. 15639.

Bowers, G. L., 1995, Pore pressure estimation from velocity data: Accounting for overpressure mechanisms besides undercompaction: SPE Drilling & Completion, v. 10, no. 02, p. 89-95.

-, Determining an appropriate pore-pressure estimation strategy, *in* Proceedings Offshore technology conference2001, Offshore Technology Conference.

-, 2002, Detecting high overpressure: The Leading Edge, v. 21, no. 2, p. 174-177.

Casey, B., Germaine, J., Flemings, P., and Fahy, B., 2015, Estimating horizontal stresses for mudrocks under one-dimensional compression: Marine and Petroleum Geology, v. 65, p. 178-186.

Chiu, S.-L., 1996, Behaviour of normally consolidated clay at elevated temperature.

Corbet, T. F., and Bethke, C. M., 1992, Disequilibrium fluid pressures and groundwater flow in the Western Canada sedimentary basin: Journal of Geophysical Research: Solid Earth, v. 97, no. B5, p. 7203-7217.

Couzens-Schultz, B., Axon, A., Azbel, K., Haugland, M., Sarker, R., Tichelaar, B., Wiesneck, J., Wilheml, R., Zhang, J., and Zhang, Z., Pore pressure prediction in unconventional resources, *in* Proceedings IPTC 2013: International Petroleum Technology Conference2013.

dos Santos Junior, J. J. P., Pereira, R. G., de Mendonça, A. J., do Espirito Santo Filho, D. M., Rosendahl-Avelino, M., and Gouveia, J. M., 2022, Determination of Density, Isobaric Thermal Expansivity Coefficient and Isothermal Compressibility Coefficient Correlations for n-Dodecane and n-Nonane, as a Function of Temperature and Pressure: International Journal of Thermophysics, v. 43, no. 7, p. 107.

Dutta, N., 2002, Geopressure prediction using seismic data: Current status and the road ahead: Geophysics, v. 67, no. 6, p. 2012-2041.

Dutton, S. P., Kim, E. M., Broadhead, R. F., Breton, C. L., Raatz, W. D., Ruppel, S. C., and Kerans, C., 2004, Play analysis and digital portfolio of major oil reservoirs in the Permian Basin: application and transfer of advanced geological and engineering technologies for incremental production opportunities: University of Texas (US).

Dvorkin, J., Walls, J., and Davalos, G., 2021, Velocity-porosity-mineralogy model for unconventional shale and its applications to digital rock physics: Frontiers in Earth Science, v. 8, p. 613716.

Eaton, B. A., The equation for geopressure prediction from well logs, *in* Proceedings Fall meeting of the Society of Petroleum Engineers of AIME1975, Society of Petroleum Engineers.

Fjaer, E., Holt, R. M., Horsrud, P., and Raaen, A. M., 2008, Petroleum related rock mechanics, Elsevier.

Fjær, E., Stroisz, A. M., and Holt, R. M., 2013, Elastic dispersion derived from a combination of static and dynamic measurements: Rock Mechanics and Rock Engineering, v. 46, p. 611-618.

Flemings, P., 2021, A Concise Guide to Geopressure: Origin, Prediction, and Applications, Cambridge Press.

Gardner, G., Gardner, L., and Gregory, A., 1974, Formation velocity and density—The diagnostic basics for stratigraphic traps: Geophysics, v. 39, no. 6, p. 770-780.

Germaine, J., 2020, Vertical Velocity Measurements during Uniaxial Unloading of Mudrocks, Presented at the UT GeoFluids Consortium Annual Meeting (11.05): Austin, TX.

Germaine, J. T., and Germaine, A. V., 2009, Geotechnical laboratory measurements for engineers, John Wiley & Sons.

Green, D. H., and Wang, H. F., 1986, Fluid pressure response to undrained compression in saturated sedimentary rock: Geophysics, v. 51, no. 4, p. 948-956.

Gutierrez, M. A., Braunsdor, N. R., and Couzens, B. A., 2006, Calibration and ranking of pore-pressure prediction models: The Leading Edge, v. 25, no. 12, p. 1516-1523.

Heidari, M., Nikolinakou, M., and Flemings, P., 2018, Coupling geomechanical modeling with seismic pressure prediction: Geophysics.

Heppard, P., and Ebrom, D., 2010, Compaction and overpressure in shales: Practice and theory.

Hill, R., 1952, The elastic behaviour of a crystalline aggregate: Proceedings of the Physical Society. Section A, v. 65, no. 5, p. 349.

Hottmann, C., and Johnson, R., 1965, Estimation of formation pressures from log-derived shale properties: Journal of Petroleum Technology, v. 17, no. 06, p. 717-722.
Kim, H., and Makhnenko, R. Y., 2023, Characterization of multiphase flow in shaly caprock for geologic CO2 storage: Advances in Water Resources, v. 182, p. 104570.
Kim, K., and Makhnenko, R. Y., 2020, Coupling between poromechanical behavior and fluid flow in tight rock: Transport in Porous Media, v. 135, no. 2, p. 487-512.
-, 2022, Short-and long-term responses of reservoir rock induced by CO2 injection: Rock Mechanics and Rock Engineering, v. 55, no. 11, p. 6605-6625.
King, M., Static and dynamic elastic moduli of rocks under pressure, *in* Proceedings ARMA US Rock Mechanics/Geomechanics Symposium1969, ARMA, p. ARMA-69-0329.
Lambe, T. W., and Whitman, R. V., 1969, Soil mechanics SI version, John Wiley & Sons.
Law, B. E., and Spencer, C., 1998, Memoir 70, chapter 1: Abnormal pressure in hydrocarbon environments.
Lee, M.-K., and Williams, D. D., 2000, Paleohydrology of the Delaware basin, western Texas: overpressure development, hydrocarbon migration, and ore genesis: AAPG bulletin, v. 84, no. 7, p. 961-974.
Lockhart, L. P., 2018, Pore pressure prediction: from vertical stress to mean stress to the full stress tensor.
Lockhart, L. P., Flemings, P. B., Nikolinakou, M., and Germaine, J., 2023, Velocity-based pore pressure prediction in a basin with late-stage erosion: Delaware Basin, US: Marine and Petroleum Geology, v. 150, p. 106159.
Loughry, D., Epps, D., and Forrest, J., Using pad ISIP, DFIT, and ESP data to generate a pore pressure model for the Midland Basin, *in* Proceedings Unconventional Resources Technology Conference, San Antonio, Texas, 20-22 July 20152015, Society of Exploration Geophysicists, American Association of Petroleum …, p. 1702-1710.
Luffel, D., and Guidry, F., 1992, New core analysis methods for measuring reservoir rock properties of Devonian shale: Journal of Petroleum Technology, v. 44, no. 11, p. 1184-1190.
Luo, M., Baker, M. R., and LeMone, D. V., 1994, Distribution and generation of the overpressure system, eastern Delaware Basin, western Texas and southern New Mexico: AAPG bulletin, v. 78, no. 9, p. 1386-1405.
Makhnenko, R., and Labuz, J. F., Saturation of porous rock and measurement of the B coefficient, *in* Proceedings ARMA US Rock Mechanics/Geomechanics Symposium2013, ARMA, p. ARMA-2013-2468.
Makhnenko, R. Y., and Podladchikov, Y. Y., 2018, Experimental poroviscoelasticity of common sedimentary rocks: Journal of Geophysical Research: Solid Earth, v. 123, no. 9, p. 7586-7603.
Mavko, G., Mukerji, T., and Dvorkin, J., 2020, The rock physics handbook, Cambridge university press.

Mayer, L. M., Macko, S. A., Mook, W. H., and Murray, S., 1981, The distribution of bromine in coastal sediments and its use as a source indicator for organic matter: Organic Geochemistry, v. 3, no. 1-2, p. 37-42.
Merrell, M. P., 2012, Pressure and stress at Mad Dog field, Gulf of Mexico.
Merrell, M. P., Flemings, P. B., and Bowers, G. L., 2014, Subsalt pressure prediction in the Miocene Mad Dog field, Gulf of Mexico: AAPG bulletin, v. 98, no. 2, p. 315-340.
Neuzil, C., and Pollock, D., 1983, Erosional unloading and fluid pressures in hydraulically" tight" rocks: The Journal of Geology, v. 91, no. 2, p. 179-193.
Neuzil, C. E., and Provost, A. M., 2014, Ice sheet load cycling and fluid underpressures in the Eastern Michigan Basin, Ontario, Canada: Journal of Geophysical Research: Solid Earth, v. 119, no. 12, p. 8748-8769.
Nikolinakou, M., Heidari, M., and Flemings, P., Pore-pressure prediction based on seismic velocities coupled with geomechanical modeling, *in* Proceedings 50th US Rock Mechanics/Geomechanics Symposium2016, American Rock Mechanics Association.
Obradors-Prats, J., Rouainia, M., Aplin, A. C., and Crook, A. J., 2017, Assessing the implications of tectonic compaction on pore pressure using a coupled geomechanical approach: Marine and Petroleum Geology, v. 79, p. 31-43.
Palciauskas, V., and Domenico, P., 1982, Characterization of drained and undrained response of thermally loaded repository rocks: Water Resources Research, v. 18, no. 2, p. 281-290.
-, 1989, Fluid pressures in deforming porous rocks: Water Resources Research, v. 25, no. 2, p. 203-213.
Pearson, C., 1981, The relationship between microseismicity and high pore pressures during hydraulic stimulation experiments in low permeability granitic rocks: Journal of Geophysical Research: Solid Earth, v. 86, no. B9, p. 7855-7864.
Plona, T., and Cook, J., Effects of stress cycles on static and dynamic Young's moduli in Castlegate sandstone, *in* Proceedings ARMA US Rock Mechanics/Geomechanics Symposium1995, ARMA, p. ARMA-95-0155.
Pskowski, M. B. D., 2024, Companies aim to release more treated oilfield wastewater into rivers and streams: The Texas Tribune.
Ramiro-Ramirez, S., 2022, Integrated stratigraphic and petrophysical analysis of the Wolfcamp at Delaware Basin, West Texas, USA.
Ramiro-Ramirez, S., Bhandari, A. R., Flemings, P. B., and Reed, R. M., Porosity and Permeability Heterogeneity in the Upper Wolfcamp, Delaware Basin, West Texas: Implications for Production, *in* Proceedings Unconventional Resources Technology Conference, 20–22 July 20202020, Unconventional Resources Technology Conference (URTeC), p. 1321-1328.
Ramiro-Ramirez, S., Bhandari, A. R., Reed, R. M., and Flemings, P. B., 2024, Permeability of upper Wolfcamp lithofacies in the Delaware Basin: The role of stratigraphic heterogeneity in the production of unconventional reservoirs: AAPG Bulletin, v. 108, no. 2, p. 293-326.

Rieder, M., Cavazzini, G., D'yakonov, Y. S., Frank-Kamenetskii, V. A., Gottardi, G., Guggenheim, S., Koval, P. W., Müller, G., Neiva, A. M., and Radoslovich, E. W., 1998, Nomenclature of the micas: Clays and clay minerals, v. 46, no. 5, p. 586-595.

Rittenhouse, S., Currie, J., and Blumstein, R., Using mud weights, DST, and DFIT data to generate a regional pore pressure model for the Delaware Basin, New Mexico and Texas, *in* Proceedings Unconventional Resources Technology Conference, San Antonio, Texas, 1-3 August 20162016, Society of Exploration Geophysicists, American Association of Petroleum …, p. 1243-1252.

Rubey, W. W., and Hubbert, M. K., 1959, Overthrust belt in geosynclinal area of western Wyoming in light of fluid pressure hypothesis: Geol. Soc: America Bull, v. 70, no. 2, p. 167-205.

Sanford, J. C., 2015, The Cretaceous-Paleogene boundary deposit in the Gulf of Mexico: oceanic basin response to the Chicxulub impact and geomechanics of reservoir-scale sand injectites, Panoche Hills, California.

Sayers, C. M., Johnson, G., and Denyer, G., 2002, Predrill pore-pressure prediction using seismic data: Geophysics, v. 67, no. 4, p. 1286-1292.

Schlumberger, 2005, Log Interpretation Charts, Houston, Texas, USA.

Sinclair, T., 2007, The generation and continued existence of overpressure in the Delaware Basin: Texas (PhD thesis) Durham University, Durham, UK.

Skempton, A., 1954, The pore-pressure coefficients A and B: Geotechnique, v. 4, no. 4, p. 143-147.

Swarbrick, R., Lahann, R., O'Connor, S., and Hoskin, E., Limitations of seismic pore pressure prediction-what is the alternative?, *in* Proceedings 75th EAGE Conference & Exhibition-Workshops2013, European Association of Geoscientists & Engineers, p. cp-349-00109.

Sweatman, R., Faul, R., and Ballew, C., New solutions for subsalt-well lost circulation and optimized primary cementing, *in* Proceedings SPE annual technical conference1999, p. 157-167.

Terzaghi, K. v., 1923, Die berechnung der durchlassigkeitsziffer des tones aus dem verlauf der hydrodynamischen spannungserscheinungen: Sitzungsberichte der Akademie der Wissenschaften in Wien, Mathematisch-Naturwissenschaftliche Klasse, Abteilung IIa, v. 132, p. 125-138.

Tribovillard, N., Algeo, T. J., Lyons, T., and Riboulleau, A., 2006, Trace metals as paleoredox and paleoproductivity proxies: an update: Chemical geology, v. 232, no. 1-2, p. 12-32.

Wang, F., Saeki, S., and Yamaguchi, T., 1997, Temperature and pressure dependence of thermal expansion coefficient and thermal pressure coefficient for amorphous polymers: Polymer, v. 38, no. 14, p. 3485-3492.

Wang, H., 2000a, Theory of linear poroelasticity with applications to geomechanics and hydrogeology, Princeton university press.

Wang, H., 2000b, Theory of linear poroelasticity: with applications to geomechanics and hydrogeology, Princeton, NJ, Princeton University Press, Princeton Series in Geophysics.
Wang, Z., Wang, H., and Cates, M. E., 2001, Effective elastic properties of solid clays: Geophysics, v. 66, no. 2, p. 428-440.
Warplnski, N., and Teufel, L., 1992, Determination of the effective stress law for permeability and deformation in low-permeability rocks: SPE formation evaluation, v. 7, no. 02, p. 123-131.
Weaver, C. E., 1965, Potassium content of illite: Science, v. 147, no. 3658, p. 603-605.
Westbrook, G., and Smith, M., 1983, Long decollements and mud volcanoes: Evidence from the Barbados Ridge Complex for the role of high pore-fluid pressure in the development of an accretionary complex: Geology, v. 11, no. 5, p. 279-283.
Wissa, A. E., 1969, Pore pressure measurement in saturated stiff soils: Journal of the Soil Mechanics and Foundations Division, v. 95, no. 4, p. 1063-1073.
Xia, X., Wallace, J., and Du, L., Modeling of abnormal fluid pressure in unconventional plays due to uplift, *in* Proceedings Unconventional Resources Technology Conference2013, Society of Exploration Geophysicists, American Association of Petroleum …, p. 2487-2495.
Zhang, J., 2011, Pore pressure prediction from well logs: Methods, modifications, and new approaches: Earth-Science Reviews, v. 108, no. 1-2, p. 50-63.
-, 2013, Effective stress, porosity, velocity and abnormal pore pressure prediction accounting for compaction disequilibrium and unloading: Marine and Petroleum Geology, v. 45, p. 2-11.
Zheng, S., and Sharma, M. M., 2021, Modeling Hydraulic Fracturing Using Natural Gas Foam as Fracturing Fluids: Energies, v. 14, no. 22, p. 7645.
Zimmer, M. A., 2004, Seismic velocities in unconsolidated sands: Measurements of pressure, sorting, and compaction effects, Stanford University.
Zoback, M. D., and Gorelick, S. M., 2012, Earthquake triggering and large-scale geologic storage of carbon dioxide: Proceedings of the National Academy of Sciences, v. 109, no. 26, p. 10164-10168.